

**FEASIBILITY OF Fe₃O₄ NANOPARTICLES DECORATED
REDUCED GRAPHENE OXIDE HETEROSTRUCTURE AS
PHOTOCATALYST AND CHEMICAL SENSORS**

TEO PEIK SEE

**DISSERTATION SUBMITTED IN FULFILLMENT OF THE
REQUIREMENT FOR THE DEGREE OF
MASTER OF SCIENCE**

**DEPARTMENT OF PHYSICS
FACULTY OF SCIENCE
UNIVERSITY OF MALAYA
KUALA LUMPUR**

2015

UNIVERSITI MALAYA

ORIGINAL LITERARY WORK DECLARATION

Name of Candidate: **Teo Peik See** (I.C/Passport No: **880616-35-5036**)

Registration/Matric No: **SGR110127**

Name of Degree: **Master of Science (Dissertation)**

Title of Project ~~Paper/Research Report/Dissertation/Thesis~~ (“this Work”):

FEASIBILITY OF Fe₃O₄ NANOPARTICLES DECORATED REDUCED GRAPHENE OXIDE HETEROSTRUCTURE AS PHOTOCATALYST AND CHEMICAL SENSOR

Field of Study: **Nanomaterials**

I do solemnly and sincerely declare that:

- (1) I am the sole author/writer of this Work;
- (2) This Work is original;
- (3) Any use of any work in which copyright exists was done by way of fair dealing and for permitted purposes and any excerpt or extract from, or reference to or reproduction of any copyright work has been disclosed expressly and sufficiently and the title of the Work and its authorship have been acknowledged in this Work;
- (4) I do not have any actual knowledge nor do I ought reasonably to know that the making of this work constitutes an infringement of any copyright work;
- (5) I hereby assign all and every rights in the copyright to this Work to the University of Malaya (“UM”), who henceforth shall be owner of the copyright in this Work and that any reproduction or use in any form or by any means whatsoever is prohibited without the written consent of UM having been first had and obtained;
- (6) I am fully aware that if in the course of making this Work I have infringed any copyright whether intentionally or otherwise, I may be subject to legal action or any other action as may be determined by UM.

Candidate’s Signature:

Date:

Subscribed and solemnly declared before,

Witness’s Signature:

Date:

Name: **Dr. Huang Nay Ming**

Designation: **Senior Lecturer**

ABSTRACT

In this study, iron oxide/reduced graphene oxide ($\text{Fe}_3\text{O}_4/\text{rGO}$) nanocomposite materials were successfully synthesized *via* a simple, eco-friendly and cost-effective approach at room temperature. The XRD spectra indicated peaks that attributed to the face-centre-cubic phase Fe_3O_4 , while the absence peak of GO in nanocomposite provides evidence for the reduction of GO. The field emission scanning electron microscopic (FESEM) images showed Fe_3O_4 nanoparticles were uniformly deposited on the rGO sheets with a narrow size distribution for all the nanocomposites. Besides, the synthesized $\text{Fe}_3\text{O}_4/\text{rGO}$ nanocomposites were found to be superparamagnetic in nature at room temperature. In the photocatalysis application, methylene blue (MB) solution was used as a model organic pollutant; the $\text{Fe}_3\text{O}_4/\text{rGO}$ nanocomposite materials showed better adsorption and excellent photocatalytic activity towards the degradation of MB under natural sunlight irradiation due to the synergistic effect that arises between rGO and Fe_3O_4 nanoparticles. Interestingly, a maximum photodegradation of almost 100% MB were achieved at 1 h light irradiation. Moreover, the magnetically separable $\text{Fe}_3\text{O}_4/\text{rGO}$ nanocomposite exhibit good sustainability and photocatalytically stable morphology even after eight cycles of photocatalytic treatment. Thus, this newly prepared $\text{Fe}_3\text{O}_4/\text{rGO}$ nanocomposite could serve as potential candidate in variety environmental remediation. The electrochemical studies were carried out with the iron oxide/graphene modified glassy carbon electrode ($\text{Fe}_3\text{O}_4/\text{rGO}/\text{GCE}$) for the simultaneous detection of dopamine (DA) and ascorbic acid (AA). The detection limit ($S/N=3$) was found to be $0.42 \mu\text{M}$ and $0.12 \mu\text{M}$ for AA and DA, respectively. The $\text{Fe}_3\text{O}_4/\text{rGO}/\text{GCE}$ displayed not only excellent electrocatalytic activity and remarkable electron transfer kinetics towards the oxidation of DA but also portrayed capability of high sensitivity and selectivity toward simultaneous detection of AA and DA. In a nutshell, the $\text{Fe}_3\text{O}_4/\text{rGO}/\text{GCE}$ has

been proved as a promising candidate and applicable for electrocatalysis and chemical sensor applications.

ABSTRAK

Dalam penyelidikan kajian ini, graphene oksida terturun /ferum oksida ($\text{Fe}_3\text{O}_4/\text{rGO}$) nanokomposit telah berjaya disintesis dengan melalui kaedah yang ringkas, mesra alam serta kos yang efektif pada suhu bilik. Spektra XRD menunjukkan puncak kiub berpusat muka bagi Fe_3O_4 sementara ketiadaan puncak GO dalam nanokomposit membuktikan penurunan GO. Imej bagi mikroskopi elektron imbasan pancaran medan (FESEM) menunjukkan Fe_3O_4 nanopartikel tertabur dengan sekata pada kepingan rGO dengan taburan saiz yang kecil untuk kesemua nanokomposit. Selain itu, $\text{Fe}_3\text{O}_4/\text{rGO}$ yang disintesis didapati bersifat superparamagnetik pada suhu bilik. Dalam aplikasi fotomangkin, di bawah sinaran matahari dengan menggunakan metilena biru (MB) sebagai model pencemar organik, $\text{Fe}_3\text{O}_4/\text{rGO}$ nanokomposit mempamerkan penjerapan yang lebih baik dan aktiviti fotomangkin yang cemerlang terhadap degradasi MB masing-masing disebabkan kesan sinergi di antara rGO dan Fe_3O_4 nanopartikel. Menariknya, pemfotorosotaan maksimum hampir 100% MB telah dicapai dalam masa sejam bawah penyinaran cahaya. Di samping itu, pemisahan secara magnetik oleh $\text{Fe}_3\text{O}_4/\text{rGO}$ nanokomposit menunjukkan kemampuan yang baik dan kestabilan aktiviti fotomangkin pada morfologi walaupun selepas lapan kitaran operasi fotomangkin. Oleh itu, bahan baru $\text{Fe}_3\text{O}_4/\text{rGO}$ ini boleh dianggap sebagai calon potensi dalam pelbagai jenis pemulihan alam sekitar. Pengajian elektrokimia telah dijalankan dengan menggunakan elektrod karbon berkaca ($\text{Fe}_3\text{O}_4/\text{rGO}/\text{GCE}$) termodifikasi dengan ferum oksida/graphene oksida terturun bagi pengesanan dopamine (DA) dan asid askorbik (AA) secara serentak. Had pengesanan ($S/N=3$) didapati $0.42 \mu\text{M}$ dan $0.12 \mu\text{M}$ untuk AA dan DA masing-masing. $\text{Fe}_3\text{O}_4/\text{rGO}/\text{GCE}$ bukan sahaja memaparkan aktiviti elektrokatalitik yang cemerlang serta pemindahan elektron kinetik luar biasa terhadap pengoksidaan DA malahan menunjukkan kemampuan sensitif dan pemilihan dalam penentuan serentak AA dan DA secara elektrokimia. Justeru itu, $\text{Fe}_3\text{O}_4/\text{rGO}/\text{GCE}$ telah

terbukti sebagai calon terpilih yang boleh diaplikasikan dalam bidang elektrokimia dan pengesanan kimia.

ACKNOWLEDGEMENT

At the beginning of my thesis, I am very thankful to everyone for their help, encouragements and contributions to success my research work. First and foremost, a deeply and forever thanks go to my lovely parents and siblings for giving strength and great support with their love and encouragement.

Next, I would like to express my deeply gratitude and sincere appreciation to my supervisor, Dr. Huang Nay Ming for his great guidance, suggestions, tremendous support and enthusiasm throughout my research work. I am grateful being part of his group and experience a great joyful time under his supervision.

Besides, a grateful appreciates and sincere thanks to Dr. Lim Hong Ngee and Dr. Alagarsamy Pandikumar for their valuable assistance, kind advice as well as motivation throughout the course of study. In the completion of this work, my deepest thanks to all of the members of LMDRC for having a friendly working environment, and valuable technical assistance and help. My special thanks also go to my group members, Fatin Saiha, Su Pei, Gregory, Norazriena, Marlinda, Vanessa Lee and John Gan for their sharing knowledge, endless kindness and assistance.

Last but not least, I would like to convey appreciate thanks to Exploratory Research Grant Scheme (ER016–2011A), the Fundamental Research Grant Scheme (UKM-FST-07-FRGS0233–2010), the High Impact Research Grant of the University of Malaya (UM.C/625/1/HIR/030) and the High Impact Research Grant from the Ministry of Higher Education of Malaysia (UM.C/625/1/HIR/MOHE/05), University of Malaya for the Postgraduate Research Grant (PPP) (PG107-2012B) and UMRG programme grant (RP007C/13AFR) for the financial support.

TABLE OF CONTENTS

ORIGINAL LITERARY WORK DECLARATION	ii
ABSTRACT.....	iii
ABSTRAK.....	v
ACKNOWLEDGEMENT	viii
LIST OF FIGURES	xii
LIST OF TABLES	xivv
LIST OF ABBREVIATIONS.....	xv
LIST OF PUBLICATIONS.....	xix
CHAPTER 1 : INTRODUCTION.....	1
1.1 Research background.....	1
1.1.1 Nanotechnology and Nanomaterials	1
1.1.2 Overview of Graphene	2
1.1.3 Overview of Iron Oxide	4
1.2 Research problems and motivations	5
1.3 Research objectives	7
1.4 Thesis outline.....	8
CHAPTER 2 : LITERATURE REVIEW	10
2.1 Introduction	10
2.2 Graphene.....	10
2.2.1 Properties of Graphene	11
2.2.2 Methods for Graphene Synthesis	14
2.3 Magnetite (Fe ₃ O ₄).....	17
2.3.1 Magnetic properties of Magnetite (Fe ₃ O ₄).....	20
2.3.2 Synthetic Methods for Magnetite (Fe ₃ O ₄)	23
2.4 Magnetite/reduced graphene oxide (Fe ₃ O ₄ /rGO) nanocomposites	25
2.5 Fe ₃ O ₄ /rGO nanocomposites Photocatalysts	27
2.5.1 Basic Mechanism for the Photocatalytic Degradation of Organic Pollutants	29
2.6 Electrochemical Sensor Based on Fe ₃ O ₄ /rGO Modified Electrodes.....	31
2.6.1 Dopamine (DA)	31
2.6.2 Electrochemical Sensor.....	33
CHAPTER 3 : EXPERIMENTAL METHODS	36
3.1 Introduction	36
3.2 Section I.....	36

3.2.1	Chemicals and Materials	36
3.2.2	Synthesis of Fe ₃ O ₄ /rGO	38
3.3	Section II	40
3.3.1	Photocatalytic Activity Measurements.....	40
3.3.1.1	Durability Test.....	41
3.3.2	Electrochemical Studies	41
3.3.2.1	Fabrication of Sensor Electrodes	41
3.3.2.2	Electrochemical Studies of Modified Electrodes	42
3.3.2.3	Electrochemical Detection of Dopamine (DA) and Ascorbic Acid (AA)	43
3.4	Section III	44
3.4.1	Characterization Techniques	44
3.4.2	Field Emission Scanning Electron Microscopy (FESEM).....	45
3.4.3	High Resolution Transmission Electron Microscope (HRTEM).....	47
3.4.4	X-Ray Diffraction (XRD)	48
3.4.5	Micro-Raman spectroscopy.....	49
3.4.7	Ultraviolet-Visible (UV-Vis) Spectroscopy.....	50
3.4.8	Photoluminescence Spectroscopy	51
3.4.9	Vibrating Sample Magnetometer (VSM).....	52
	CHAPTER 4: RESULTS AND DISCUSSION.....	53
4.1	Introduction	53
4.2	Part I	53
4.2.1	Formation mechanism of the Fe ₃ O ₄ /rGO nanocomposite	53
4.3	Part II.....	55
4.3.1	Characterization of Fe ₃ O ₄ /rGO nanocomposites	55
4.3.1.1	Field Emission Scanning Electron Microscopic (FESEM) Studies	55
4.3.1.2	High Resolution Transmission Electron Microscopic Studies.....	57
4.3.1.3	X-Ray Diffraction (XRD)	60
4.3.1.4	Micro-Raman	63
4.3.1.5	UV-visible spectroscopy	64
4.3.1.6	Photoluminescence Emission Spectrum.....	66
4.3.1.7	Vibrating Sampling Magnetometer (VSM) Studies.....	69
4.4	Part III.....	71
4.4.1	Photocatalytic application of Fe ₃ O ₄ /rGO nanocomposites	71
4.4.2	Durability Test Studies of Fe ₃ O ₄ /rGO nanocomposites.....	74

4.4.3	Mechanism for the Photocatalytic Studies of Fe ₃ O ₄ /rGO nanocomposites..	77
4.4.4	Electrochemical Application for Simultaneous Detection Dopamine (DA) and Ascorbic Acid (AA)	78
4.4.4.1	Electrochemical Behaviour of Fe ₃ O ₄ /rGO Nanocomposites	78
4.4.4.2	Electrochemical Impedance Spectroscopy (EIS) of Modified Electrodes	80
4.4.4.3	Electrocatalytic Response of Modified Electrodes towards the Oxidation of Dopamine (DA)	82
4.4.4.4	Mechanism for the Electrocatalytic Oxidation of Dopamine (DA) at Modified Electrodes	83
4.4.4.5	Influence of Scan Rate on the Electrocatalytic Oxidation of DA at G1F5/GCE Electrode.	84
4.4.4.6	Studies of G1F5 Concentration on the Electrocatalytic Activity of DA...86	
4.4.4.7	Selective Determination of Dopamine (DA) In The Presence of Ascorbic Acid (AA).....	87
	CHAPTER 5: CONCLUSION AND FUTURE WORKS	92
5.1	Conclusion	92
5.2	Future works	94
	REFERENCES.....	96

LIST OF FIGURES

Figure 2.1: Graphene as a basic building block for all graphitic dimensionalities (Seyller, 2011).	11
Figure 2.2: The sp^2 hybridization between carbon atoms and formation of π bonds from the unoccupied p-orbital (Ul Hasan, 2012).	12
Figure 2.3: (A) Photographic image of magnetite (Fe_3O_4) and (B) the cubic spinel structure of magnetite (Friak et al., 2007).	20
Figure 2.4: Super-paramagnetic particles versus ferromagnetic particles in (a) presence and (b) absence of external magnetic field (Demas et al., 2011).	22
Figure 2.5: (A) Structure of methylene blue and its reduced form (leucomethylene blue). (B) Picture of methylene blue solution.	28
Figure 2.6: Schematic representation for the photodegradation process in the presence of photocatalysts under visible light irradiation.	31
Figure 2.7: Molecular structure of dopamine (DA).	32
Figure 2.8: Molecular structure of ascorbic acid (AA).	33
Figure 3.1: Schematic route for synthesis of graphene oxide (GO).	38
Figure 3.2: Schematic pathway for the synthesis of Fe_3O_4/rGO nanocomposite.	40
Figure 3.3: Photographic image of VersaSTAT 3 electrochemical analyzer (Princeton Applied Research, USA).	43
Figure 3.4: Electrochemical detection of dopamine and ascorbic acid in three-electrode cell system.	44
Figure 3.5: Characterization techniques involved for Fe_3O_4/rGO nanocomposite.	45
Figure 3.6: Photographic image of FESEM, FEI Nova NanoSEM 400.	46
Figure 3.7: Photographic image of HRTEM, JEM-2100F.	48
Figure 3.8: Photographic image of Renishaw inVia Raman microscope system.	50
Figure 3.9: Photographic image of computer controlled Thermoscientific Evolution 300 UV-vis absorption spectrophotometer machine.	51
Figure 4.1: Schematic illustration for the formation Fe_3O_4/rGO nanocomposite <i>via</i> a one-step in situ chemical deposition method.	54
Figure 4.2: FESEM images of (a) G1, (b) F20, (c) G1F2, (d) G1F5, (e) G1F10 and (f) G1F20; (g) EDX spectrum of G1F2; and (h) elemental mapping of G1F2 based on image shown in (c).	57
Figure 4.3: HR-TEM images of (a) G1, (b) F20, (c) Fe_3O_4/rGO , and (d) at a higher magnification.	58
Figure 4.4: TEM images of (a) G1F2, (b) G1F5, (c) G1F10 and (d) G1F20. The average Fe_3O_4 nanoparticle diameter for each sample is (a) 3.8, (b) 7.9, (c) 10.5 and (d) 12.1 nm.	60
Figure 4.5: XRD patterns of (a) G1, (b) F20, (c) G1F2, (d) G1F5, (e) G1F10 and (f) G1F20.	62
Figure 4.6: Raman spectra of (a) GO, (b) G1, (c) G1F2, (d) G1F5, (e) G1F10, (f) G1F20 and (g) F20.	64
Figure 4.7 (A): UV-vis spectra of (a) GO, (b) G1F2, (c) G1F5, (d) G1F10, (e) G1F20 and (f) F20.	66

Figure 4.1 (B): Tauc's plot of (a) G1F2, (b) G1F5, (c) G1F10, (d) G1F20, (e) F20 and (f) The relationship between band gap energy (E_{bg}) and weight of Fe_3O_4 (mg).....	66
Figure 4.8: Room temperature photoluminescence (PL) spectra of (a) G1F2, (b) rGO, (c) G1F5, (d) G1F10, (e) G1F20 and (f) F20.	68
Figure 4.9: Images of magnetic property and dispersibility of the nanocomposites: (a) F20, (b) dispersed G1F2 unaffected by the magnetic attraction, (c) G1F20 in water (d) G1F20 in ethanol, (e) G1F2 and (f) G1F20.....	70
Figure 4.10: VSM magnetization curves of (a) G1F2, (b) G1F5, (c) G1F10, (d) G1F20 and (e) F20.	71
Figure 4.11: (a) Photocatalytic degradation rate of MB in the presence of different photocatalysts under natural sunlight irradiation. (b) Adsorption of MB solution by different catalysts after 12 h stirring.....	74
Figure 4.12: (a) Photodegradation efficiency (%) of MB solution for 8 cycles in the presence of Fe_3O_4 /rGO nanocomposites and Fe_3O_4 . (b) Photographic images of MB before and after degradation by Fe_3O_4 /rGO and recovery by applying a permanent magnet.	76
Figure 4.13: HR-TEM images of (a) F20, (b) G1F2, (c) G1F5, (d) G1F10 and (e) G1F20.....	76
Figure 4.14: Schematic representation of photodegradation of MB by Fe_3O_4 /rGO nanocomposites under natural sunlight irradiation.	78
Figure 4.15: (A) Cyclic voltammograms obtained for (a) bare GCE and (b) Fe_3O_4 /rGO/GCE in the presence of 5 mM $K_3[Fe(CN)_6]$ and 0.1 M KCl solution at a scan rate of 100 mV/s. (B) Cyclic voltammograms obtained for (a) G1F2/GCE and (b) G1F5/GCE, (c) G1F10/GCE, (d) G1F20/GCE and (e) F20/GCE in the presence of 5 mM $K_3[Fe(CN)_6]$ and 0.1 M KCl solution at a scan rate of 100 mV/s.....	80
Figure 4.16: (A) Nyquist plots obtained for (a) bare GCE, (b) rGO, (c) G1F5 and (c) F20; (B) Nyquist plots for Fe_3O_4 /rGOs (a) G1F2, (b) G1F5, (c) G1F10 and (d) G1F20 in the presence of 5 mM $K_3[Fe(CN)_6]$ / $K_4[Fe(CN)_6]$ (1:1) solution containing 0.1 M KCl. (C) Equivalent electrical circuit for (a) F20 and (b) G1F5.....	81
Figure 4.17: CVs for (a) G1F2, (b) G1F5, (c) G1F10, (d) G1F20 and (e) F20, in the presence of 0.1 M PBS (pH 6.5) containing 0.1 mM DA at a scan rate of 100 mV/s. Inset: Electrochemical detection of 0.1 mM DA for bare GCE, Fe_3O_4 /rGO and F20.	83
Figure 4.18: Electrocatalytic oxidation of dopamine at Fe_3O_4 /rGO/GCE electrode (N. Li et al., 2013).	84
Figure 4.19: (a) CVs observed for G1F5/GCE in 0.1M PBS (pH 6.5) containing 0.1 mM DA at various scan rates ((a)–(j): 10, 20, 40, 60, 80, 100, 150, 200, 250 and 300 mV/s). (b) The plots of peak current vs. the scan rates. (c) Variation of E_p vs. the logarithm of scan rate. (d) Variation of E_p vs. the logarithm of the high scan rates: 600, 650, 700, 750, 800, 850, 900 and 950 mV/s).	86
Figure 4.20: Effect of G1F5 amount of electro-oxidation current response of 0.1 mM DA in 0.1 M PBS (pH 6.5) at a scan rate of 100mV/s.	87

Figure 4.21: DPV response observed for (a) bare GCE and (b) G1F5/GCE electrodes in the presence of 0.1 mM of DA and 3 mM of AA in 0.1 M PBS (pH=6.5)...88

Figure 4.22: (A) DPV response of G1F5/GCE modified electrode with increasing the concentration of DA (from a to n: 0, 0.5, 1, 2, 4, 6, 8, 10, 20, 30, 40, 60, 80 and 100 μM) in the presence of 2 mM AA. (B) The relationship between the oxidation peaks current against DA concentration (0.5–100 μM) in the presence of 2 mM AA. Inset: Enlarge view of calibration plot in the concentration range of 0–10 μM of DA. (C) DPVs response of G1F5/GCE modified electrode with various concentrations of AA (1-25 mM) in the presence of 0.1 mM DA. (D) Calibration plot obtained for oxidation peak current against AA concentration.....90

LIST OF TABLES

Table 3.1: Weight ratios between GO and FeSO ₄ used for the preparation of rGO/Fe ₃ O ₄ nanocomposites.....	39
Table 4.1: EIS fitting parameters for modified electrodes.	81
Table 4.2: Comparison of various modified electrodes for the detection of DA.	91

LIST OF ABBREVIATIONS

α	Charge Transfer Coefficient
α_a	Anodic Transfer Coefficient
I_{pa}, I_{pc}	Anodic and Cathodic Peak Currents
k_s	Apparent Heterogeneous Electron Transfer Rate Constant
$\bullet\text{OH}$	Hydroxyl Radicals
$\text{O}_2^{\bullet-}$	Superoxide Radical Anions
O_2	Oxygen
e^-	Electrons
h^+	Holes
CB	Conduction Band
VB	Valence Band
W/O	Water in Oil
R	Gas
T	Temperature
F	Faraday Constant
H	Hysteresis
R_s	Solution Resistance
Q_{CPE}	Constant Phase Element
R_{ct}	Charge Transfer Resistance
W	Warburg Impedance
LOD	Limit of Detection
2D	Two-Dimensional
Fe_3O_4	Magnetite
FeO	Wustite
GICs	Graphite Intercalation Compounds

GO	Graphene Oxide
HOPG	Highly Oriented Pyrolytic Graphite
MNPs	Magnetic Nanoparticles
rGO	Reduced Graphene Oxide
α -Fe ₂ O ₃	Hematite
γ -Fe ₂ O ₃	Maghemite
BPA	Bisphenol A
DAQ	Dopaminequinone
DA	Dopamine
AA	Ascorbic Acid
UA	Uric Acid
MB	Methylene Blue
NR	Neutral Red
SiC	Silicon Carbide
DI water	Deionized Water
DMF	Dimethylformamide
NMP	<i>N</i> -methyl-2-pyrrolidone
KMnO ₄	Potassium Permanganate
H ₂ SO ₄	Sulfuric Acid
H ₂ O ₂	Hydrogen Peroxide
NaBH ₄	Sodium Borohydride
NH ₄ OH	Ammonium Hydroxide
FeSO ₄ .7H ₂ O	Iron (II) Sulphate
H ₃ PO ₄	Phosphoric Acid
HCl	Hydrogen Chloride
NaOH	Sodium Hydroxide

$\text{Na}_2\text{HPO}_4 \cdot 2\text{H}_2\text{O}$	Di-Sodium Hydrogen Phosphate Dihydrate
$\text{NaH}_2\text{PO}_4 \cdot \text{H}_2\text{O}$	Sodium Dihydrogen Phosphate
PBS	Phosphate Buffer Solution
CAT	Catalase
ZnO	Zinc Oxide
CPE	Carbon Paste Electrode
Cu_2O	Copper (I) Oxide
TiO_2	Titanium Oxide
AT	2-Amino-Thiazol
CTAB	Cetyltrimethylammonium Bromide
GNSP	Graphene Nano-Sheets
Meso- SiO_2	Meso-Silicon Dioxide
RGO-HDPPy	Reduced Graphene Oxide-Polypyrrole Nanospheres with Highly Dispersibility
$\text{K}_3[\text{Fe}(\text{CN})_6]$	Potassium Hexacyanoferrate (III)
GCE	Glassy Carbon Electrode
Pt wire	Platinum Wire
Ag/AgCl	Silver/ Silver Chloride Electrode
MRI	Magnetic Resonance Imaging
CVD	Chemical Vapor Deposition
ADHD	Attention Deficit Hyperactivity Disorder
RLS	Restless Legs Syndrome
HPLC	High Performance Liquid Chromatography
GC-MS	Gas Chromatography-Mass Spectrometry
CV	Cyclic Voltammetry
DPV	Differential Pulse Voltammetry

EIS	Electrochemical Impedance Spectroscopy
FESEM	Field Emission Scanning Electron Microscope
SEM	Scanning Electron Microscope
EDX	Energy-Dispersive X-ray Spectroscopy
TEM	Transmission Electron Microscope
HRTEM	High Resolution Transmission Electron Microscope
XRD	X-Ray Diffraction
UV-Vis	Ultraviolet-Visible Absorption Spectroscopy
PL	Photoluminescence Spectroscopy
VSM	Vibrating Sample Magnetometer
STM	Scanning Tunneling Microscope
SPM	Scattering Probe Microscopy
AFM	Atomic Force Microscopy

LIST OF PUBLICATIONS

Full-paper (ISI-cited)

1. **P.S. Teo**, A. Pandikumar, H.N. Lim, N.M. Huang, C. H. Chia. “Magnetically separable reduced graphene oxide/iron oxide nanocomposite materials for environmental remediation” *Catalysis Science & Technology* 2014. DOI: 10.1039/C4CY00806E
2. **P.S. Teo**, A. Pandikumar, N.M. Huang, H.N. Lim, Y. Sulaiman. “Simultaneous electrochemical detection of dopamine and ascorbic acid using iron oxide/reduced graphene oxide modified glassy carbon electrode” *Sensors* 2014 (14); 15227-15243.
3. F.A. Jumeri, H.N. Lim, S.N. Ariffin, N.M. Huang, **P.S. Teo**, S.O. Fatin, C.H. Chia, I. Harrison. “Microwave synthesis of magnetically separable ZnFe₂O₄-reduced graphene oxide for wastewater treatment” *Ceramics International* 2014(40); 7057-7065.
4. S.N. Ariffin, F.A. Jumeri, H.N. Lim, A.H. Abdullah, M. Ahmad, N.A. Ibrahim, N.M. Huang, **P.S. Teo**, K. Muthoosamy, I. Harrison. “Modification of polypropylene filter with metal oxide and reduced graphene oxide for water treatment” *Ceramics International* 2014(40); 6927-6936.
5. **P.S. Teo**, H.N. Lim, N.M. Huang, C. H. Chia, I. Harrison. “Room temperature in situ synthesis of Fe₃O₄/graphene” *Ceramics International* 2012(38); 6411-6416.

CHAPTER 1 : INTRODUCTION

1.1 Research background

1.1.1 Nanotechnology and Nanomaterials

Nanotechnology is a broad and interdisciplinary area of research and development activity that have been growing rapidly worldwide in the past and present decades. The prefix “nano” was come from the Greek word for “dwarf”. In 1974, the term “nanotechnology” was first given by a Japanese scientist, Prof Norio Taniguchi (University of Tokyo), which defined as the ability of the engineering materials precisely at the scale of nanometer, that is, in the size of range 1 to 100 nanometer (Kearnes et al., 2006). Till date, the evolved version of the “nanotechnology” is more properly deal with the design and fabrication of materials, devices and systems with control at nanoscale dimension and is used in an all-embracing sense as long they all share the common feature to control at the nanometer scale (Ramsden, 2005).

Nanomaterials are the materials with size or features ranging from 1 to 100 nm in at least one or more dimension. As compare to bulk materials, nanomaterials are said to be much more reactive as they possesses large surface area and high percentage of atoms at the surface. Thus, the physical and chemical properties of these nanostructure materials are distinctly different those of a single atom (molecule) and bulk material with the same chemical composition. Once formed, these nanostructures are extremely small and give rise to some interesting and intriguing properties of electrical, optical, structural, and electromagnetic of nanomaterials. Owing to their unique and beneficial physical, chemical and mechanical properties, nanomaterials have been received tremendous attention and exploited for wide-ranging applications in textile, drug delivery, energy storage system, cosmetics, microelectronics and healthcare. As results

from the advanced rapid innovation of nanomaterials synthesis, the increased invention of characterization tools and instrumentation to identify and measure these extremely small particles. The commonly used instruments such as Scanning Tunneling Microscope (STM), Scattering Probe Microscopy (SPM) and Atomic Force Microscopy (AFM) which allow to study the nanoparticles which could not visible in the conventional microscope (Ghorai, 2013; Lue, 2007).

One of the most important among these nanoscale materials are nanocomposites. Generally, nanocomposite is a combination material created from two or more components at nanometer length scale, or else nanocomposite can be defined as a multiphase solid material where one of the phases has one, two or three dimensions and amorphous materials, made of distinctly dissimilar constituents and mixed at the nanoscale. The properties of nanocomposite materials are not depend only of their individual parents, but also on their morphology and interfacial characteristics. By combining the properties from the parent components into a single material, it could lead to generate new exciting materials with novel properties when compared to conventional microscale counterparts. Therefore, the unique and improved properties of nanocomposite gained number interests of researchers and promising for utilize in a variety of industrial applications (Rao et al., 2001).

1.1.2 Overview of Graphene

In 2004, graphene was first discovered and exfoliated mechanically from graphite by physicists from the University of Manchester, Novoselov, Geim and co-workers (Novoselov et al., 2004). Afterwards, Geim and Novoselov awarded the Nobel Prize in Physics for “groundbreaking experiments regarding the two-dimensional material graphene” (Geim et al., 2007).

Graphene is a planar monolayer of sp² bonded carbon atoms densely packed into a two-dimensional (2D) honeycomb lattice structure (Rao et al., 2009). Since graphene was first isolated from graphite, it had attracted a great number of interests from researchers. The elusive 2D structure of graphene possesses numerous outstanding properties, where it has a large theoretical specific surface area (2630 m²g⁻¹) (L. Zhang et al., 2010), offer mobility of charge carriers at room temperature (200,000 cm²v⁻¹s⁻¹) (Vlassiouk et al., 2011), exceptional thermal conductivity (5000 W m⁻¹ K⁻¹) (Balandin, 2011), and exhibit superior mechanical properties with Young's modulus (1Tpa) (Y. L. Liu et al., 2012). Besides, as a zero band gap semiconductor, the electrons and charge carriers in graphene behave like massless relativistic particles under ambient condition, resulting unexpected electronic properties such as anomalous quantum Hall effect and transport via Dirac fermions (Novoselov et al., 2007). As a result, these extraordinary properties of graphene make it considered as a “rising star” carbon material to have great potential in a number of interesting fields, including sensors, solar cells, energy storage and nanocomposites.

However, the aggregation problem of graphene sheets when dissolved in solvents could limit its applications. Therefore, graphene fabrication process is an important step to develop new, simple and low budget processing routes for efficiently producing the large-scaled graphene as the graphene synthesized defines its properties and may offer valuable insights into future applications. To date, various synthesis routes of graphene have been reported, which can be broadly divided into two categories: physical methods and chemical methods. However, some of the reported methods have some disadvantages, including low yield, limitations of instruments and high energy requirement. In this investigation, the chemical method is chosen for graphene synthesis because of it simple, inexpensive, versatile and available for large scaled production. Generally, this method consists of three important steps: graphite

oxidation, exfoliation of graphite oxide, and reduction of graphene oxide sheets. Initially, the bulk graphite will undergo chemical oxidation to become hydrophilic graphite oxide (GO). The graphite oxide is then exfoliated into monolayer or few-layered stacks of graphene oxide. Lastly, graphene oxide is reduced to graphene through reduction process.

1.1.3 Overview of Iron Oxide

Iron oxides are being one of the most abundant minerals and have a widespread occurrence in the Earth's crust as they have been utilized for over 30,000 years. Based on Cornell and Schwertmann, most of the iron oxides are in trivalent state of iron, low solubility and exhibit in good crystalline structure, except for ferrihydrite and Schwertmannite.

Basically, iron oxides can exist in variety of structures and phases in nature, ranging from oxides, oxyhydroxides and hydroxides. Six phases forms of iron oxides can exist at the ambient pressure condition; including magnetite Fe_3O_4 , wustite FeO and Fe_2O_3 ($\alpha\text{-Fe}_2\text{O}_3$, $\gamma\text{-Fe}_2\text{O}_3$, $\beta\text{-Fe}_2\text{O}_3$ and $\varepsilon\text{-Fe}_2\text{O}_3$). Among of these ferrous and ferric oxides, Fe_3O_4 (magnetite), $\alpha\text{-Fe}_2\text{O}_3$ (hematite), $\gamma\text{-Fe}_2\text{O}_3$ (maghemite) and FeO (wustite) are more common and being studied due to their amazing properties exhibit at nanoscale. Furthermore, these iron oxides display strong magnetic properties in nature, and thus the surface enhancement and functionalization of these magnetic oxides at nanometric dimensions are therefore subjected to many technological applications, including biomedical, catalysts, batteries, magnetic resonance imaging agents (MRI) and biosensing (Cornell et al., 2003). Various types of iron oxides are summarized in **Table 1.1** (Mohapatra et al., 2010).

Table 1.1: Various types of iron oxides (Mohapatra & Anand, 2010).

Oxides	α -Fe ₂ O ₃ ; Hematite Fe ₃ O ₄ ; Magnetite γ -Fe ₂ O ₃ ; Maghemite β -Fe ₂ O ₃ ϵ -Fe ₂ O ₃ FeO; Wustite
Oxide-hydroxides	α -FeOOH; Goethite γ -FeOOH; Lepidocrocite β -FeOOH; Akagetite Fe ₁₆ O ₁₆ (OH) _y (SO ₄) _z .nH ₂ O; Schwertmannite δ -FeOOH δ' -FeOOH; Feroxyhyte FeOOH (High pressure) Fe ₅ HO ₈ .4H ₂ O; Ferrihydrite
Hydroxides	Fe(OH) ₃ ; Bernalite Fe(OH) ₂ Fe _x ⁱⁱⁱ Fe _y ⁱⁱ (OH) _{3x+2y+z} (A ⁺) _z [A ⁺ =Cl ⁻ ; 0.5 SO ₄ ²⁻]; Green rust

1.2 Research problems and motivations

In this regard, graphene has been brought into sharp focus largely due to its fascinating and enhanced functionalities in a wide variety of applications. However, the individual graphene sheets tend to irreversibly aggregate or restack to form graphite through the strong π - π stacking and van der Waals interactions between the planar basal planes of graphene sheets. The serious aggregation inevitably hinders the active catalytic sites and subsequently hampers the catalytic activity of graphene. Furthermore, there is an unavoidable problem associated with the magnetic iron oxide nanoparticles, which is their intrinsic instability over long period of time. The magnetic iron oxides are chemically active, unstable under ambient conditions and easily oxidized

in the air. The oxidation of iron oxides can be correlated with the migration of cations through their lattice framework to maintain the charge balance by creating cationic vacancies. However, a number of factors such as pH range in aqueous solution, temperature, concentration of dissolved oxygen and ionic strength also highly contributed to the oxidation rate of iron oxides. Besides, they exhibit high energies owing to the large surface-to-volume ratio, thus they are prone to agglomeration, especially in the large scale synthesis; resulting in the loss of magnetism and dispersibility. Therefore, it is crucial to develop an effective strategy for magnetic nanoparticles synthesis that not only stabilize the nanoparticles but also can utilize for wide range of potential fields.

To solve these serious problems, recently, graphene-based metal oxide nanocomposites have attracted great attention due to the synergistic effects between two or more functional components. In such composite system, the magnetic nanoparticles act as stabilizer against the aggregation of individual graphene sheets because of the strong van der Waals force between graphene layers, and consequently keeping property of high active surface area graphene. On the other hand, graphene act as support for magnetic particles to prevent agglomeration and effectively reduce the size of magnetic particles. Nanocomposite of graphene and magnetic nanoparticles exhibit the beneficial properties of each parental constituents, producing a material with novel physicochemical properties and enhanced catalytic performance which widely investigated in the field of catalysis and sensor platforms.

Graphene-based magnetic nanomaterial composites have been intensively explored in environmental remediation to prepare the photocatalytic composite with enhanced performance. Peng et al have reported that carbon nanotubes-iron oxides composites as an adsorbent which displayed their good adsorption ability for the

removal of pollutants from water due to their large specific surface area. However, one of the major drawbacks from this adsorption method is that the contaminants only transfer from one phase to another, thus it is not destructive and deemed require further treatment process. A newly alternative to this conventional method, combination of adsorption and photocatalytic degradation was introduced for the efficient removal of toxic pollutants. During the adsorption-photodegradation, the contaminants in wastewater were firstly in-situ adsorbed onto the adsorbent, consequently the adsorbent was photocatalytically oxidized under irradiation and can be reused for the further adsorption cycles. Fu et al have reported that ZnFe_2O_4 -graphene nanocomposite successfully prepared by one-step hydrothermal method showed high photocatalytic performance under visible light irradiation. Ma et al synthesized $\text{Fe}_3\text{O}_4/\text{TiO}_2/\text{rGO}$ composite with a hydrothermal route and found its enhanced photocatalytic activity under sunlight. Furthermore, magnetic graphene composite also has been proved to become an active area and apply for electrochemical sensing or biosensing purposes. Zhu et al reported an electrochemical sensor for hydrogen peroxide (H_2O_2) at $\text{Fe}_3\text{O}_4/\text{rGO}/\text{GC}$ electrode. Magnetic nanoparticles (MNPs)/rGO/GCE was developed by Zhang et al displayed excellent catalytic activity for bisphenol A (BPA) detection. H. Teymourian et al studied the voltammetric detection of electroactive compounds (H_2O_2 , NADH, nitrite, dopamine (DA), uric acid (UA) and ascorbic acid (AA)).

1.3 Research objectives

The objectives of this study are:

- I. To synthesize iron oxide/reduced graphene oxide ($\text{Fe}_3\text{O}_4/\text{rGO}$) nanocomposite with good characteristics *via* a simple and eco-friendly, in-situ chemical synthesis approach at room temperature.

- II. To study the physical and chemical properties (i.e. morphology, magnetic, electrochemical) of as-synthesized nanocomposites.
- III. To investigate the photocatalytic performance of nanocomposites under natural solar light irradiation towards degradation of methylene blue (MB) in wastewater.
- IV. To study the inference effect of ascorbic acid (AA) on the electrochemical sensing of dopamine (DA) by using modified $\text{Fe}_3\text{O}_4/\text{rGO}$ glassy carbon electrode ($\text{Fe}_3\text{O}_4/\text{rGO}/\text{GCE}$).

1.4 Thesis outline

This research work on this dissertation consists of five chapters. This work focuses on the synthesis of iron oxide/reduce graphene oxide ($\text{Fe}_3\text{O}_4/\text{rGO}$) nanocomposite, characterization and utilized for the study of photocatalytic activity of $\text{Fe}_3\text{O}_4/\text{rGO}$ nanocomposites as well as the electrochemical determination of dopamine in the presence of high concentration of AA. A brief overview of the chapters is given as following:

Chapter 2: Literature Review

In this chapter, the literature review of this research work, including the background and reason for selecting graphene and iron oxide (Fe_3O_4), the intriguing and improved features of as-synthesized $\text{Fe}_3\text{O}_4/\text{rGO}$ nanocomposite and the proposed fabrication route for magnetic graphene composite. Lastly, the chapter will end up with discussed the performance of nanocomposite in application of photocatalysis and electrochemical detection of biological molecules.

Chapter 3: Experimental Details

This chapter introduced the reliable pathway for preparation of GO and Fe₃O₄/rGO nanocomposites. Various characterization tools that employed to define the nanocomposite characteristics are also presented. At last, the photocatalytic and electrochemical measurements of the obtained Fe₃O₄/rGO are described.

Chapter 4: Results and Discussion

This chapter explores the result obtained from analytical techniques for the characterization studies of structural, morphological and electrochemical of magnetic graphene composite. In addition, the performance of Fe₃O₄/rGO as photocatalyst for MB degradation under natural sunlight irradiation also investigated. Furthermore, the selectivity and sensitivity of Fe₃O₄/rGO modified electrode sensor for dopamine in the presence of acid ascorbic will be demonstrated.

Chapter 5: Conclusion and Future Works

This chapter included the achievement of the objectives, brief description of its influence in the real industry communities and suggestions for future research are discussed too.

CHAPTER 2 : LITERATURE REVIEW

2.1 Introduction

This chapter describes the introduction of the research background and purpose of the present study. In this chapter, the discovery, properties and synthetic methods of the graphene will be briefly described. Besides, details of the super-paramagnetic nanoparticles (Fe_3O_4) and synthesized $\text{Fe}_3\text{O}_4/\text{rGO}$ are presented. Moreover, the improvement in the photocatalytic activity and pathway towards the MB degradation of the magnetically separable $\text{Fe}_3\text{O}_4/\text{rGO}$ nanocomposite are included. Finally, the electrocatalytic performance for the simultaneous determination of DA and AA is addressed and reviewed.

2.2 Graphene

Graphene is defined as a two-dimensional (2D) crystalline material, consists of a single layer of sp^2 hybridized carbon atoms tightly arranged in a hexagonal honeycomb network. The one-atom-thick graphene is considerable as a basic building material for graphitic materials of all dimensionalities, such as carbon nanotubes and fullerenes. Meanwhile, it can be wrapped into 0D buckyballs, rolled into 1D carbon nanotubes or stacked up to form the 3D graphite (**Figure 2.1**). In 1987, the term “graphene” was first appeared in description of single sheets of graphite as a constituent of graphite intercalation compounds (GICs), however, the term “graphene” was firstly named studied by Hanns-Peter Boehm in 1962, who studied the single layer carbon foils. In 2004, the creation of graphene was discovered and investigated by two Russian born scientists at the University of Manchester, Andrei Geim and Kostya Novoselov and their co-researchers, in an attempt to explore the electrical properties of graphene by extracted the single layer-atomic-thick crystallites from highly oriented pyrolytic graphite (HOPG) with the help of sticky ‘Scotch tape’. In 2010, Geim and Novoselov

won and awarded the Nobel Prize in Physics for their ground-breaking experiments with 2D graphene. Since the potential applications for superlattice graphene appeared to be unlimited, hence it emerged as fascinating nanomaterial in stimulating and fosters both scientific discovery and its commercial exploitation in a variety of areas nanotechnology (Novoselov, 2011).

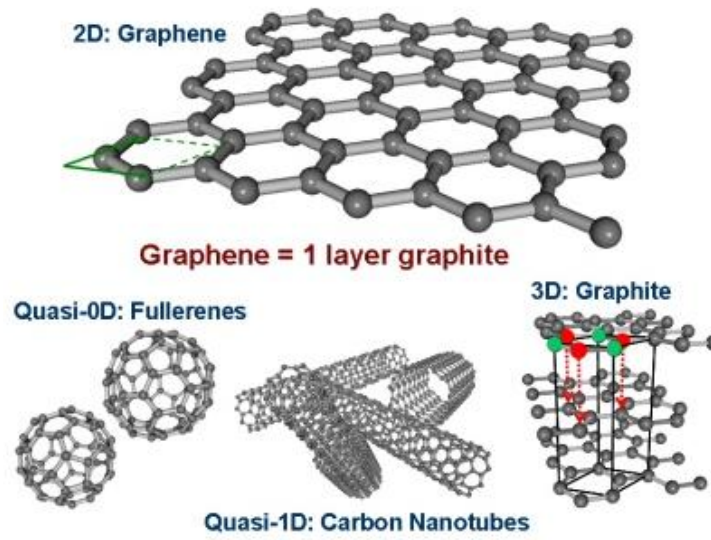


Figure 2.1: Graphene as a basic building block for all graphitic dimensionalities (Seyller, 2011).

2.2.1 Properties of Graphene

The single layer of hexagonal lattice graphene is composed of two equivalent sub-lattices of carbon atoms that bonded with σ bonds, and separated by carbon-carbon distance of 0.142 nm. The electronic configuration of graphene defined as $1s^2 2s^2 2p^2$, while the $2s^2 2p^2$ configuration from the outer shell can hybridize to form different hybrid orbitals which consequently leading to different forms of carbon materials (Deshmukh et al., 2011). The adjacent graphene sheets holds together by weak van der Waals interactions and hence enables graphene sheets slide with respect to each other, give rise to its soft and lubricating properties.

The hexagonal lattice arrangement of graphene is a result of the sp^2 hybridization and interaction between π orbital of each carbon atoms in the lattice allows delocalization of electrons within graphene sheets. These highly mobile electrons are located above and below the graphene sheets. The free unoccupied p-orbitals ($2p_z$), which is perpendicular to the 2D planar structure graphene play important role in the electronic properties of graphene. These unaffected p-orbitals can bind covalently with the neighboring carbon atoms to form the π -band (**Figure 2.2**) and results the existence of exceptional properties of graphene. Hence, the 2D honeycomb lattice of graphene reflected in its remarkable electrical conductivity properties.

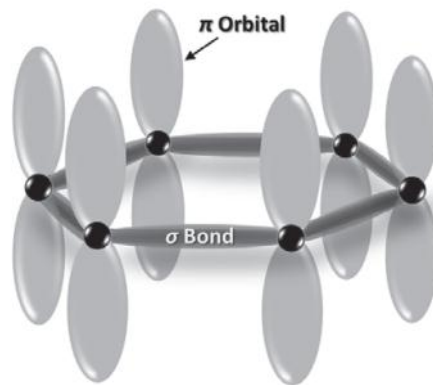


Figure 2.2: The sp^2 hybridization between carbon atoms and formation of π bonds from the unoccupied p-orbital (Ul Hasan, 2012).

Owing to the small overlap between the bonding and anti-bonding (valence and conduction bands) makes graphene exhibits semiconductor behaviour. As a zero band-gap semiconductor, graphene possesses high electron mobility up to $250\,000\text{ cm}^2\text{ V}^{-1}\text{ s}^{-1}$ under ambient temperature (Bolotin et al., 2008). Graphene electrons moves very much like photons in their mobility due to their lack of mass. At the Fermi level, the electrical conductivity of intrinsic graphene is relatively. However, the Fermi level of a material is depend on the polarity of the applied field, thus, the electrical conductivity graphene changed becomes either n-type (with electrons) or p-type (with holes) when applied an

electric field. The electron mobility is nearly or weakly independent on temperature, indicating the importance of graphene as electron carrier in both electrical and chemical applications that involves electron transfer process including sensors, catalysts and supercapacitors. Furthermore, the Dirac point in zero-overlap graphene, electrons and holes (also known as Dirac fermions) are zero effective mass, ascribed to the low energy excitation. The electronic conductivity is relatively low due to the zero density states at the Dirac points and is unparalleled at room temperature. However, the Fermi level can be altered depending on the polarity of the applied electric field by doping (electrons or holes) to create a better and potentially conducting electrical material (Neto et al., 2009). Due to graphene's tunable band gap, bi-layer graphene was changed from a conductor to a semiconductor in the applied electric field.

Apart from the intriguing electronic properties of graphene, the 2D planar graphene material demonstrates a variety of marvelous properties, for instance large theoretical specific surface area ($2630 \text{ m}^2 \text{ g}^{-1}$) (Cranford et al., 2011). In addition, high thermal conductivity of graphene ($\sim 5000 \text{ W m}^{-1} \text{ K}^{-1}$) (Balandin et al., 2008) allows it portrays excellent thermal stability, which is important in the electronic devices including lithium-ion batteries (LIBs). Further, the inherent strength of sp^2 C-C covalent bonds in graphene lattice contributes the mechanical properties with Young's modulus of 1 TPa (Y. L. Liu et al., 2012). These superior properties make graphene as the strongest material and perfect choice for transparent or flexible electrodes for electrochemical energy conversion. Graphene also displays extraordinary optical transparency characteristics (Bae et al., 2010), as it only has 2.3% opacity in its hexagonal planar surface, thus graphene is almost completely transparent. The graphene opacity of 2.3% is found to be equates to the universal dynamic conductivity (G) = $e^2/4\hbar$ (1.01 ± 0.04) over the visible frequencies range, which is the behaviour for ideal Dirac fermions (Nair et al., 2008). Besides, the reported optical transmittance of

mono and bilayer graphene is found to be around 98 and 96 % in the visible range. In summary, the unique and interesting properties arise from graphene open new existing possibilities to develop new multi-functional nanomaterials, for instance, graphene-based composites involving conductive polymer, transition metal oxides and noble metals as attractive candidate for fundamental science and near future applications.

2.2.2 Methods for Graphene Synthesis

The synthetic process of graphene is a crucial step to be noted as the yield graphene defines and highly dependent on the optimum properties exhibited by graphene are relevant at nanoscale for all potential applications. Up to date, there are dozen preparing graphene sheets routes have been developed and reported. Generally, the graphene synthesis methods are including mechanical exfoliation in solutions, chemical vapor deposition (CVD), epitaxial growth of graphene layers on silicon carbide (SiC), chemical reduction of graphene oxide (GO), and intercalation technique.

Mechanical exfoliation is a simple peeling process firstly used by Geim and coworkers to obtain both mono and few layer graphene by micromechanical exfoliation of highly oriented pyrolytic graphite (HOPG) with scotch-tape. Thus, it is also known as ‘Scotch tape’ or peel-off method. The repetitively peeling of HOPG with adhesive tape produced the highest quality of thin flakes in the range of 10 μm , which were composed of monolayer or a few layers of graphene. This approach however is limited neither by its high throughput nor high yield, and hence it is only suitable for fundamental study in laboratory.

Chemical vapor deposition (CVD) also one of the most promising method for bulk quantities production of monolayer or few layer of graphene films. In 2006, Somani and coworkers successfully synthesis the few layer graphene films via CVD using camphor as the precursor on Ni foils (Somani et al., 2006). Typically, CVD process involving the

utilization of transition metal surfaces as substrate for growth of graphene and the use of diluted hydrocarbon gasses as graphene precursors at a vacuum of 10^{-3} Torr and temperature about 1000 °C. However, the process is expensive due to the energy consumption and removal of the underlying metal layer. Thus, a number of progress need to be resolved for the development of graphene growth on the arbitrary at low temperature with a reduced number of defects to avoid the complex and expensive transfer process and promote better integration of graphene with the alternatives (like Si or GaAs) that significant for energy saving (Reina et al., 2009).

Epitaxial growth of graphene on SiC is one of the substrate-based methods of graphene synthesis. This approach is efficiently for the synthesis of uniformly, wafer-size graphene layers and required no transfer process. However, there are several hurdles impedes the production, for instance, controlling the thickness graphene layers in the large surface area graphene and the unusual epitaxial growth patterns were observed in multilayers graphene on different SiC polar face (Si-face or C-face). Another drawbacks of this method are the high cost of the SiC wafers as well as the requirement of high temperature (above 1000 °C) and high vacuum would probably limit its niche applications (Deng et al., 2010; Varchon et al., 2007).

Chemical exfoliation is a two process step that achieved by introducing external forces to overcome the adjacent van der Waals interactions between layers in bulk graphite. Several efforts are attempt to weaken these strong attractions, for instance, expanding the distance of 3.4 Å between graphitic layers through oxidation and chemical intercalating small molecules (i.e. alkali metal ions or acid molecules) to prepare graphene-intercalated compounds (GICs). Consequently, thermal and ultrasonication treatment are introduced for exfoliation of GICs into single or few layers of graphene. Additionally, solvents such as dimethylformamide (DMF) and *N*-methyl-2-

pyrrolidone (NMP) are widely used in liquid immersion techniques to facilitate the exfoliation of graphite in reducing the strength of the van der Waals.

One of the most suggested and viable route evaluated to produce the low cost, considerable and large quantities of bulk graphene, namely chemical reduction of graphene oxide (GO). This two-step approach involves chemically oxidation of graphite to graphene oxide and subsequently chemically reduction of GO graphene using reducing agents. Graphene oxide (GO) is the oxygenated form of a monolayer graphene sheet, which possess large surface area and excellent mechanical properties. The surface of GO is heavily decorated with oxygen-containing functionalities such as hydroxyl and epoxy groups on sp^3 hybridized on the basal carbon plane, while carbonyl and carboxyl groups attached at the edges sheets of sp^2 hybridization carbon. These surface reactive oxygenated functional moieties on carbon sheets are highly hydrophilic and hence GO is readily dispersible in a wide range of polar organic solvents in ultrasonication to yield stable dispersion of single layered sheets GO, as well as provide a better surface affinity during the fabrication nanocomposites process, in the comparison with the hydrophobic pristine graphene. The dispersibility basically depends on the polarity of the surface. The exfoliation of multilayer system graphitic oxide in water through ultrasonication, eventually yielding single or few layered graphene, namely graphene oxide (GO). However, graphene oxide is structurally different with graphitic oxide, attributed to the number of layers, although they shared similar chemical properties owing to the surface functionalities.

Due to the rich of the chemically reactive oxygen functionalities surface of GO and its capable dispersibility in most organic solvent and water, as well as in the variety of surface-modification reaction for development of functionalized graphene oxide materials, and hence GO easy to process and proven to be utilized as precursor or

starting material for a wide range of applications. However, GO is electrically insulating and consists of irreversible defects owing to the disruption of the conjugated electronic structure (Bourlinos et al., 2003). Chemical reduction of graphene oxide involves two reaction steps. Firstly, graphene oxide is prepared through the chemical oxidation of graphite by reacting with strong oxidants *via* Hummers method. The mixture of potassium permanganate (KMnO_4) and concentrated sulfuric acid (H_2SO_4) and nitric acid are well known as strong oxidizing agents, which act as reactive species treated in the reaction with aromatic region surfaces of graphite as well as achieving the levels of oxidation (Lakshminarayanan et al., 2004). Subsequently, GO is chemically reduced to graphene with reducing agents such as hydrazine, sodium borohydride (NaBH_4) and sugar. The changes of brown colour dispersion graphene oxide into black reduce graphene oxide (rGO), mainly due to the removal of oxygen groups and hence hydrophobic nature of rGO is aggregated and precipitated (Stankovich et al., 2007; S. Stankovich et al., 2006). Recently, chemical functionalization of graphene with polymers, surfactants and organic molecules provides repulsive steric interactions between exfoliated sheets and therefore, allows the formation of stable colloidal graphene suspension and preventing restacking or aggregation of rGO sheets (Coleman, 2009; Oyer et al., 2012).

2.3 Magnetite (Fe_3O_4)

Iron oxides are one of the elements may exist in rich a variety forms of structures in nature. Magnetite (Fe_3O_4), maghemite ($\gamma\text{-Fe}_2\text{O}_3$) and hematite ($\alpha\text{-Fe}_2\text{O}_3$) are the most probably common iron oxides being widely studied and investigated by chemists, engineers and physicists. Hematite ($\alpha\text{-Fe}_2\text{O}_3$), is known as the oldest iron oxide found from 80,000 years ago and is widespread in rocks and soils. Sometimes, the brown reddish hematite is also known as ferric oxide, red ochre, or kidney ore. Hematite

exhibits in rhombohedral lattice system and stable at ambient temperature. Maghemite is brown or brick-red in colour and formed by weathering oxidation of magnetite or titanian magnetite. Maghemite, the oxidized form of magnetite is a spinel ferrite and has a same spinel structure as magnetite and is widespread in continental sediments, rocks and soils. However, it is metastable in comparison with hematite (Chirita et al., 2009; Sahoo et al., 2010).

Magnetite, the black iron oxide consists of Fe^{2+} and Fe^{3+} and represented with the formula $\text{FeO}\cdot\text{Fe}_2\text{O}_3$ becomes the main focus and gains great interest of iron oxide in the present study. It is a narrow band gap semiconductor, with the photon energy region 0.1 eV and 3 eV for temperature between for between 77 K to 300 K, which contributes to its unique electrochemical properties among the iron oxides (Buchenau et al., 1972). In general, the crystal structure of these three iron oxides are arranged in a close-packed planes of oxygen anions with iron cations either in octahedral or tetrahedral interstitial sites. Magnetite has an inverse spinel structure with a face-centered cubic lattice in the length of 0.839 nm for each unit cell (Fonin et al., 2005; Y. L. Li et al., 2007). Unlike the maghemite, vacancies in the cations sublattice, Fe^{3+} ions are randomly distributed between the octahedral and tetrahedral sites, while the Fe^{2+} ions located in octahedral sites (**Figure 2.3**) (Ketteler et al., 2001; Klotz et al., 2008). In the inverted cubic spinel structure of magnetite, one third of Fe^{3+} ions are occupy tetrahedral *A* sites, while octahedral *B* sites contain the equal numbers of Fe^{3+} and Fe^{2+} ions, respectively.

Magnetite is the archetype mixed valent *3d* transition metal compound, thus it is a half-metallic ferromagnet at room temperature, possessing 100% spin polarized charge carriers at the Fermi level (E_f) and expected to be metallic at high temperature as the half-filled Fe *3d* bands associate with *B* sites. Due to its magneto-optical properties, Fe_3O_4 nanoparticles have been studied and intensively developed into the optical

application such as optical switches (Chieh et al., 2010). Shauo et al. successfully the magnetite nanoparticles that showed excellent absorption in ultraviolet region and good transmittance in visible region, suggesting the unique magnetic properties and favorable optical properties of magnetite have great potential for use in optical applications (Shauo et al., 2007). On the other hand, Milichko et al. have demonstrated a co-precipitation of spherical Fe_3O_4 nanoparticles with a wide nonlinear absorption band of visible radiation (1.7:3.7 eV) which can effectively change their electric polarizability in a low intensity visible radiation ($I \leq 0.2 \text{ kW/cm}^2$) (Milichko et al., 2013). However, there is limited review literatures reported on the band gap of magnetite nanoparticles, thus the optical parameters of magnetite including optical energy band gap were conducted in the form of magnetic fluid (MF). Ghandoor et al. reported that the particles size of magnetite is inversely proportional to their energy band gap (El Ghandoor et al., 2012).

Magnetite exhibiting the Verwey metal-insulator transition where spontaneous intercorrelated change occur in both the lattice symmetry and electric conductivity, for instance, transformation from cubic spinel to monoclinic structure at the Verwey transition ($T_v = 110\text{-}120 \text{ K}$). Above the Verwey transition temperature, electron hopping occurs between Fe^{3+} and Fe^{2+} ions in octahedral sites, give rise to a half metallic behaviour that mediate the high room temperature conductivity of magnetite. However, the inhibition of electron hopping and reduction in conductivity happened when below the T_v (S. Park et al., 1998).

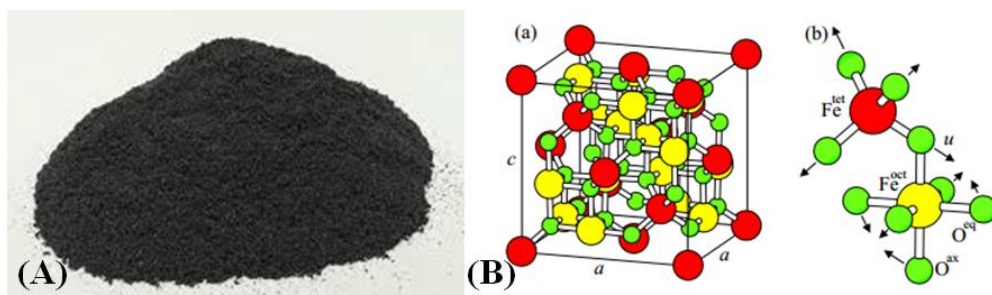


Figure 2.3: (A) Photographic image of magnetite (Fe_3O_4) and (B) the cubic spinel structure of magnetite (Friak et al., 2007).

2.3.1 Magnetic properties of Magnetite (Fe_3O_4)

Recently, the increasing considerable attention and extensive study of the magnetic nanoparticles mainly related to their specific magnetic properties that differentiate them from that exhibited bulk materials. However, it is crucial to noted that the key factors such as size, morphology, structure of nanoparticles, enhanced surface effects as well as inter-particle interactions greatly influence the magnetic behaviour of iron oxides including magnetization, coercive field, magnetic susceptibility and magnetic transition temperature.

Magnetism or magnetic effects of a material arises from the alignment of the electron spin. The movements of spinning electric-charged particles (electrons, holes, protons, positive and negative ions) with both mass and electric charges may subsequently create a magnetic dipole, so called magneton. Thus, the magnetism of materials can be classified to five basic types of magnetism namely paramagnetism, diamagnetism, ferromagnetism, ferrimagnetism and anti-ferrimagnetism, respectively by their responses to an external applied magnetic field as well as the orientation of the magnetic moments in materials (Teja et al., 2009).

Magnetite is a ferrimagnetic material at room temperature and has a Curie temperature of 850 K. It exhibits the strongest magnetism of any transition metal oxide

and is a naturally occurring mineral on earth. The unique electronic and ferrimagnetic properties of magnetite originate from the active electrons in the $3d$ orbitals (unpaired electron spins). For a ferrimagnetic material, below the Neel temperature, the neighboring atoms or ions are tending to align in non-parallel arrangement under a zero applied field. Below the Curie temperature, magnetite aligns in uneven coupling with the spin arrangement of $\text{Fe}^{3+}\downarrow [\text{Fe}^{3+}\uparrow\text{Fe}^{2+}\uparrow] \text{O}_4$ (Gu et al., 2004; Jeong et al., 2007).

Superparamagnetism is a form of magnetism, which probably occurs in the small enough nanoparticles that have single magnetic domain. Below a critical particles size of magnetite (i.e. 15 nm), the nanoparticles have a zero coercivity and no hysteresis due to the spontaneously demagnetization by thermal fluctuations. Therefore, superparamagnetic nanoparticles tend to align along the magnetic field and become magnetic in the presence of an applied external magnetic field, but revert to nonmagnetic or retain no magnetization after removal of the external field (**Figure 2.4**) (Rockenberger et al., 1999). The superparamagnetic behaviour of magnetite is preferred and successfully offers a high potential for all sorts of biological and biomedical applications of drugs delivery (Dorniani et al., 2012), magnetic resonance imaging (MRI) (D. K. Kim et al., 2001) and tumor hyperthermia (Pankhurst et al., 2003) as their magnetic properties can be easily manipulated upon the application of an external magnetic field.

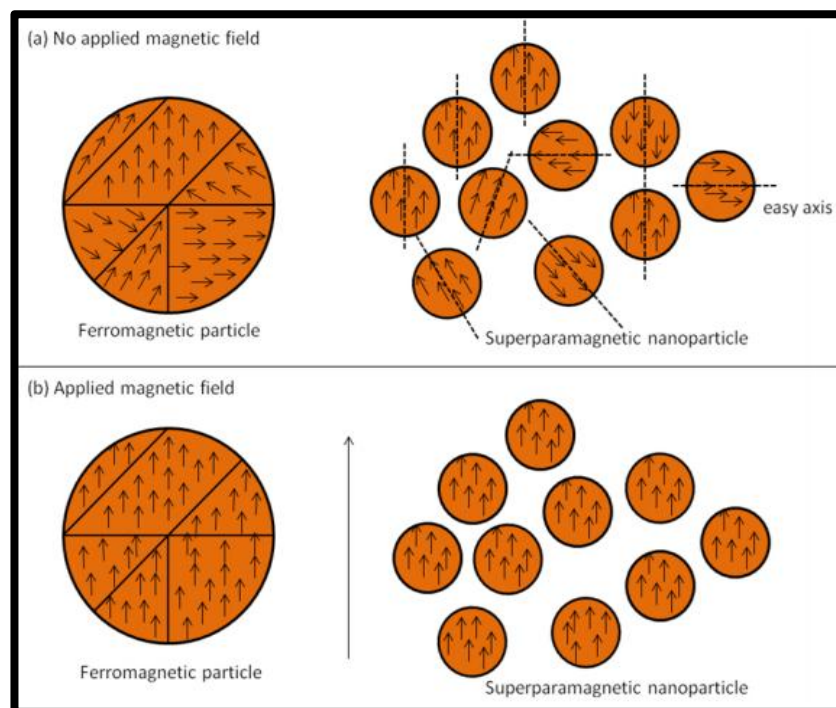


Figure 2.4: Superparamagnetic particles versus ferromagnetic particles in (a) presence and (b) absence of external magnetic field (Demas et al., 2011).

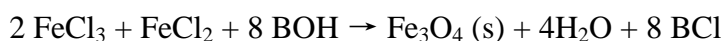
In the particular applications of biology, therapy and medical diagnosis, the nanoparticles must be stable at a pH of 7 in water or physiological environment. Besides, the nanoparticles must be non-immunogenic, possess high effective surface area, lower sedimentation and exhibit improved tissular diffusion to prevent vessel embolism, allow the binding and delivery of targeted drugs or biomolecules to a specific area by entrapment, adsorption or covalent interaction; to remain in the circulation or pass through the capillary system after an injection (J. N. Park et al., 2005; Puntès et al., 2001; Thorek et al., 2006). Moreover, the nanoparticles must have high field irreversibility and high magnetization to control their movement in blood system with an external field (Lopez-Quintela et al., 2004). Therefore, the fascinating properties including biocompatibility, non-toxic, high chemical stability, large surface area, superparamagnetic nature and easy surface modification of magnetite became a

great importance for magnetite nanoparticles to make them as promise candidate in the biological and biomedical applications.

2.3.2 Synthetic Methods for Magnetite (Fe₃O₄)

Suitable method for the magnetite preparation is a key factor that highly influence and determines the fascinating properties of synthesized iron oxides in their potential applications. Up to date, a great number of efforts devoted on the routes for the magnetic nanoparticles preparation have been developed to obtain the highly stable, nanosized and shape controlled, narrow size distribution, good crystallinity and strong magnetic nature of magnetic nanoparticles. Co-precipitation, hydrothermal, solvothermal, sol-gel, microemulsion, sonochemical, microwave-assisted and electrochemical methods are some popular synthetic pathways usually utilized.

Co-precipitation is the most convenient and facile method used for the synthesis of the black magnetic iron oxide from mixture aqueous salt solution. This precipitation method involves mixing of ferrous (Fe²⁺) and ferric (Fe³⁺) ions in a 1:2 molar ratio at room temperature or at elevated temperature with alkaline solution. The overall chemical reaction is shown as below, where BOH refers to different bases, B = Na⁺, K⁺, or (C₂H₅)₄N⁺ (Mascolo et al., 2013):



Moreover, the key factor such as ionic strength of the media, Fe³⁺/Fe²⁺ ratio, pH value, reaction temperature, mixing rate as well as the types of the salt used are very much affect the formation of nanosized iron oxide particles. However, the generated iron oxide particles from this pathway have a wide particle size distribution, unstable, easily oxidized to maghemite in the air or tend to agglomerate, and hence to control the synthetic parameters, addition of surfactants or stabilizers and bubbling of nitrogen gas

are advisable to generate good crystallinity and stabilized magnetite nanoparticles (Ahn et al., 2012).

The water in oil (W/O) microemulsion defined as a thermodynamically stable single phase system dispersion that consists of two immiscible phase in the presence of surfactant that commonly used in the synthesis of uniform sized superparamagnetic nanoparticles. The introduction of surfactant in the mixture system is to lower the interfacial tension between water and oil, contributes to the formation of a transparent solution. Despite of the addition of surfactants, stabilization treatment process using stabilizers in the fabrication is necessary to impede the aggregation of the obtained nanoparticles. However, a drawback of this synthetic pathway is the requirement of large amount volume of solvent is needed, but with a low quantity of yield generated (Lu et al., 2013).

Hydrothermal, so called solvothermal is an efficient and environmentally friendly route for preparing the highly crystalline, ultrafine and pure black magnetite particles. This reaction system requires performing in an aqueous media in reactors or autoclaves with pressure and temperature higher than 200 psi and 200 °C, respectively. However, hydrothermal method has slow reaction kinetics at any given temperature. Thus, combination of microwave-hydrothermal method is introduced to increase the kinetics of crystallization for the fabrication of better crystallinity and high purity of magnetic nanoparticles (Kholam et al., 2002; H. Zhang et al., 2012).

Sonochemical method is usually used to synthesize highly monodisperse nanosized materials with attractive properties in a short period reaction time, arises from acoustic cavitation phenomenon. The sonochemical synthesis of magnetite involves the ultrasonication of mixture containing Fe(II) or Fe(III) complexes or irons salts under an

inert atmosphere and eventually resulting narrow particle size distribution of final product (S. M. Zhu et al., 2013).

2.4 Magnetite/reduced graphene oxide ($\text{Fe}_3\text{O}_4/\text{rGO}$) nanocomposites

A nanocomposite is a combination comprises of at least two or more components of distinctly different nature and mixed at the nanometer scale. The new hybrid material exhibits unusual and improved combination properties that are not found in the parent constituent materials. These uniqueness and superior properties of nanocomposites mainly can attribute to interface interaction between the two phases are maximized. Owing to the excellent characteristics of graphene, it emerged as an attractive candidate substrate for the graphene-based nanocomposite and successfully stimulated immense attention in the field of material science. Magnetite, itself exhibits ferromagnetic properties at room temperature, biocompatibility and nontoxicity making them attracted for a variety of applications. The incorporation of graphene with magnetite particles liberates a functional hybrid material that give rise to new and enhanced functionalities which possesses complementary behaviour between each constituent. Magnetite/reduced graphene oxide ($\text{Fe}_3\text{O}_4/\text{rGO}$) nanocomposites not only showed favorable magnetic nature, improved electrocatalytic activity and rapid electron transfer process and increased photo-induced charge separation efficiency, but also overcome the existing graphene limitation and magnetite itself. The introduction of magneto-optical properties into graphene sheets create a new class of graphene-based materials that combine the high adsorption of graphene and the separation convenience rises from magnetic response demonstrated their potential in applications such as biosensing (Teymourian et al., 2013) and environmental remediation (Farghali et al., 2015).

In this work, $\text{Fe}_3\text{O}_4/\text{rGO}$ nanocomposite is accomplished *via* a simple, eco-friendly and efficient approach by in-situ deposition of Fe_3O_4 nanoparticles on reduced graphene

oxide (rGO) sheets at room temperature. Since the synthesis is a one-step approach, the problem in the aggregation of the reduced graphene oxide (rGO) sheets and magnetite particles are prevented. During the fabrication process, reduction of GO into rGO and chemically deposition of Fe_3O_4 nanoparticles on rGO sheets were occurred simultaneously. Thus, the loading of magnetic nanocrystals prevent the single layer graphene sheets from restacking once the reaction process was completed. Moreover, the possibility of contamination in the nanocomposite fabricated is reduced through this facile one-pot reaction. The Fe_3O_4 nanoparticles act as an effective stabilizer preventing agglomeration of GO sheets after reduction in solution through hydrophobic interaction (Sasha Stankovich et al., 2006). From the XRD spectra of $\text{Fe}_3\text{O}_4/\text{rGO}$ nanocomposites with no other characteristic peaks for impurities provide the information that the Fe_3O_4 nanoparticles anchored onto the surfaces of rGO sheets effectively prevent the exfoliated rGO from direct restacked after the reduction of GO due to the absence of diffraction peak of rGO in the XRD spectrum of $\text{Fe}_3\text{O}_4/\text{rGO}$ nanocomposites. (Y. Zhang et al., 2012) The synthetic method is green and eco-friendly as it requires non-toxic solvents such as ferrous sulphate (FeSO_4) and sodium hydroxide (NaOH). Unlike other reported method required high temperature, such as hydrothermal method by Zhang et al. (X. Zhang et al., 2014), solvothermal method by Wu et al. (Q. H. Wu et al., 2013), and microwave irradiation method by Zhang et al. (M. Zhang et al., 2010), the formation of $\text{Fe}_3\text{O}_4/\text{rGO}$ nanocomposite reported was occurred at room temperature. Therefore, the energy consumption is reduced, making the reported method efficient, cost-effective and easily controlled by varying the process parameters such as pH range in aqueous solution, temperature and concentration of ferrous ion (Fe^{2+}). By varying the weight ratio of graphene oxide (GO) and FeSO_4 in the starting materials, allowing the modification for the properties of fabricated nanocomposite, such as particle size

distribution, surface morphology, optical, electronic and magnetic property to be optimized for various applications.

2.5 Fe₃O₄/rGO nanocomposites Photocatalysts

The widespread of organic dyes due to the rapid growth of textile and dye industry has caused critical environmental issues. The discharge of organic pollutants such as dye effluents, agricultural waste and chemical spills into the ecological system can pollute the ground water resources, and contain toxic, non-biodegradable components that are harmful effects to ecosystem as well as on human beings. Particularly, the releases of synthetic dye effluents are that contained azo-dyes, anesthetic pollutants and intermediate products as the degradation products such as aromatic amines from azo-dyes are highly carcinogenic.

Besides, the effluents such as methylene blue (MB) (**Figure 2.5**) and neutral red (NR), the common cationic dyes that used extensively in the industries can reduce the light penetration and consequently affect the photosynthesis process and eventually exhibits toxic effects towards the microbial populations (Gong et al., 2005). Owing to their enough stability to natural decomposition and persistence in the environment, the traditional wastewater treatment including conventional physiochemical and biological treatments are ineffective and environmentally compatible for the dyes removal. In this respects, the photoinduced redox chemical reaction, also known as photocatalytic oxidation occurred on the irradiated material surface emerged as new and promising technologies have become the focus that stimulate intensive efforts for purifying water-borne pollutants.

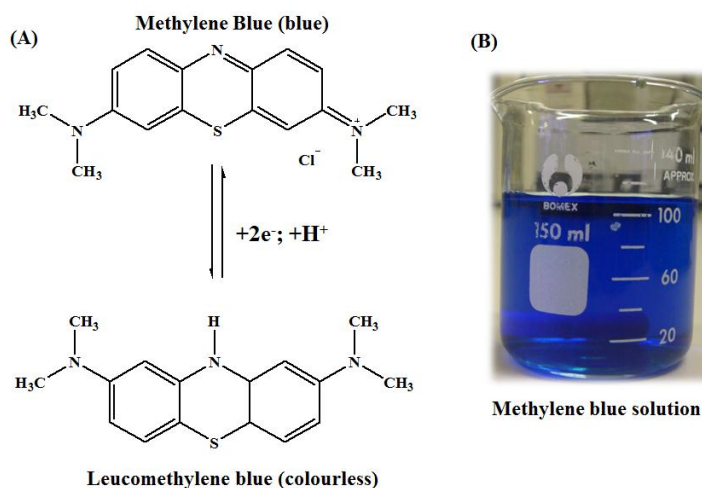


Figure 2.5: (A) Structure of methylene blue and its reduced form (leucomethylene blue). (B) Picture of methylene blue solution.

However, photoreaction does not occur by solely illumination of light in the absence of any catalyst, which refers to the photon-assisted generation of catalytically active species. Photocatalysis is an alternative green technology to clean the hazardous organic pollutants or degraded to harmless innocuous substances. Solar energy is renewable source energy with 45% of visible region, while only 4% belongs to UV region in the solar spectrum. Thus, photodegradation under visible light irradiation would be mainly employed to activate the photodegradation process.

Due to the excellent properties including large surface area, high electrical conductivity, chemical stability and sp^2 basal plane structure of 2D graphene, it has been tremendous attraction for constructing functionalized graphene-based visible-light-driven-photocatalysts. The incorporation of graphene support with semiconductor photocatalysts (e.g. rGO-TiO₂, rGO-ZnO, etc.) significantly show large specific surface, high adsorption, good visible-response, faster electron transfer rate, which consequently results in the efficiency of photoinduced charge separation and enhanced photocatalytic performance. However, the problems associated with recovery, reuse and separation of catalyst from the reaction system still exist after the photocatalytic reaction and become

a bottleneck for their environmental applications, due to the good dispersive property of these materials may cause the loss of catalysts and inconvenient to recycle as well as the secondary environmental problems. Here, the biocompatibility, eco-friendly and strong superparamagnetic nature of magnetite (Fe_3O_4) nanophotocatalyst materials are introduced into 2D graphene sheets provide a convenient magnetic separation to remove and recycle the catalysts under an external magnetic field (Lin et al., 2012). The combination of Fe_3O_4 nanoparticles and rGO sheets has successfully overcome this limitation of recovery, exhibit ferrimagnetic behaviour, strong adsorption ability and leads to excellent photocatalytic performance by the increased charge separation efficiency in Fe_3O_4 nanoparticles (J. Wang et al., 2012; Wei Wu et al., 2015; C. Zhou et al., 2014).

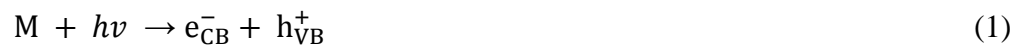
2.5.1 Basic Mechanism for the Photocatalytic Degradation of Organic Pollutants

The photogenerated holes (h^+) and electrons (e^-) in the photodegradation process are plays an important key role in pollutant degradation. These photogenerated electrons and holes are unstable and it can easily recombine together and renders low photocatalytic efficiency. Thus, the generation of highly reactive and powerful oxidizing species such as hydroxyl radicals ($\bullet\text{OH}$) and superoxide radical anions ($\text{O}_2^{\bullet-}$) to oxidize the organic contaminants.

Under light irradiation, photocatalysts absorbs sufficient photon energy undergoes photo-excitation to form electron-hole pair (**Figure 2.6**). The photoinduced electrons (e^-) are promoted to the conduction band (CB) and leaving behind positive holes (h^+) in the valence band (VB) (Eqn. (1)). At the same time, the organic contaminants also undergo photo-excitation to cationic radicals. There photoinduced electrons and holes will participate in some chemical reactions with adsorbed species to generate the reactive oxidation agents. For instance, the photogenerated electrons react

with oxygen (O_2) to generate the superoxide anions ($O_2^{\bullet-}$), as called electron scavengers to extend the duration of charge recombination (Eqn. (2)). On the other hand, the holes may react with surface-bound H_2O or OH^- groups to produce hydroxyl radicals (OH^\bullet) (Eqn. (3)). The oxidation reaction by these powerful oxidizing species would efficiently degrade the dye pollutants into non-toxic products (Eqn. (4)-(5)). The proposed mechanism is summarized in the equations below (Chen et al., 2010; Kuo et al., 2001):

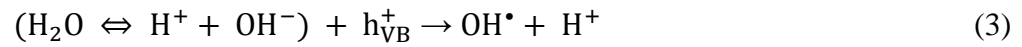
1. Absorption of sufficient photon by photocatalyst, M ($E_{hv} \geq E_{bg}$)



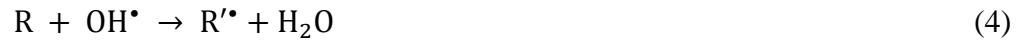
2. Formation of superoxide radical anion



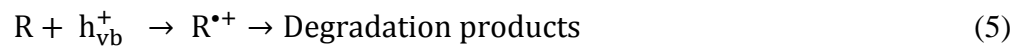
3. Formation of hydroxyl radical by holes



4. Oxidation reaction of dye pollutants (R) by hydroxyl radical (OH^\bullet)



5. Direct oxidation with holes



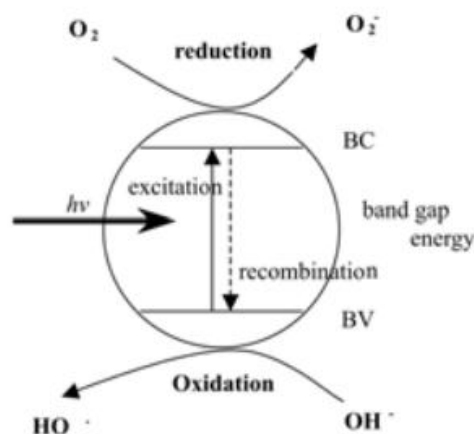


Figure 2.6: Schematic representation for the photodegradation process in the presence of photocatalysts under visible light irradiation (Silva et al., 2002).

2.6 Electrochemical Sensor Based on Fe₃O₄/rGO Modified Electrodes

2.6.1 Dopamine (DA)

Neurotransmitters are the endogenous chemicals that allow transmission of nerve impulses from one neuron (brain cell) to another across synapses. Sometimes, they can be classified as excitatory and inhibitory depending on their actions on the neurons. Inhibitory neurotransmitters are those that calm the brain and help in creating balancing, whereas, excitatory neurotransmitters have function in exciting the neurons and stimulating the brain.

Here, our main focus is dopamine (DA) (**Figure 2.7**) is a special neurotransmitter as it is considered to be both excitatory and inhibitory. DA is a hormone and one of the most important catecholamine neurotransmitters that are produced in the adrenal glands and several areas in the brain. Furthermore, DA is the most abundant catecholamine that belongs to the family of inhibitory neurotransmitter, which is widely distributed in the central nervous, renal, hormonal and cardiovascular systems.

Dopamine is strongly associated with reward mechanism in the brain. In the brain, DA may function as a neurotransmitter for message transfer in brain-body integration. Drugs like cocaine, heroin, nicotine and alcohol are DA transporter blocker that competitively inhibits the re-uptake of DA and eventually increase the DA level and stimuli the pleasurable emotions of feeling satisfied, happiness and also raise the risk of depression. However, a deficiency or abnormalities in the DA concentration may lead to several neurological diseases, such as schizophrenia, Parkinson's disease (Obata, 2002), attention deficit hyperactivity disorder (ADHD) (Mohammadi et al., 2011), restless legs syndrome (RLS) (Aurora et al., 2012) and drug addiction. However, the voltammetric determination of DA remains a challenge in the presence of large excess of ascorbic acid (AA). Often, AA is similarly present along with some neurotransmitter including DA in the mammalian nerve and brain, with a concentration of 100-1000 times higher than that of DA. Furthermore, DA and AA exhibit very similar oxidation peak potentials, and therefore the coexistence of AA results the poor selectivity and reproducibility of electrochemically detection DA, due to the fouling effect from the product of AA oxidation on the electrode surface.

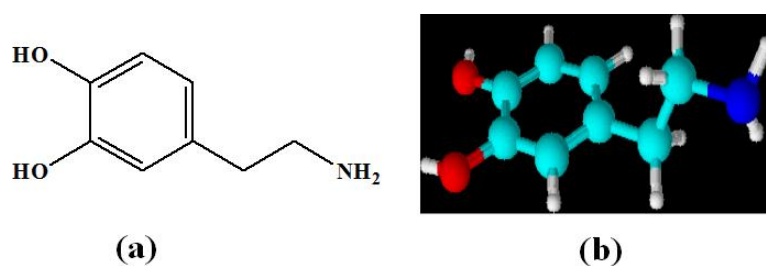


Figure 2.7: Molecular structure of dopamine (DA).

Ascorbic acid (AA), so called vitamin C is a water soluble vitamin that naturally occurring in the form of sugar acid with peculiar antioxidant properties. It appears as a yellowish or white crystal with slightly acidic taste. It is an essential nutrient and crucial

in many biological and physiological metabolisms. Ascorbic acid is a strong reducing agent and readily to oxidize to form dehydroascorbic acid and involves its electron transport reactions has been subjected to numerous biomedical studies. Moreover, it is a powerful antioxidant and can act as a scavenger to oxidize the free radicals and oxygen-derived species to prevent the oxidative damage in cellular components. Besides facilitates the absorption of iron, it also plays a key role in the cell development, healing if injuries and the synthesis of collagen because the lack of vitamin C may results the formation of impaired collagen and scurvy. Furthermore, it also helps to maintain the health of skin, cartilage, teeth, bone and blood vessels (Davey et al., 2000; Iqbal et al., 2004).

The symptoms for a low level of vitamin C appear when the serum level of the body falls below 0.2 mg/dl. The chronic deficiency of this vitamin may cause number of disorders including scurvy, anemia, neurotic disturbance, bleeding gums and poor wound healing, diabetes, and cardiovascular disease. Hence, an uptake of at least 10 mg ascorbic acid per day through the consumption of fresh fruit and vegetables can potentially avoid the severe diseases (Hacisevki, 2009; Schleicher et al., 2009).

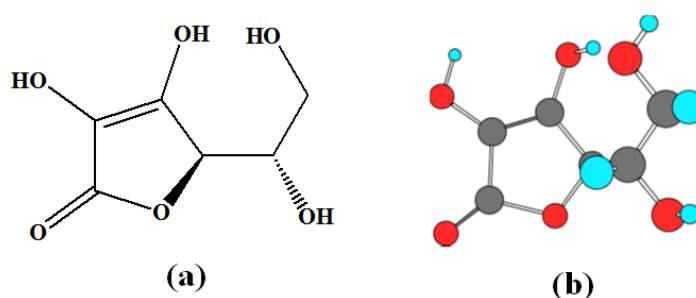


Figure 2.8: Molecular structure of ascorbic acid (AA).

2.6.2 Electrochemical Sensor

For a decade, the importance functions of DA in the mammalian central nervous system and its electroactive nature has been motivated and stimulated the development

of a sensor for a precise and selective detection of DA at a relatively low concentration (26-40 nM and below) in a variety of studies related to biological and biomedical applications.

Up to date, several analytical methods have been established and developed to the detection of dopamine at sub-micro concentration level, including high performance liquid chromatography (HPLC) (Carrera et al., 2007), chemiluminescence (Xu et al., 2012) and gas chromatography-mass spectrometry (GC-MS) (Naccarato et al., 2014). Although these analytical techniques have high sensitivity, selectivity and low detection limits towards DA from $\mu\text{g/L}$ to ng/L levels in the different environmental samples, however, they are still having some limitations, such as time-consuming multi-step processes that involving liquid-liquid extraction (LLE) and solid-phase extraction (SPE) for the pre-treatment procedures and require expensive and complicated equipment, which prior for the chromatographic analysis of estrogenic compounds in environmental samples. In this regard, electrochemical sensor is a preferred alternative method in monitoring the lower concentration of DA under physiological conditions with the advantages of its simple operation, most straightforward, low-cost, fast response, time saving, high sensitivity, excellent selectivity and real-time detection. Various voltammetric techniques (i.e. cyclic voltammetry (CV), differential pulse voltammetry (DPV), square wave voltammetry, and chronoamperometry (CA)) have been devoted and proven to have relatively low detection limit for tracing DA analysis (U. Chandra et al., 2011; Maina et al., 2010; Njagi et al., 2010).

Previously, direct determination of DA is widely used in the traditional electrochemical sensor method. However, this direct determination of DA causes the poor response and selectivity towards DA, which may attribute to the relatively large overpotential of direct oxidative detection at electrode surface and formation of

phenolic hydroxyl radicals on the electrode together with poor reproducibility. Moreover, the fouling effect often occurred at a bare electrode that eventually results the rather low sensitivity and selectivity towards DA (Hubbard et al., 1984). In addition, co-existence of several interfering species such as ascorbic acid (AA) and uric acid (UA) are sharing nearly same oxidation potentials on the bare electrode, which resulting in overlapping of voltammetric responses and poor selectivity and sensitivity in DA measurement (Kamyabi et al., 2012). Therefore, surface modification of working electrode emerged as an effective way to circumvent the overvoltage and slow kinetics of electrode processes in the simultaneous determination of DA and AA (Ensafi et al., 2009). The improved sensitivity and selectivity of modified electrodes in analytes detection are highly depending on their excellent electrical conductivity and electrocatalytic properties.

Magnetic nanoparticles consists of Fe^{2+} and Fe^{3+} valence metals have attracted increasing attention in biosensor applications, because of their interesting properties such as magnetic properties and easy redox reaction rises from transfer between Fe^{2+} and Fe^{3+} , environmentally friendly, low cost, biocompatibility, excellent water solubility, and narrow size distribution and structural manipulation. Electrode modification by incorporation of biocompatibility and superparamagnetic behaviour of magnetite (Fe_3O_4) nanoparticles onto the graphene sheets ($\text{Fe}_3\text{O}_4/\text{rGO}$) acquires novel properties such as unusual electronic and robust transport properties and high electrical conductivity. The $\text{Fe}_3\text{O}_4/\text{rGO}$ nanocomposite significantly enhance the electrocatalytic activities, increase the sensing surface and facilities the rate of electron transfer on the electrode surface. Subsequently, this will resolve the overlapping of anodic peaks of DA and AA during the electrocatalytic process (Pruneanu et al., 2015; W. Zhang et al., 2015).

CHAPTER 3 : EXPERIMENTAL METHODS

3.1 Introduction

In this chapter, the experimental details for this study is presented, including the chemicals and materials used, preparation method for Fe₃O₄/rGO nanocomposites, application studies in photocatalysis and electrochemical biosensors, along with the characterization techniques. This chapter consists of three sections, with the first section covers for the synthesis of Fe₃O₄/rGO nanocomposites; the second section covers the experimental details for the photocatalytic wastewater treatment and electrochemical biosensors with the Fe₃O₄/rGO nanocomposites. At the end, the characterization techniques have been used for sample analysis, photocatalytic activity measurements and electrochemical detection.

3.2 Section I

3.2.1 Chemicals and Materials

Graphite flakes were purchased from Ashbury Graphite Mills Inc. (Asbury, NJ), Sulfuric acid (H₂SO₄, 98 %), hydrogen peroxide (H₂O₂, 30 %), 3-hydroxytyraminium chloride (Dopamine, DA), L(+)-ascorbic acid (AA) and ammonium hydroxide (NH₄OH), 25 %), were purchased from Merck (Darmstadt, Germany). Iron (II) sulphate (FeSO₄.7H₂O, 99.5 %), methylene blue and potassium permanganate (KMnO₄, 99.9%) were obtained from System. Potassium hexacyanoferrate (III) (K₃[Fe(CN)₆]) was purchased from Sigma Aldrich. All other chemicals were of analytical grade and used without further purification. All solutions were prepared by deionized water (resistivity ≥ 18 M Ω) throughout the experimental process.

3.2.1.1 Synthesis of Graphene Oxide (GO)

GO was synthesized from graphite through the simplified Hummer's method (**Figure 3.1**) (Lim et al., 2011). Initially, 3 g of graphite flakes were treated with the mixture $\text{H}_2\text{SO}_4:\text{H}_3\text{PO}_4$ (360: 40 mL) solution in a ratio of 9: 1 and followed by gradually adding of strong oxidizing agent, KMnO_4 under magnetic stirring for the development of graphene oxide. The mixture was then left to continuously stir for 3 days to ensure the complete oxidation of graphite. After 3 days, the colour of mixture changed from dark purplish-green to dark brown. Then, oxidation process was stopped by adding 400 mL ice together with 27 mL of 30 % H_2O_2 into the solution to prevent the temperature of the suspension from exceeding 20 °. The treatment with the H_2O_2 efficiently reduced the residual of permanganate and manganese dioxide to the colourless soluble manganese sulphate. The changes colour of solution from dark brown to bright yellow indicated the highly oxidized level of graphite. The graphene oxide obtained was centrifuged and washed 3 times with 1 M HCl) and 6 times repeatedly with deionized (DI) water until the solution pH became 4 to 5. At the final washing process with DI water, the exfoliation of graphene oxide resulting in thickening of GO solution with a diminishing in effervescence, and eventually formation of light brown GO gel (Hummers Jr et al., 1958).

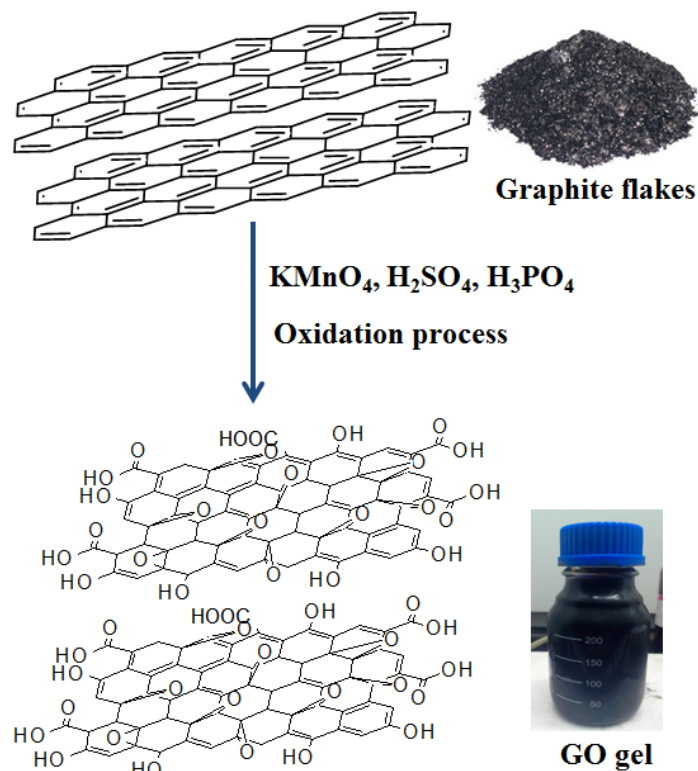


Figure 3.1: Schematic route for synthesis of graphene oxide (GO).

3.2.2 Synthesis of $\text{Fe}_3\text{O}_4/\text{rGO}$

The $\text{Fe}_3\text{O}_4/\text{rGO}$ nanocomposites were prepared by a facile in-situ chemical synthetic approach at room temperature. Initially, A 25 mg of GO gel was dispersed in deionized water (DI) under magnetic stirring and followed by sonication for 20 min. Then, 25 % of NH_4OH solution was added drop-wise into the GO solution until pH reached 11 or 12. Later, a desired quantity of FeSO_4 solution was added slowly to the GO solution under magnetic stirring and left overnight at room temperature. The next day, the obtained mixture of black precipitate ($\text{Fe}_3\text{O}_4/\text{rGO}$) was centrifuged and washed with DI water for 20 min at 6000 rpm. This step was repeated for 3 times to remove excess ammonium ions in the solution. At the end, the black precipitate was dried in oven at 60 °C. The Fe_3O_4 nanoparticles was obtained *via* the similar procedure in the absence of GO and labelled as F20. Similarly, rGO was synthesized by using the same

protocol without the adding the FeSO_4 and labelled as G1. The schematic synthetic pathway of $\text{Fe}_3\text{O}_4/\text{rGO}$ shows in the **Figure 3.2**. The $\text{Fe}_3\text{O}_4/\text{rGO}$ nanocomposites were prepared by varying the weight ratio between the GO and FeSO_4 and was denoted as G1FX, where X is the weight ratios between GO and FeSO_4 to GO. For the sake of convenience, four kinds of $\text{Fe}_3\text{O}_4/\text{rGO}$ was prepared by fixing GO as constant with varying FeSO_4 content ($m_{\text{GO}}: m_{\text{FeSO}_4} = 1: 2, 1: 5, 1: 10, 1: 20$) and labelled as G1F2, G1F5, G1F10 and G1F20, respectively (**Table 3.1**).

Table 3.1: Weight ratios between GO (gel) and FeSO_4 that being used for the preparation of $\text{rGO}/\text{Fe}_3\text{O}_4$ nanocomposites.

Sample	m_{GO} (mg)	m_{FeSO_4} (mg)	Weight ratio (GO: FeSO_4)
G1F2	25	50	1:2
G1F5	25	125	1:5
G1F10	25	250	1:10
G1F20	25	500	1:20
G1	25	-	-
F20	-	500	-

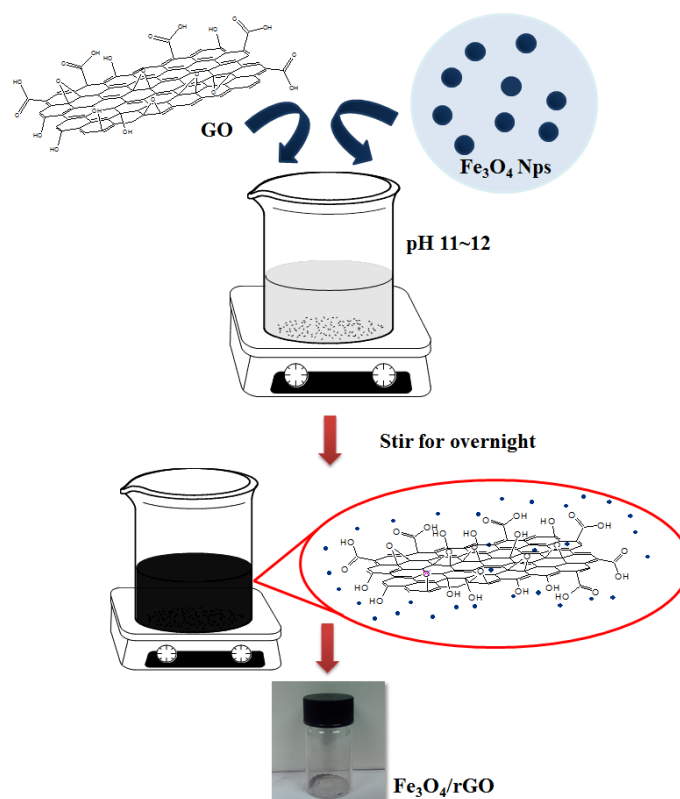


Figure 3.2: Schematic pathway for the synthesis of Fe₃O₄/rGO nanocomposite.

3.3 Section II

3.3.1 Photocatalytic Activity Measurements

The photocatalytic performance of Fe₃O₄/rGO nanocomposites was evaluated based on degradation of methylene blue (MB) under natural sunlight irradiation. The photocatalytic experiments were carried out on bright sunny days from 9 a.m. to 2 p.m. All the measured photocatalyst materials (2 mg Fe₃O₄/rGO) were separately dispersed in the 12 mL aqueous solution of the MB (10 mg/mL) under magnetic stirring and left overnight (12 h) at room temperature in order to study the adsorption behaviour. Prior to sunlight irradiation, the MB was kept in the dark under stirring for 1 h in order to allow the system to reach an adsorption-desorption equilibrium between the photocatalyst and MB molecules. At given time intervals, 2 mL of irradiated MB solution was withdrawn and the degradation rate was monitored and the catalyst in the solution was separated by

magnetic field, using a permanent magnet. The equilibrium concentration of MB dye in the photo-reacted solution for each sample was analyzed by a UV-visible absorption spectrophotometer (Thermo Scientific Evolution 300) by measuring the absorbance band maximum at the wavelength of 662 nm.

3.3.1.1 Durability Test

Recyclability test of a catalyst is a valuable key feature to verify the stability and sustainability of sample without any mechanical failure and chemical stability. In order to study the sustainability of magnetic separable Fe₃O₄/rGO photocatalyst in the photodegradation of MB under natural solar light, eight consecutive cycles were evaluated. The used photocatalyst was recovered by applying a magnetic field and washed with DI water before re-dispersed into the fresh MB solution (10 mg/mL) for the next consecutive cycle. The photodegradation rate (change of MB concentration in solution) and MB removal efficiency during the degradation process with the different photocatalysts were recorded and calculated using the following equations.

$$\text{Photodegradation rate} = \frac{C_t}{C_0} \quad \text{----- (Eqn. 1)}$$

$$\text{Dye removal efficiency} = \left(1 - \frac{C_t}{C_0}\right) \times 100 \% \quad \text{----- (Eqn. 2)}$$

where, C₀ represents the initial concentration of MB and C_t is the concentration of MB at a reaction time 't'.

3.3.2 Electrochemical Studies

3.3.2.1 Fabrication of Sensor Electrodes

Prior to the modification, the surface of glassy carbon electrode (GCE) was polished carefully by alumina suspension (0.05 μm) on a microcloth polishing pad, followed by thoroughly rinsed and ultrasonically cleaned using DI water to produce a

mirror-like surface. Subsequently, the GCE was dried at the room temperature. For the preparation of modified electrode, a 1.5 mg/mL suspension of Fe₃O₄/rGO in DI water was sonicated for 1h and then, a 5 μL of the suspension was coated on the freshly treated GCE surface. The modified GCE electrode was then dried in the oven at 60 °C. A similar drop casting procedure was repeated used to fabricate other modified GCE electrodes.

3.3.2.2 Electrochemical Studies of Modified Electrodes

In the present study, all the electrochemical measurements such as cyclic voltammetry (CV), electrochemical impedance spectroscopy (EIS), and differential pulse voltammetry (DPV) were carried out using a VersaSTAT 3 electrochemical analyzer (Princeton Applied Research, USA) (**Figure 3.3**) with a conventional three-electrode cell system. A bare GCE (3 mm in diameter) or modified electrodes was used as working electrode, Ag/AgCl and Pt wire were used as reference and counter electrode, respectively. Phosphate buffer solution (0.1 M) was used as supporting electrolyte. The phosphate buffer solution (PBS) (0.1 M with pH 6.5) was prepared by mixing stock of solution 0.1 M Na₂HPO₄·2H₂O and 0.1 M NaH₂PO₄·H₂O. Stock solutions of DA and AA were freshly prepared by using doubly-distilled (DI) water and used for electrochemical studies. All the electrochemical experiments were performed at room temperature. Before each measurement, all solutions was deoxygenated under nitrogen atmosphere for 10 min and treated with 5 successive cycles of cyclic voltammetric sweeps until a steady CVs curve achieved.



Figure 3.3: Photographic image of VersaSTAT 3 electrochemical analyzer (Princeton Applied Research, USA).

The electrochemical behaviour of the different modified electrodes were evaluated using CV technique in the aqueous solution of $K_3[Fe(CN)_6]$ containing 0.1 M KCl, at a scan rates of 100 mV/s between -0.2 V and +0.6 V. To investigate the interface properties of modified electrode surface, EIS was performed in the frequency range from 10^{-1} to 10^4 Hz in 5 mM $[Fe(CN)_6]^{3-/4-}$ solution containing 0.1 M KCl.

3.3.2.3 Electrochemical Detection of Dopamine (DA) and Ascorbic Acid (AA)

The bare GCE and modified electrodes were immersed in PBS solution (0.1 M, pH 6.5) containing AA and DA concentration in the range of 1-25 mM and 0.5-100 μ M, respectively to study the electrochemical response at a scan rate of 100 mV/s between -0.1 V to 0.6 V.

In the interference study for modified electrode, the simultaneous addition of possible interfering substance, such as 2 mM AA on the determination of DA into the pH 6.5 PBS was evaluated by DPV technique.

The reproducibility and stability of modified electrode plays a vital role to verify the long-term stability of a sensor. Thus, the reproducibility of modified electrode was

checked by recording the 10 successive CV data in 0.1 M PBS with pH 6.5 containing 0.1 M DA with same fabrication procedure. **Figure 3.4** shows the electrochemical detection of DA and AA in three-electrode cell system.

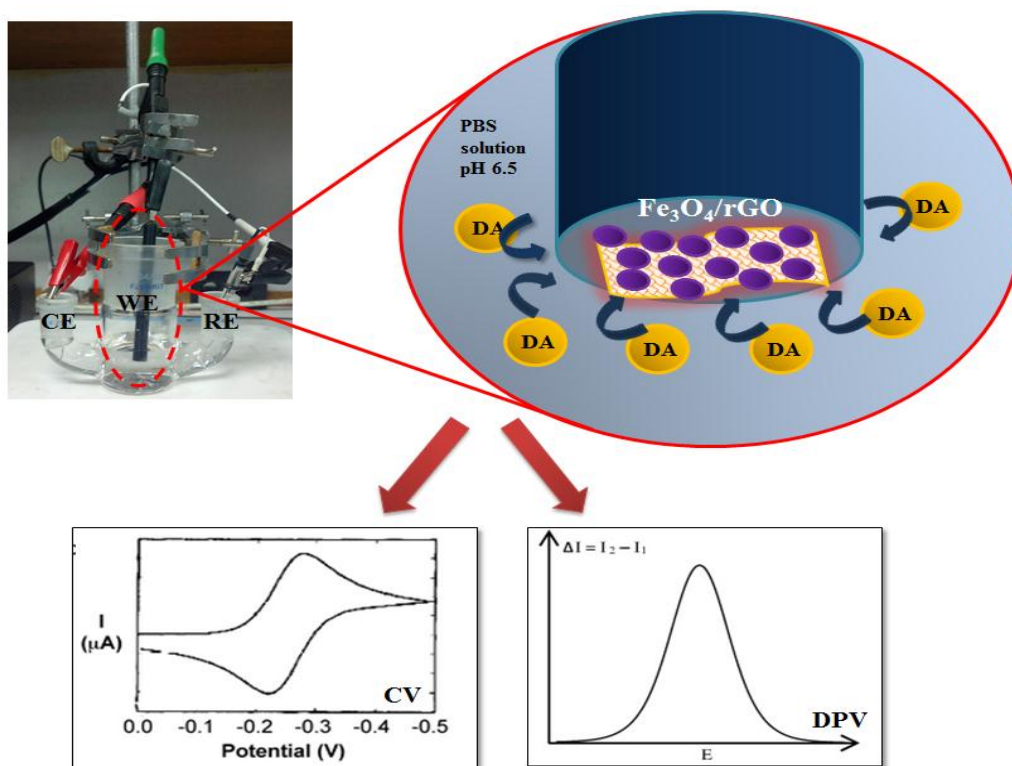


Figure 3.4: Electrochemical detection of dopamine and ascorbic acid in three-electrode cell system.

3.4 Section III

3.4.1 Characterization Techniques

Material characterization is an important analytic technique providing information of structure, morphology, mechanical, optical properties, magnetic properties by probe into the internal structure of materials. In the present investigation, the surface morphology of $\text{Fe}_3\text{O}_4/\text{rGO}$ nanocomposites was analyzed by FESEM, TEM and HRTEM. The crystalline structure and elemental composition of samples were confirmed by using XRD and micro-Raman spectroscopy whereas the VSM was used to

characterize the magnetic nature of samples. At last, UV-vis and PL were utilized to study the optical properties and electron-hole pair recombination of the nanocomposites. **Figure 3.5** showed the material characterization techniques utilized for Fe₃O₄/rGO nanocomposite.

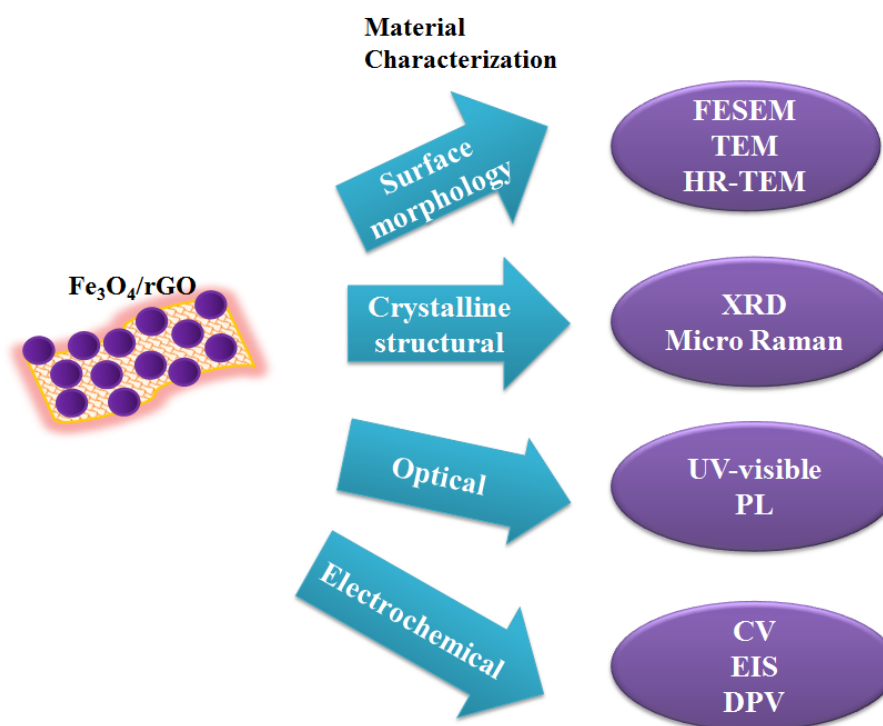


Figure 3.5: Characterization techniques involved for Fe₃O₄/rGO nanocomposite.

3.4.2 Field Emission Scanning Electron Microscopy (FESEM)

The field emission scanning electron microscopy (FESEM) is a versatile and non-destructive analysis technique that used to visualize and observe very small structure on the surface of fractioned or entire cells or materials. As compared with the conventional SEM, the FESEM can able to provide and reveal clear imaging small as 1 nanometer (nm) and detailed information about the morphology and composition of the materials. Besides, this characterization technique is preferred among the researchers as it offers high stability and is compatible with energy dispersive spectroscopy (EDS) at

the accelerating voltages to examine smaller spot areas. The FESEM works with the negatively charged electron that liberated by a field emission source in the electron gun of a scanning electron microscope, which later resulting improved spatial resolution and minimizes damage of the samples (Bogner et al., 2007). In the study, the surface morphology of the as-synthesized nanocomposites ($\text{Fe}_3\text{O}_4/\text{rGO}$) were observed using FEI Nova NanoSEM 400-FESEM with an acceleration voltage of 5 kV. Then, the ISolution Image Analysis software was used to measure the particle size of iron oxide nanoparticles deposited on the surface of rGO sheets.

All the specimens for FESEM imaging must be able to sustain in the high vacuum environment. The preparation specimen step for FESEM observation is important in order to visualize sharper and less distorted image of structure objects in the best resolution scale. For the material in solution form, the sample need to be drop-cast onto a silicon wafer and dried at room temperature before placing into the FESEM chamber. During the FESEM characterization, EDX was used to reveal the elemental analysis in nanocomposite composition. **Figure 3.6** shows the pictorial image of FEI Nova NanoSEM 400 FESEM.



Figure 3.6: Photographic image of FESEM, FEI Nova NanoSEM 400.

3.4.3 High Resolution Transmission Electron Microscope (HRTEM)

HRTEM is a powerful and high resolution technique for perfect imaging of nanomaterials in the atomic scale. Unlike SEM, the HRTEM works based on both scattered and transmitted beams to create an interference image, and therefore it can provide better structural information at better than 0.2 nm spatial resolution. The HRTEM can able to investigate the internal composition of a material, including morphology, crystallinity and magnetic domains, whereas the conventional TEM can provides information about the surface of sample and elemental composition (Jia et al., 2010).

Hence, JEM-2100F-HRTEM was used for analyzing the internal composition of $\text{Fe}_3\text{O}_4/\text{rGO}$ and study the morphology, compositional, crystal structure and lattice imperfections on an atomic resolution scale (Sharma et al., 2000).

Prior to HRTEM analysis, the prepared composite samples are homogeneously dispersed by sonication for 1 h, followed by drop-casting onto a holey copper grid and subsequently dried at room temperature. The specimens for the highest resolution must be extremely thin i.e. <10 nm thick and relatively beam insensitive. HRTEM characterization is done under vacuum environment system and the heating experiments are designed to reduce the contamination of microscope. **Figure 3.7** shows the pictorial image of JEM-2100F-HRTEM.



Figure 3.7: Photographic image of HRTEM, JEM-2100F.

3.4.4 X-Ray Diffraction (XRD)

XRD is a non-destructive analytical technique used to analyze the atomic and molecular structure of an unknown crystal by X-ray pattern produced. Regarding to the arrangement of atoms within the lattice, XRD analysis can provide information such as lattice parameters, orientation of a single crystal, degree of crystallinity as well as size and shape of crystallite. The raw data obtained from the XRD will later using the PANanalytical X'pert Highscore software to determine the atomic or molecular structure of specimen. Miller indices can be used to specify or represent the orientation of lattice planes of a crystal, which determined by 3 integers h, k, l and are written (hkl) (Morgan et al., 2003). Each crystalline solid has its unique characteristic X-ray pattern independently of others which may be used as a “fingerprint” for identification. The XRD diffraction pattern is correlated with the interatomic distance, diffraction angle and the arrangement of the atoms in the crystalline state, which can express in Bragg’s Law mathematically as following:

$$2d \cdot \sin \theta = n \cdot \lambda$$

During the XRD characterization, the as-prepared nanocomposite was placed in a holder, and then was illuminated with CuK α radiation ($\lambda=1.4506 \text{ \AA}$), by employing a scanning rate of 0.033°s^{-1} in 2θ range from 5° to 80° by using PANalytical Empyrean XRD for determination of crystalline phase.

3.4.5 Micro-Raman spectroscopy

Raman spectroscopy is a powerful, in-situ and completely non-destructive experimental instrumentation chosen to identify the molecules and their functional groups in the fabricated composite and provide information about the internal structural and electronic changes in nanocomposite during the chemical reaction. Furthermore, study the bonding nature of various carbon materials can be revealed by probing the types of vibration modes for different materials (Alim et al., 2005). The Raman effect is based on the changes in the molecular dipole-electric polarizability occurs when the frequency of the reemitted photons is shifted up or down in comparison with original monochromatic frequency which subsequently provides information on vibrational, rotational and other low frequency transitions for molecules in the phase of solid, liquid and gaseous. The Raman spectra is the measurement of the intensity of light scattering relative to its Stokes shifts represented in wavenumbers from the wavelength of the excitation source (exciting laser light). In the Raman system, the sample is illuminated with a beam of light in either ultraviolet (UV), visible (Vis) or near infrared (NIR) range. The scattered light is collected with a lens and finally a Raman spectrum is obtained with a charge-coupled device (CCD) array detector.

In the study, the prepared nanocomposites were characterized using Renishaw inVia Raman microscope system (**Figure 3.9**) excited with 514 nm (green laser). The

measurements were scanned from wavenumber 100 to 2000 cm^{-1} . It is important to noted that selection of a wrong laser power may cause the destruction of the sample.



Figure 3.8: Photographic image of Renishaw inVia Raman microscope system.

3.4.7 Ultraviolet-Visible (UV-Vis) Spectroscopy

UV-visible absorption spectrophotometer is widely used to explore the optical property, absorption behaviour and bond structure of nanosized materials. Different molecules consist of different absorption wavelength. Therefore, the number of absorption bands in absorption spectra are corresponding to the structural groups within the molecules (Anderson et al., 2007; Skoog et al., 1980). The as-prepared nanocomposites were analyzed on Thermoscientific Evolution 300 UV-vis absorption spectrophotometer (**Figure 3.10**). Moreover, this analytical technique was performed to determine the degradation rate of MB in the photocatalytic studies in the wavelength range of 200-800 nm.

Prior to the analysis on powder samples, the sample was sonicated for 30 min to produce a homogeneous dispersion. It is necessary to carry out a baseline measurement before measuring the new sample. Then, a quartz cuvette containing deionized water as

a reference and another quartz cuvette with sample solution were inserted into the quartz holder. During the measurement, the sample molecules undergo electronic transition under the excitation of the electromagnetic spectrum. Next, absorption spectrum was measured due to the transitions from the ground state to the excited state and eventually produces the absorbance spectrum *via* software.



Figure 3.9: Photographic image of computer controlled Thermoscientific Evolution 300 UV-vis absorption spectrophotometer machine.

3.4.8 Photoluminescence Spectroscopy

Photoluminescence (PL) is defined as the phenomenon when radiative emission from a matter after sufficient absorption of photons and eventually these electronic excitations falls in the shorter wavelength side (ultraviolet region) of the electromagnetic spectrum. PL spectroscopy is a standard, non-destructive and contactless characterization method of probing the electronic and optical properties of materials (Buyanova et al., 1999; Vanheusden et al., 1996). The PL curves of prepared sample were obtained using Renishaw inVia PL microscope excited at a wavelength 325 nm. From the PL emission spectral, the intensity and distribution of spectra provides the information about the types of transition energies of photoexcited material, which can be utilized to determine electronic band gap, impurity levels and defect detection and also can directly measure the relative amount of radiative and non-radiative recombination rate of a photoactive materials.

3.4.9 Vibrating Sample Magnetometer (VSM)

The vibrating sample magnetometer (VSM) is a fast and sensitive analytical technique pioneered by S. Foner in 1959 (Foner, 1959). It is used to characterize and measure the magnetic properties, including hysteresis, saturation magnetization (M_s), coercivity and anisotropy nature of various magnetic materials. Basically, the $\text{Fe}_3\text{O}_4/\text{rGO}$ sample was magnetized by placing it inside a uniform magnetic field and used by piezoelectric material to physically vibrating the sample sinusoidally. The induced voltage in the pickup coil is independent to the strength of the applied magnetic field but is proportional to the magnetic field of the sample. The magnetization (M) of $\text{Fe}_3\text{O}_4/\text{rGO}$ sample was measured by placing it in an external magnetic field in VSM, when converting the dipole field of magnetic sample into an AC electrical signal. Moreover, it is possible to obtain the magnetic hysteresis (H) curve of $\text{Fe}_3\text{O}_4/\text{rGO}$ sample with the measurement in the field of an external electromagnet.

CHAPTER 4: RESULTS AND DISCUSSION

4.1 Introduction

This chapter briefly discussed on the mechanism involved in the nanocomposite synthesis, characterization method utilized and results of photocatalysis and electrochemical sensor applications. This chapter is divided into three major parts. Part I begins with the synthesis pathway and formation mechanism of Fe₃O₄/rGO nanocomposite. Part II consists of the discussion and interpretation of the analytical characterization of synthesized nanocomposite, including surface morphology with an aid of FESEM and HRTEM, structural and crystallinity properties with XRD and micro-Raman, magnetic property by using VSM, optical and electronic properties by using UV-visible and PL and finally electrochemical properties by potentiostat. For the last section, part III the studies cover on photocatalytic degradation MB and simultaneous electrochemical detection of DA and AA by using synthesized Fe₃O₄/rGO nanocomposite. The magnetically separable of Fe₃O₄/rGO nanocomposite not only showed enhanced photocatalytic activity towards the degradation of organic dye but also demonstrated excellent sensitive and selectivity ability in the simultaneous electrochemical detection of DA and AA.

4.2 Part I

4.2.1 Formation mechanism of the Fe₃O₄/rGO nanocomposite

Graphene nanosheets, itself hardly dispersed in most of the polar solvents, such as water and ethanol due to the lack of oxidized surface functional moieties having planes mostly decorated with the hydroxyl, epoxy, carbonyl and carboxyl group located at the edges. In addition, due to the strong van der Waals interaction, rGO sheets tend to

generate irreversible aggregation which causes the further process difficult. Herein, this work proposed a suitable substituent material and an effective stabilizer to impede the agglomeration of graphene sheets. Graphene oxide (GO), consists of oxygenated surface functional groups is an interesting and promising candidate directly used as starting material in the preparation process. The presence of oxygen functionalities at the edge of GO sheets, results the high dispersion stability of GO that readily to be well-dispersed either in water or polar organic solvents to form homogeneous colloidal suspension and later lead to formation of water soluble multifunctional graphene-based composites. However, GO is electrically insulating by nature and thermally unstable (Stankovich et al., 2007; Tung et al., 2011), which may render its further processing in various applications. Hence, our strategy in the study involved the conversion of individual GO sheets to graphene-like sheets *via* in-situ reduction reaction, meanwhile loading the magnetite onto graphene sheets through one-pot reaction.

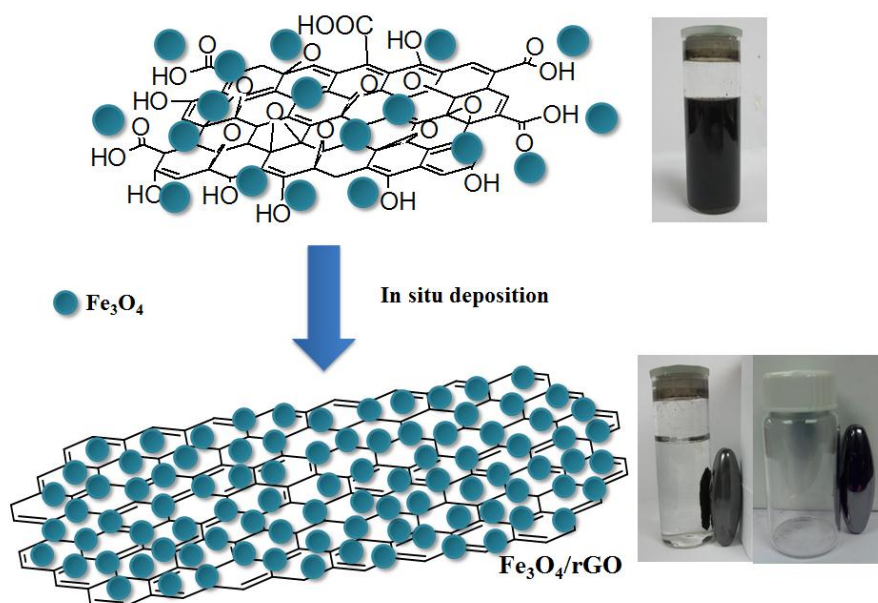


Figure 4.1: Schematic illustration for the formation $\text{Fe}_3\text{O}_4/\text{rGO}$ nanocomposite *via* a one-step in situ chemical deposition method.

The formation of Fe₃O₄/rGO nanocomposite involved redox reaction between the graphene oxide (GO) and FeSO₄ (Fe²⁺) at room temperature and is shown in **Figure 4.1**. During the synthetic process, the starting material, GO with its rich surface of oxygenated functional groups play an important role as oxidizing agent in the oxidation of Fe ions. The Fe²⁺ ions from FeSO₄ aqueous solution initially coordinated onto the surface of GO sheets. These Fe²⁺ ions are then captured by the carboxylate anions on the surface of GO sheets. As a strong oxidizing agent, GO effectively increase the oxidation state of Fe ions from Fe²⁺ to Fe³⁺ ((Eqn. (1)). In an alkaline condition, OH⁻ groups from ammonia act as a precipitating agent, together with the reaction of Fe³⁺ coordinated *in-situ* co-precipitated into Fe₃O₄ nanoparticles on the surface of rGO sheets covalently ((Eqn. (2)). Additionally, the OH⁻ groups attached on the GO surface can be used to produce Fe₃O₄ nanoparticles by transferring electron from Fe²⁺ to GO(8OH) species thereby forming a stable rGO sheets ((Eqn. (3)). During the redox reaction, GO sheets serve as the anchoring sites or as a “spacer” for the Fe₃O₄ nanoparticles consequently impedes the agglomeration of magnetic nanoparticles, meanwhile, these loading nanocrystals efficiently inhibit the single layer graphene from restacking.



4.3 Part II

4.3.1 Characterization of Fe₃O₄/rGO nanocomposites

4.3.1.1 Field Emission Scanning Electron Microscopic (FESEM) Studies

Figure 4.2 portrays the FESEM images of the G1, F20 and the Fe₃O₄/rGO nanocomposites. It was observed that G1 has a smooth surface with a paper-like

distinctive layered appearance (**Figure 4.2a**). F20, consisting only of Fe_3O_4 nanoparticles, are tend to agglomerate into a wide distribution of particle sizes (**Figure 4.2b**) (Su et al., 2011). Apart from that, it was clearly seen that Fe_3O_4 nanoparticles are uniformly embedded on the surface of rGO sheets with a narrow size distribution for all prepared nanocomposites. Deposition of Fe_3O_4 nanoparticles on the surface of rGO sheets has indicated a strong interaction between rGO sheets and nanoparticles (**Figure 4.2c-f**). Meanwhile, the unclear evidence for the formation of Fe_3O_4 nanoparticles in the FESEM image of G1F2 was further investigated by elemental mapping of C, O, and Fe using energy dispersive X-ray (EDX) analysis (**Figure 4.2h and g**). The area of bright contrast correlates with the Fe signal map. This result, later may couple with XRD result, provides the evidence for the presence of Fe_3O_4 nanoparticles on the surface of rGO sheets.

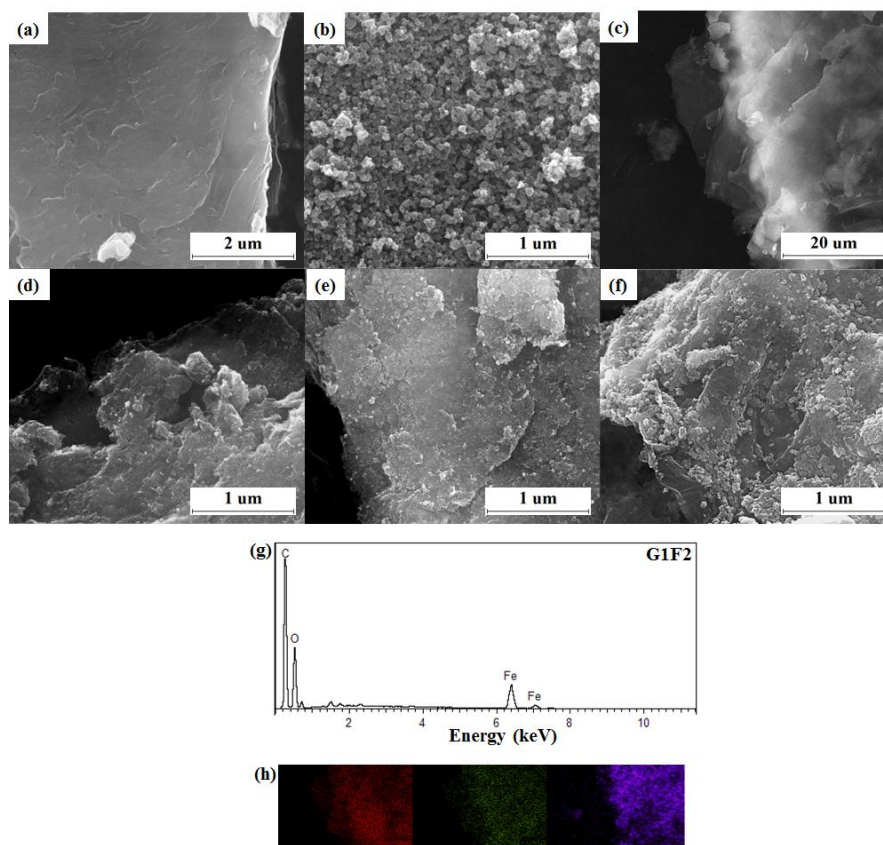


Figure 4.2: FESEM images of (a) G1, (b) F20, (c) G1F2, (d) G1F5, (e) G1F10 and (f) G1F20; (g) EDX spectrum of G1F2; and (h) elemental mapping of G1F2 based on image shown in (c).

4.3.1.2 High Resolution Transmission Electron Microscopic Studies

The morphology and structure of $\text{Fe}_3\text{O}_4/\text{rGO}$ nanocomposites was further observed by using recording the TEM. **Figure 4.3** presents the representative TEM images of synthesized G1, Fe_3O_4 and $\text{Fe}_3\text{O}_4/\text{rGO}$ nanocomposites and they clearly indicated that the uniform decoration of spherical Fe_3O_4 nanoparticles on the surface of rGO sheets. The rGO sheets remain flat and no curled or wrinkled layered appearance, despite of the distribution of Fe_3O_4 nanoparticles on the surface of rGO. This can be attributed to the distribution of the carboxylic acid groups on the graphene oxide sheets which is beneficial lead to the attainment of a higher surface area (Almeida et al., 2015). Thus, in-situ chemical synthesis of nanocomposites effectively impeded the aggregation of magnetic nanoparticles and restacking of rGO sheets. The lattice resolved HRTEM

image of $\text{Fe}_3\text{O}_4/\text{rGO}$ in **Figure 4.3d** clearly revealed the presence of atomic lattice-fringes of Fe_3O_4 nanoparticles on the surface of rGO sheets. The estimated lattice-fringe values of magnetic Fe_3O_4 nanoparticles are 2.533 Å and 1.643 Å, which can be respectively indexed to the (3 1 1) plane (2.530 Å) and (5 1 1) plane (1.614 Å), further confirming the crystalline nature of Fe_3O_4 .

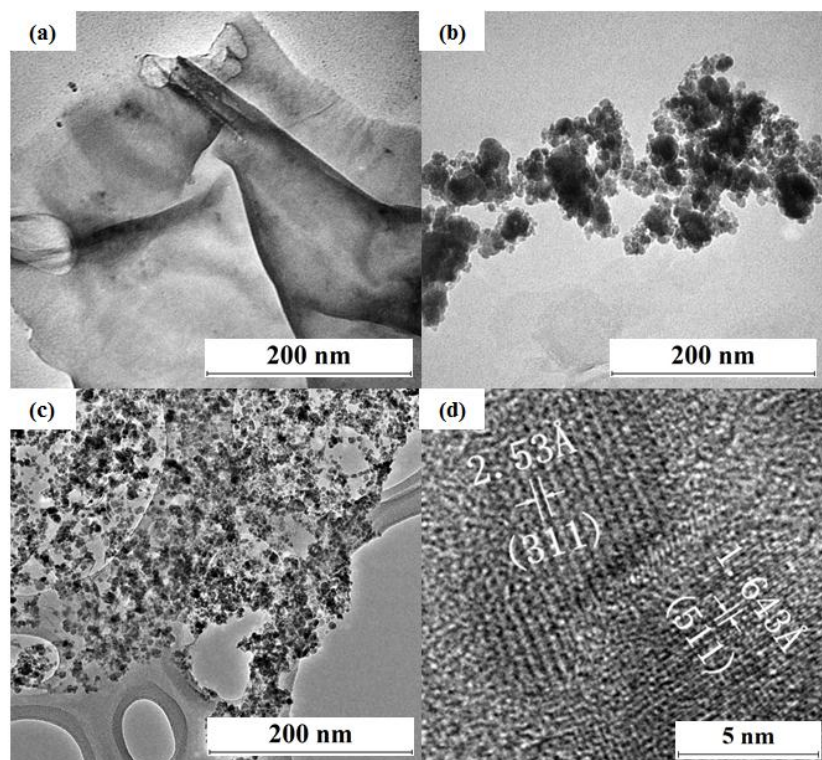


Figure 4.3: HR-TEM images of (a) G1, (b) F20, (c) $\text{Fe}_3\text{O}_4/\text{rGO}$, and (d) at a higher magnification.

Moreover, increase in the FeSO_4 concentration during the preparation of nanocomposite showed steadily increase the particle size and coverage density of Fe_3O_4 nanoparticles on the surface of rGO sheets in the order of G1F2 (3.8 nm) < G1F5 (7.9 nm) < G1F10 (10.5 nm) < G1F20 (12.1 nm) (**Figure 4.4a-d**), which disclose that the aggregation tendency of Fe_3O_4 nanoparticles in the $\text{Fe}_3\text{O}_4/\text{rGO}$ nanocomposite become increases with increasing the FeSO_4 precursor concentration. Among the different nanocomposite materials, the G1F20 showed the maximum aggregation of Fe_3O_4

nanoparticles (**Figure 4.4d**), while the G1F2 exhibited a good distribution of Fe_3O_4 nanoparticles on the surface of rGO sheets (**Figure 4.4a**). Generally, the nanoparticles tend aggregating to form clusters of colloids in the aqueous suspension, most probably attributed to the van der Waals interactions and weak magnetic attractions. The fast aggregation of nanoparticles in diluted aqueous solutions may diminish their remarkable material properties during the application. In this case, the easily agglomeration of Fe_3O_4 nanoparticles are mainly originates from the strong the magnetic dipole-dipole interactions among the particles, which will diminish their magnetic properties in the practical applications (Chicea, 2010).

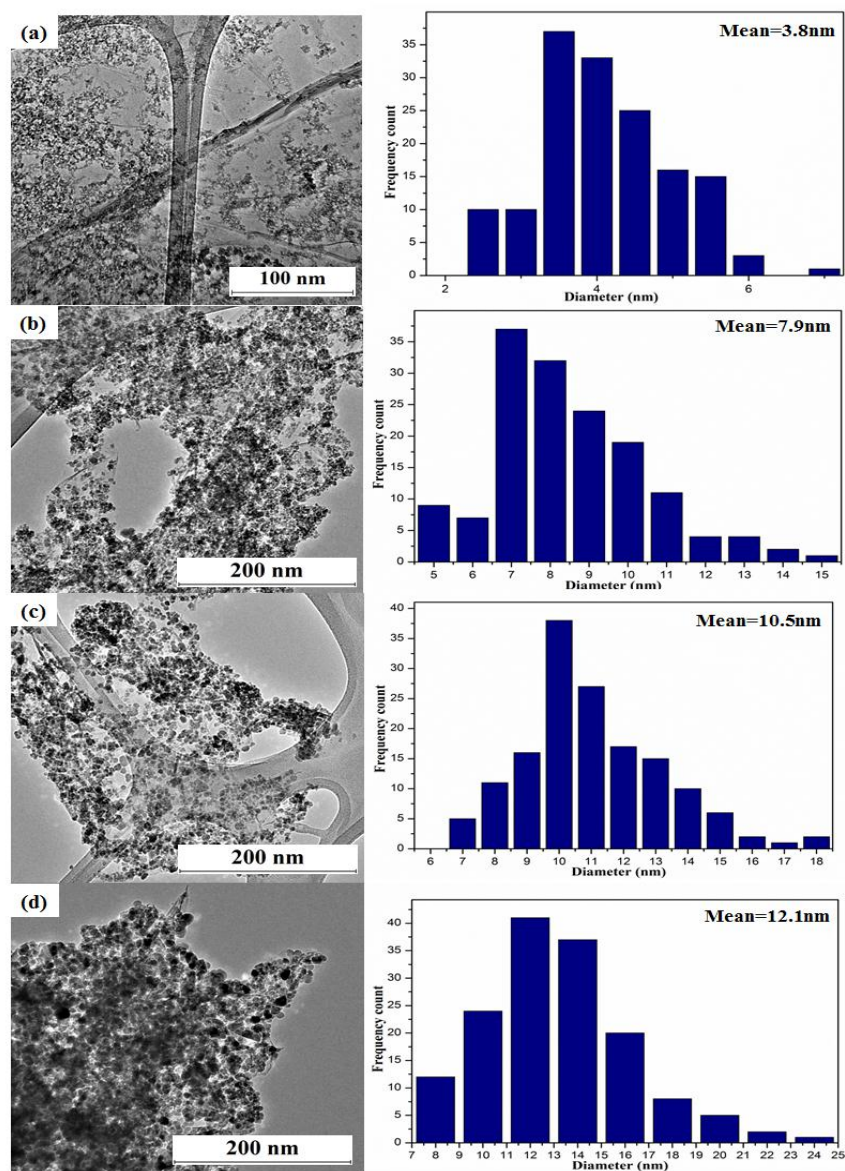


Figure 4.4: TEM images of (a) G1F2, (b) G1F5, (c) G1F10 and (d) G1F20. The average Fe₃O₄ nanoparticle diameter for each sample is (a) 3.8, (b) 7.9, (c) 10.5 and (d) 12.1 nm.

4.3.1.3 X-Ray Diffraction (XRD)

The structural information of G1, F20 and the nanocomposites were conducted by XRD, as shown in **Figure 4.5**. The sharp peak appear in G1 XRD spectrum at $2\theta = 10.8^\circ$ correspond to the (0 0 1) plane due to GO (**Figure 4.5a**), indicating that GO was not completely reduced to rGO during the preparation process and also implies that the GO in crystalline nature. Since the crystalline Interestingly, for the samples containing

Fe^{2+} ions, apart from G1F2, this peak was absent, suggesting that Fe^{2+} from FeSO_4 solution acts as a reducing agent for GO in the redox reaction of nanocomposites synthesis. On the other hand, the series of the diffraction peaks shown in **Figure 4.5b** at $2\theta = 30.2^\circ$, 35.6° , 43.3° , 53.7° , 57.3° and 62.8° were assigned to the (2 2 0), (3 1 1), (4 0 0), (4 2 2), (5 1 1) and (4 0 0) crystal planes of magnetite spinel structure of Fe_3O_4 (JCPDS No.: 19-0629). The pattern show the absence of impurity peaks, suggest that Fe_3O_4 nanoparticles are pure and exhibit good crystallinity. In **Figure 4.5c**, a sharp peak at $2\theta = 10.8^\circ$ in the XRD spectrum of G1F2 is corresponds to the (0 0 1) plane of the GO characteristics, while the diffraction peaks of Fe_3O_4 were not observed. The low content of reducing agent Fe^{2+} in the starting material resulted in the incomplete reduction of GO. However, the low diffraction peak located between 20° and 25° indicates that a small degree of restacking of graphitic sheets (Lim et al., 2012). In this case, the Fe_3O_4 formed on the surface of the partially reduced rGO sheets, which based on the dispersion ability of the nanocomposite to disperse homogeneously in an aqueous solution (**Figure 4.9**). In contrast to the rGO, Fe_3O_4 nanoparticles tends to aggregate in the most solvents, and the XRD pattern located at 35.6° , is assigned to reflection from the (3 1 1) planes of cubic Fe_3O_4 structure. When increasing the Fe^{2+} content, the five typical reflection peaks of Fe_3O_4 (30.2° , 35.6° , 43.3° , 53.7° , 57.3° and 62.8°) were observed for G1F5, G1F10 and G1F20 (**Figure 4.5d-f**).

In addition, there is an inverse correlation between the width of the diffraction peak and the concentration of Fe^{2+} , revealing that lower the Fe^{2+} concentration, smaller crystallite size of Fe_3O_4 formed in the nanocomposites. This result is proved with the observation from the FESEM and HRTEM (**Figure 4.2 and 4.4**). Surprisingly, the graphitic peak (0 0 1) for G1F5, G1F10 and G1F20 is missing due to the deposition of attached magnetite nanoparticles hinder the formation of van der Waals and π - π stacking interactions between the rGO sheets (X. W. Wang et al., 2012).

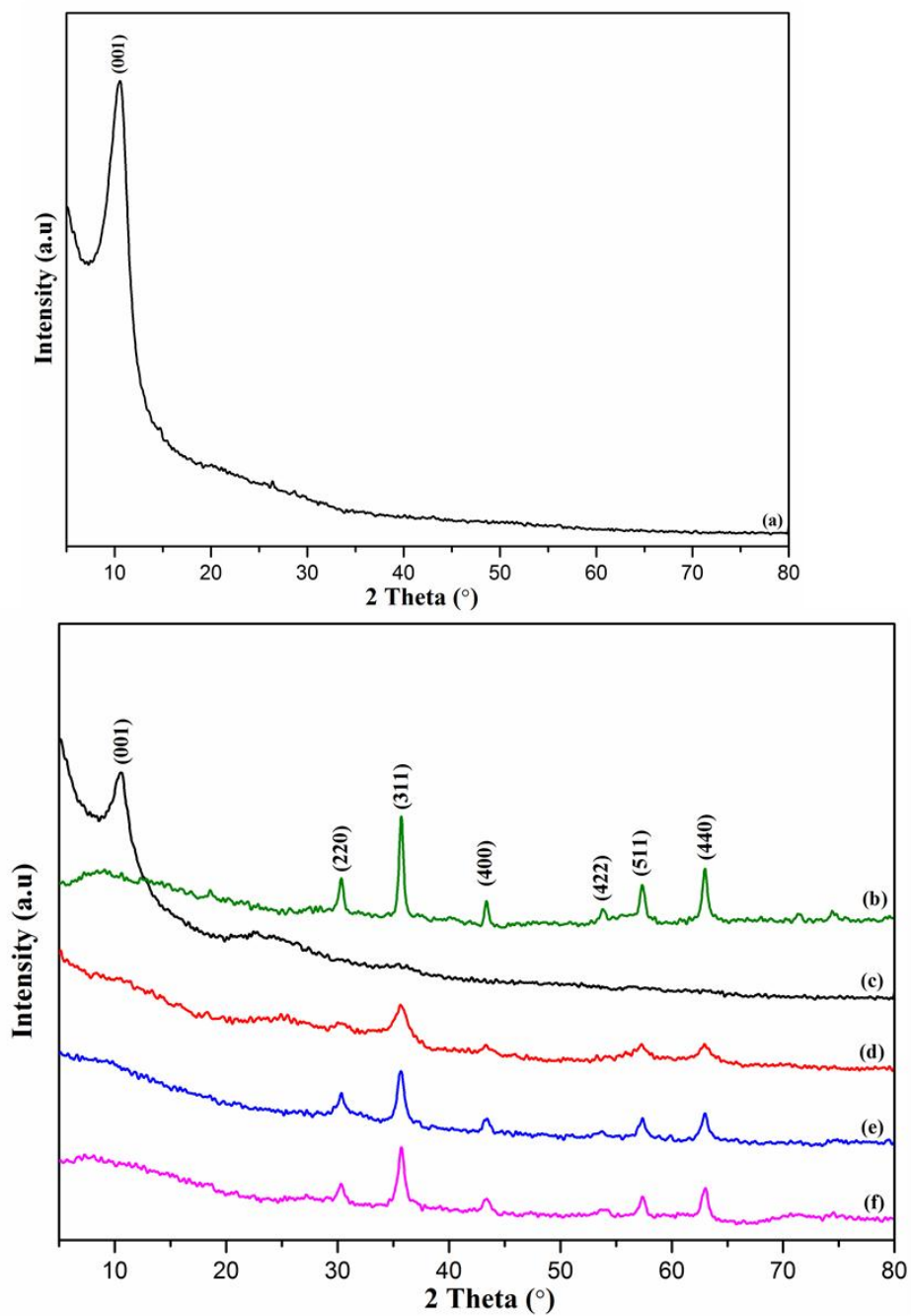


Figure 4.5: XRD patterns of (a) G1, (b) F20, (c) G1F2, (d) G1F5, (e) G1F10 and (f) G1F20.

4.3.1.4 Micro-Raman

The crystalline and electronic properties of GO, G1, F20 and Fe₃O₄/rGO nanocomposites were evaluated by using Raman spectroscopy with 514 nm laser. Raman spectroscopy is an efficient and powerful analytical tool to investigate the ordered and crystalline structure of carbonaceous materials, such as graphite, graphene oxide and reduced graphene oxide. **Figure 4.6** showed the Raman spectra of GO, G1 and Fe₃O₄/rGO nanomaterials. In the **Figure 4.6(Inset)**, the existence of two prominent peaks, D band around 1,350 cm⁻¹ which can assigned to the sp³ defects, which is the characteristic sign of the presence defective graphitic carbon while G band around 1,580 cm⁻¹ is ascribed to the in-plane vibration of sp² carbon atoms in a 2D hexagonal lattice of GO and rGO (L. Fu et al., 2015). The observed intensity ratio of D and G bands (I_D/I_G) is highly influence the structural transformation in the carbon nanomaterials. In **Figure 4.6c-f**, the I_D/I_G ratio of Fe₃O₄/rGO nanocomposite show significantly increases, which from 0.92 to 1.15 for nanocomposite G1F2 to G1F20 when compared to that of GO (0.91) due to the higher Fe₃O₄ content in the nanocomposite (Guo et al., 2012). Moreover, the high intensity of D band as compared to the G band of Fe₃O₄/rGO suggest the presence of localized sp³ defects within sp² clusters during the functionalization reaction of exfoliated GO (V. Chandra et al., 2010; Sathish et al., 2012). Meanwhile, a small characteristic Raman peak located around 670 cm⁻¹ indicates the presence of the magnetite (Fe₃O₄) (**Figure 4.6c-g**). Thus, the broad peak at 670 cm⁻¹ again further confirmed the successful synthesis and presence of magnetite nanoparticles in the Fe₃O₄/rGO nanocomposites (Ritter et al., 2002).

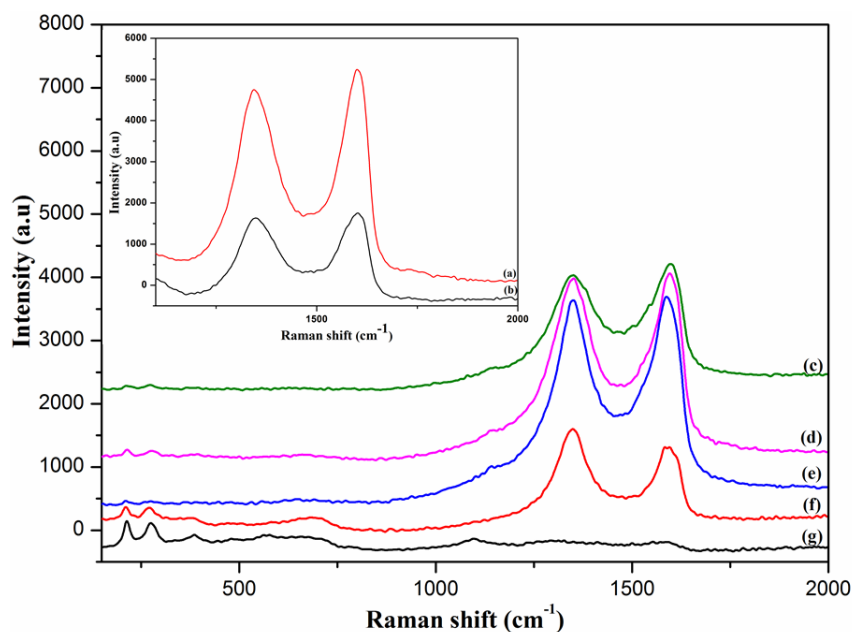


Figure 4.6: Raman spectra of (a) GO, (b) G1, (c) G1F2, (d) G1F5, (e) G1F10, (f) G1F20 and (g) F20.

4.3.1.5 UV-visible spectroscopy

UV-vis spectroscopy is an informative tool to investigate the optical properties of the photocatalysts. **Figure 4.7A** displays the UV-vis absorption spectra of graphene oxide (GO), Fe₃O₄ nanoparticles (F20) and Fe₃O₄/rGO nanocomposites. Graphene oxide exhibited an obvious characteristic absorption peak around 226 nm and a shoulder around 300 nm. The observed absorption peak at 226 nm is attributed to the $\pi \rightarrow \pi^*$ transition of aromatic C=C bonds whereas the shoulder peak at 300 nm is related to the $n \rightarrow \pi^*$ transition of the C=O bonds (**Figure 4.7A (a)**) (Paredes et al., 2008). However, this characteristic absorption peak of GO disappeared and slightly right-shifted to 255 nm for all Fe₃O₄/rGO nanocomposites (**Figure 4.7A (c-e)**), except for G1F2. This may be due to restoration of π conjugation within rGO sheets upon chemical reduction process (Y. K. Kim et al., 2012). However, this right-shifted peak barely noticed in G1F2 (**Figure 4.7A (b)**), because of the low content of reducing agent Fe²⁺ which resulting the incompletely or partially reduction of GO to rGO in G1F2 composite. Furthermore,

the redshift and enhanced absorption of the Fe₃O₄/rGO nanocomposites into the longer wavelength region (visible region) as compared to Fe₃O₄ nanoparticles (**Figure 4.7A (f)**), is ascribed to the formation of chemical linkage between Fe₃O₄ nanoparticles and rGO after incorporation of graphene into Fe₃O₄ nanoparticles (Y. S. Fu et al., 2012; Phan et al., 2011). Thus, the presence of rGO in Fe₃O₄/rGO nanocomposite is beneficial for the photocatalytic performance, especially in the formation of electron-hole pair during irradiation.

The band gap energy value (E_{bg}) of the as-prepared Fe₃O₄/rGO nanocomposites and Fe₃O₄ nanoparticles (F20) were calculated using the Tauc's plot method as following formula and their corresponding plots are shown in **Figure 4.7B (a-e)**

$$\alpha h\nu = A(h\nu - E_{bg})^{n/2}$$

where α is the absorbance, h is the Plank's constant, ν is frequency, and E_g is the band gap energy. The band gaps value of G1F2, G1F5, G1F10, G1F20 and F20 were estimated to be 3.25 eV, 3.10 eV, 2.90 eV, 2.75 eV and 2.55 eV, respectively. The observed E_g value of the Fe₃O₄/rGO nanocomposites is slightly higher and leads to a shift in the absorption edge with a decrease in particle size (**Figure 4.7B (f)**). This can be attributed to the quantum size effect (Singh et al., 2010; Yusoff et al., 2015). This result is in agreement with the FESEM and TEM results in **Figure 4.2** and **Figure 4.4**, respectively where the G1F20 in **Figure 4.4d** has the largest particles size among the nanocomposites and depicted the most agglomeration of Fe₃O₄ in nanocomposite, hence exhibited the narrowest band gap.

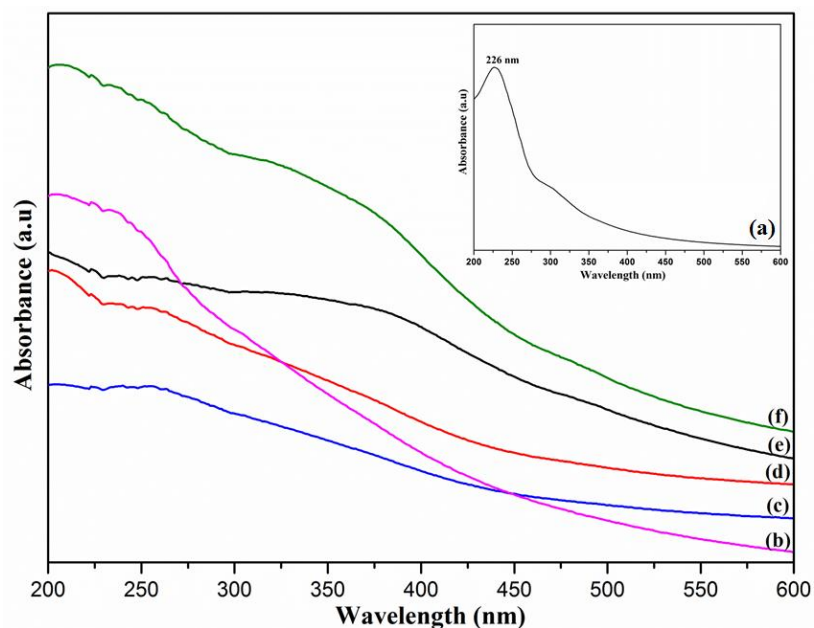


Figure 4.7 (A): UV-vis spectra of (a) GO, (b) G1F2, (c) G1F5, (d) G1F10, (e) G1F20 and (f) F20.

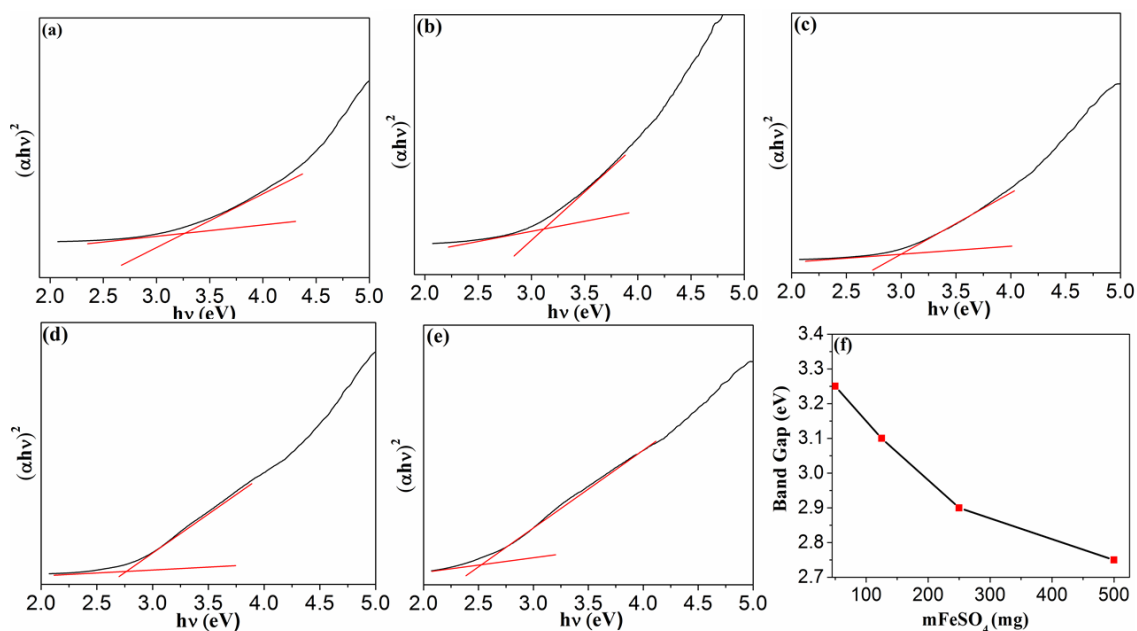


Figure 4.8 (B): Tauc's plot of (a) G1F2, (b) G1F5, (c) G1F10, (d) G1F20, (e) F20 and (f) The relationship between band gap energy (E_{bg}) and weight of Fe_3O_4 (mg).

4.3.1.6 Photoluminescence Emission Spectrum

Photoluminescence (PL) emission spectrum is extensively conducted to study the electronic and optical properties of photoinduced semiconductor. It is beneficial that the faster electron transfer from the conduction band of a photoinduced semiconductor

to rGO sheets can prevent the recombination electron-hole rate. **Figure 4.8** demonstrated the room temperature PL spectra of rGO, Fe₃O₄/rGO and Fe₃O₄ (F20). From the PL spectra, it is obviously observed that the rGO and Fe₃O₄/rGO nanocomposites have exhibited lower PL intensity of the visible peak than that of the bare Fe₃O₄ nanoparticles (**Figure 4.8f**). Fe₃O₄ is an indirect band-gap semiconductor with a narrow band optical gap value of 1.4 eV (Beydoun et al., 2000). This narrowness value arises from the d orbitals indicated that Fe₃O₄ exhibits high electrical conductivity with almost metallic nature at room temperature, however, with the low charge carriers (electron and hole) mobility in magnetic nanoparticles may lead to an increase in electron-hole pair recombination. Hence, the higher PL intensity of the bare Fe₃O₄ nanoparticles is assigned to the recombination of excited electrons and holes, whereas the lower PL intensity of rGO and Fe₃O₄/rGO nanocomposites is because of the lower charge recombination rates. This reflects that graphene have the tendency to greatly influence the PL intensities of Fe₃O₄/rGO nanocomposites, owing to the 2D hexagonal π -conjugation structure and excellent electronic conductivity of graphene that have the tendency to greatly influence the PL intensities of the Fe₃O₄/rGO nanocomposites. The rGO consists of two different carbon domains, namely sp² and sp³ that has a different charge transition pathway inside each domain, respectively. Moreover, the PL emission of rGO depend on the shape, size and fractions of the sp² domains and sp³ domains, thus the π - π^* transition within the sp² carbon clusters cab be attributed to the PL quenching shifted in rGO (Han et al.). Amazing property such as the high charge mobility of graphene act as an electron acceptor for the photoinduced electron from Fe₃O₄ nanoparticles, and eventually leads to low charge recombination rate (Liu et al., 2011). Among the synthesized nanocomposites and rGO, the G1F2 has the lowest PL intensity, suggesting that G1F2 (**Figure 4.8a**) is efficiently suppresses the electron-hole pair recombination and promotes the charge separation and these are expected highly

beneficial for the photocatalytic performance rate. The synergistic effect (Y. Fu et al., 2011) between graphene and Fe_3O_4 nanoparticle in G1F2 nanocomposite allows graphene to trap or capture the photogenerated electrons from conduction band of Fe_3O_4 through the extended π -conjugation carbon network and consequently restricted the flash recombination electron-hole pair (L. Zhou et al., 2014). However, further increase the Fe_3O_4 content in the $\text{Fe}_3\text{O}_4/\text{rGO}$ nanocomposite results in a higher PL intensity. A high PL intensity of the visible peak for bare Fe_3O_4 nanoparticle in **Figure 4.8f** indicates high recombination rate. The large surface energies of Fe_3O_4 nanoparticles are tend to aggregate into large particles in order to minimize the surface energies (Meizhen Gao et al., 2011). Thus, adding excess amount of Fe_3O_4 nanoparticles in nanocomposite may introduce new charge centres for photoinduced charge separation and consequently minimize the photocatalytic efficiency. (Pawar et al., 2014; Zedan et al., 2010).

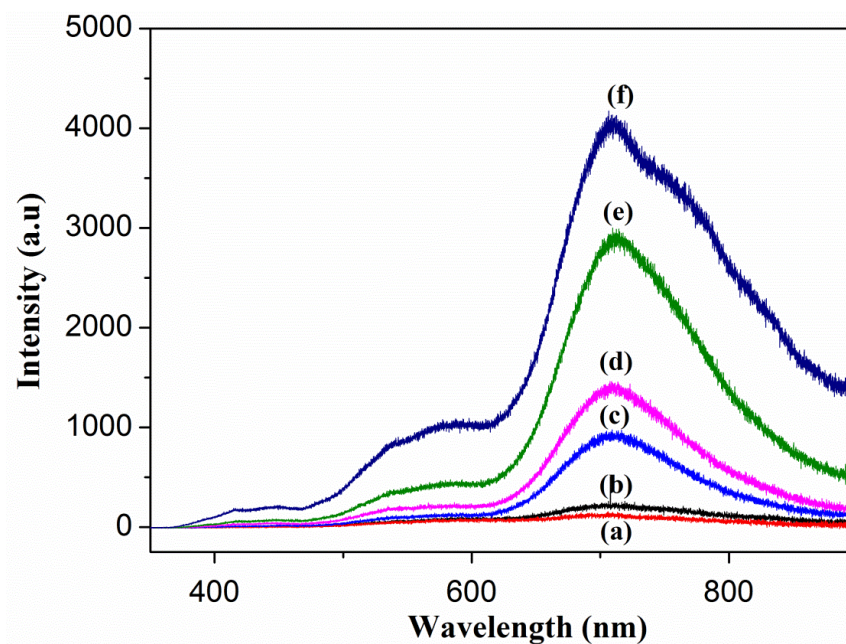


Figure 4.9: Room temperature photoluminescence (PL) spectra of (a) G1F2, (b) rGO, (c) G1F5, (d) G1F10, (e) G1F20 and (f) F20.

4.3.1.7 Vibrating Sampling Magnetometer (VSM) Studies

Study the magnetic behavior of the as-prepared magnetically separable $\text{Fe}_3\text{O}_4/\text{rGO}$ nanocomposites is one of the essential steps. Initially, the magnetic properties of $\text{Fe}_3\text{O}_4/\text{rGO}$ nanocomposites were evaluated by placing a permanent magnet next to the sample bottle. For the F20 sample, which containing only magnetite particles without any solvent, moved under magnetic field and attracted to the side of the sample bottle in a short period time (**Figure 4.9a**). In the case of sample G1F2 (**Figure 4.9b and 4.9e**), G1F2 was observed well dispersed in the aqueous solution and yet barely unaffected by the external magnetic field in with and without solvent, respectively. In contrast, composite of G1F20 amazingly was attracted to the side of the sample bottle spontaneously once placing the permanent magnet and leaving behind the transparent solvent. This phenomenon occurred in both water (**Figure 4.9c**) and ethanol (**Figure 4.9d**). Besides G1F2, as expected, G1F5 and G1F10 (image not shown) also experienced the same magnetic attraction as G1F20 in **Figure 4.9f**. Hence, this result suggests that the weight ratio between the GO and Fe^{2+} influences the magnetic behavior of prepared nanocomposites. When increasing the Fe^{2+}/GO weight ratio in the starting material, the Fe_3O_4 content in the nanocomposite as well increasing, quicker the separation of nanocomposite from the solution, is indicating an increase of magnetic sensitivity in nanocomposites.

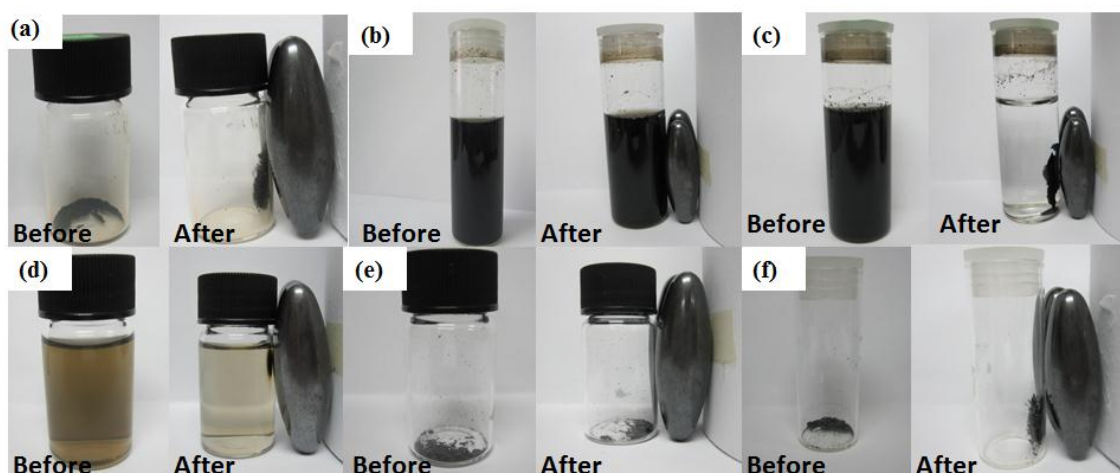


Figure 4.10: Images of magnetic property and dispersibility of the nanocomposites: (a) F20, (b) dispersed G1F2 unaffected by the magnetic attraction, (c) G1F20 in water (d) G1F20 in ethanol, (e) G1F2 and (f) G1F20.

The magnetic behaviour of these prepared nanocomposites were further studied using VSM. VSM analysis of both the bare Fe_3O_4 (F20) and Fe_3O_4 /rGO nanocomposites were carried out at room temperature and the results are represented in **Figure 4.10**. The magnetic hysteresis curves of both the Fe_3O_4 nanoparticles and Fe_3O_4 /rGO nanocomposites are typical Sigmoid-like (S-like) curves with no coercivity, inferring that they exhibit superparamagnetism behaviour and besides, this indicated that the magnetization behaviour diminished and become non-permanent magnet in the absence of applied magnetic field. Furthermore, the saturation magnetization (M_s) of Fe_3O_4 /rGO nanocomposites (**Figure 4.10 a-d**) significantly increased from 1.63 to 30.30 emu/g as increasing the content of Fe_3O_4 on the rGO sheets. The saturation magnetization of pure Fe_3O_4 nanoparticles (**Figure 4.10e**) with value of 58.70 emu/g was expected higher than that of magnetically separable Fe_3O_4 /rGO nanocomposites and this can be mainly attributed to the presence of graphene in the nanocomposites (Ren et al., 2011). The progressive increment of graphene content will increase the overall mass of the VSM sample and subsequently reduce the saturation magnetization since the measurement is per unit mass.

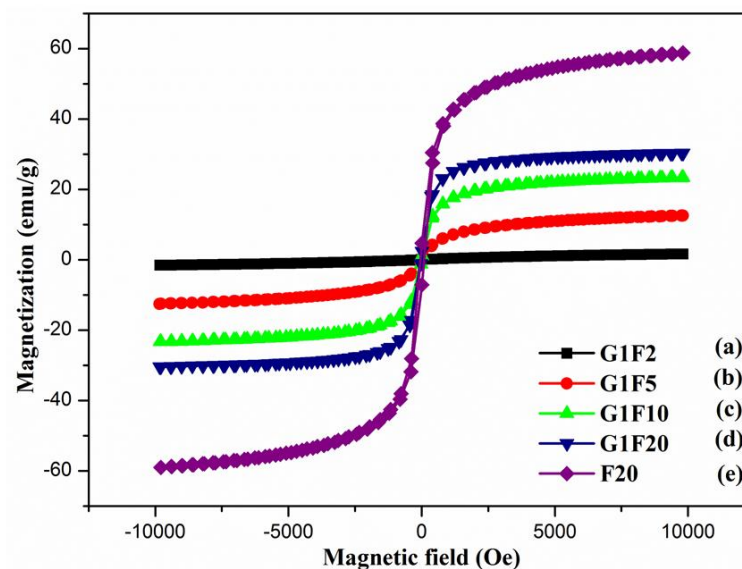


Figure 4.11: VSM magnetization curves of (a) G1F2, (b) G1F5, (c) G1F10, (d) G1F20 and (e) F20.

4.4 Part III

4.4.1 Photocatalytic application of $\text{Fe}_3\text{O}_4/\text{rGO}$ nanocomposites

The photocatalytic activity of the synthesized photocatalysts such as Fe_3O_4 (F20) nanocrystals and magnetically separable $\text{Fe}_3\text{O}_4/\text{rGO}$ nanocomposites were investigated towards the degradation of a model organic dye pollutant, methylene blue (MB) under 5 h of natural sunlight irradiation. **Figure 4.11** depicts the results of the photodegradation study for the as-synthesized photocatalyst materials. During photocatalytic measurements, the bare Fe_3O_4 nanoparticles showed only of 57% of photodegradation activity even after 5 h of exposure to natural solar light (**Figure 4.11a**). The poor photocatalytic performance of bare Fe_3O_4 nanoparticles can be related to the heavy aggregation of magnetite which caused by the high surface energies area Fe_3O_4 nanocrystals. As a consequence, the magnetic interactions between these magnetic particles lead to the agglomeration to form particle with (W. Wu et al., 2008). Fascinatingly, an optimum and maximum photodegradation of MB was achieved at the

first hour light irradiation for the photocatalyst which Fe_3O_4 nanoparticles incorporated on the rGO sheets. Hence, the photocatalytic measurements were performed with different ratio compositions of rGO and Fe_3O_4 to optimize the Fe_3O_4 content for maximum photodegradation of MB dye. Among the photocatalysts, the G1F2 showed excellent photocatalytic activity and almost 89 % MB was decolorized upon 30 min and 100 % after 1 h sunlight irradiation, whereas, the G1F5, G1F10 and G1F20 were showed almost 100 % degradation of MB after 2 h of irradiation. In contrast, the bare Fe_3O_4 nanoparticles were only achieved 57% MB removal efficiency. The maximum photocatalytic performance by the $\text{Fe}_3\text{O}_4/\text{rGO}$ can be ascribed to the emergence of the synergistic effect between Fe_3O_4 and rGO during the catalytic reaction. The efficient transfer of photogenerated charge from Fe_3O_4 to graphene sheets facilitates increased and fast electron-hole pair separation and consequently a better achievement of photocatalytic performance.

To further investigating the enhanced photocatalytic performance of the $\text{Fe}_3\text{O}_4/\text{rGO}$ nanocomposites, the photocatalytic experiments were conducted in the dark which the MB solution was stirring continuously with photocatalysts overnight (12 h) and the observations are shown in **Figure 4.11b**. The rGO and G1F2 showed maximum adsorption of almost 86 and 84 %, respectively. The sample with lower content of magnetite allows better transmission of light, which is crucial for the photocatalytic performance. However, further increasing the Fe_3O_4 content in the nanocomposites is leading to a decrease of MB adsorption. The shadowed area in the Figure 4.11a follows the similar trend to the adsorption behaviour of the photocatalysts. The excellent and enhanced dye adsorptivity of $\text{Fe}_3\text{O}_4/\text{rGO}$ photocatalysts is mainly attributed to the existence of the large phenyl ring structure of graphene in the nanocomposites (Matsumoto et al., 2011). Additionally, the 2D hexagonal crystalline structure graphene possess large surface area, superior electrical conductivity and unique transport

property; make it as a great electron-transport candidate in the process of photocatalysis. When the magnetite particles distributed on the surface of rGO sheets, the graphene provides facial adsorption sites and photocatalytic reaction centres for the organic dye MB molecules via π - π conjugation between MB dye and aromatic region of graphene sheets (Y. S. Fu et al., 2012; L. W. Zhang et al., 2010). These highly exposed surface active reaction sites are beneficial to generate of oxidative species such as hydroxyl radicals for MB adsorption by the redox reaction within the active sites ($\text{Fe}^{2+}/\text{Fe}^{3+}$). Moreover, the strong Fe-O-C interaction of $\text{Fe}_3\text{O}_4/\text{rGO}$ between the delocalized unpaired π electrons from π -conjugated carbon network on graphene's basal plane facilitates the electron-transfer between rGO sheets and iron centres (Jasuja et al., 2010). Therefore, the concentration of photoinduced of charge carriers deeply affects the photocatalytic activity during the reaction. The strong attachment of Fe_3O_4 on electron carriers of rGO sheets and fast electron-transfer kinetic of $\text{Fe}_3\text{O}_4/\text{rGO}$ attempt to facilitate the enhanced migration of photogenerated electrons from the conduction band of Fe_3O_4 to rGO sheets and improve the interfacial charge transfer process, leading to a better photocatalytic activity (Mukherji et al., 2011). In contrast, the strong anisotropic dipolar interactions of Fe_3O_4 in aqueous phase may diminish their catalytic activity; hence, Fe_3O_4 nanoparticles have a great tendency to aggregate into large particles (**Figure 4.3b**), results to the decreased MB decolourization efficiency.

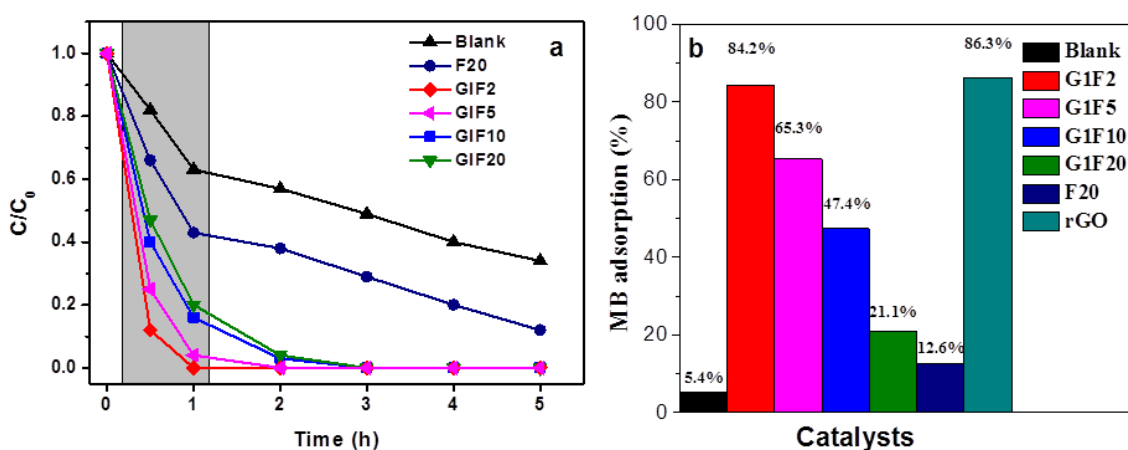


Figure 4.12: (a) Photocatalytic degradation rate of MB in the presence of different photocatalysts under natural sunlight irradiation. (b) Adsorption of MB solution by different catalysts after 12 h stirring.

4.4.2 Durability Test Studies of Fe₃O₄/rGO nanocomposites

The sustainability of a photocatalyst is one of the most crucial and essential requirements for successful practical applications. In this section, the reusability of Fe₃O₄/rGO photocatalyst was evaluated by using the same photocatalyst for 8 cycles of experiments with fresh MB solution at each measurement and maintained all the experimental with similar parameters. The photocatalyst was removed from the photocatalysis cell by applying external magnetic field and followed by washed with high pure DI water to remove the presence of any intermediate compounds from the degradation of MB. The magnetic separation technique offers an easy, simple and convenient way to remove or recycle the photocatalyst by only placing a permanent magnetic bar close to the sample bottle and subsequently, the Fe₃O₄/rGO will align with external magnetic field and attracted to the side of the bottle in a short period, leaving behind a transparent and clear solution system (**Figure 4.12d**). Thus, magnetic separable Fe₃O₄/rGO catalysts are easily repeated and recycled after photocatalytic reaction. Notably, the MB dye molecules are effectively photodecomposed in measurement cycle and TEM images provide strong evidence that Fe₃O₄/rGO remain no

significant change observed in morphology property after the 8 sets of repeated photocatalytic experimental cycles (**Figure 4.13**).

Among all the Fe₃O₄/rGO photocatalysts, sample G1F2 displayed the best stability during the photodegradation of MB dye and hence G1F2 is potential to be used as a recyclable photocatalyst in the wastewater treatment application (**Figure 4.12a**). A lower content of magnetite particles in the nanocomposites may contribute to the smaller the particle sizes with high surface area without problem of heavy aggregation of Fe₃O₄ nanoparticles and thus offer enhanced decolourization MB efficiency. Besides, the brownish nature of Fe₃O₄ nanoparticles also inhibits the light transmission. Hence, the lower content of magnetite in the nanocomposites exhibits the better photocatalytic performance. G1F2 consists of the lowest amount of Fe₃O₄ particles possess the smaller particles size with the highest specific surface area, which can offer numbers of active sites for adsorption and desorption of MB molecules in the nanocomposites, promotes the facile transport of photoexcited electrons to reach at the surface reaction sites more easily and thereby effectively inhibited the recombination of photogenerated electron-hole pairs during the electron-transfer process. In a nutshell, high enhanced photocatalytic efficiency and good sustainability of Fe₃O₄/rGO composite could be considerable as a beneficial and promising candidate for industrial environmental remediation process.

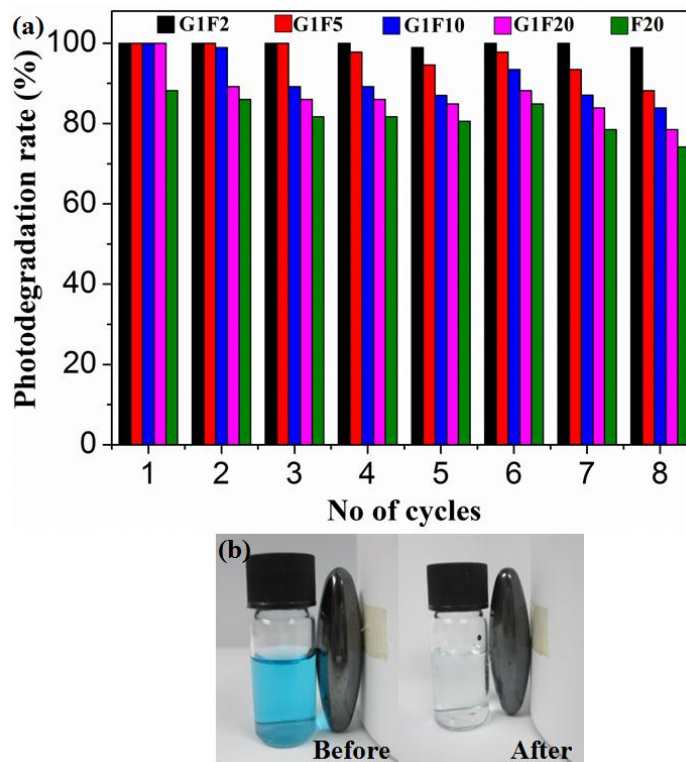


Figure 4.13: (a) Photodegradation efficiency (%) of MB solution for 8 cycles in the presence of $\text{Fe}_3\text{O}_4/\text{rGO}$ nanocomposites and Fe_3O_4 . (b) Photographic images of MB before and after degradation by $\text{Fe}_3\text{O}_4/\text{rGO}$ and recovery by applying a permanent magnet.

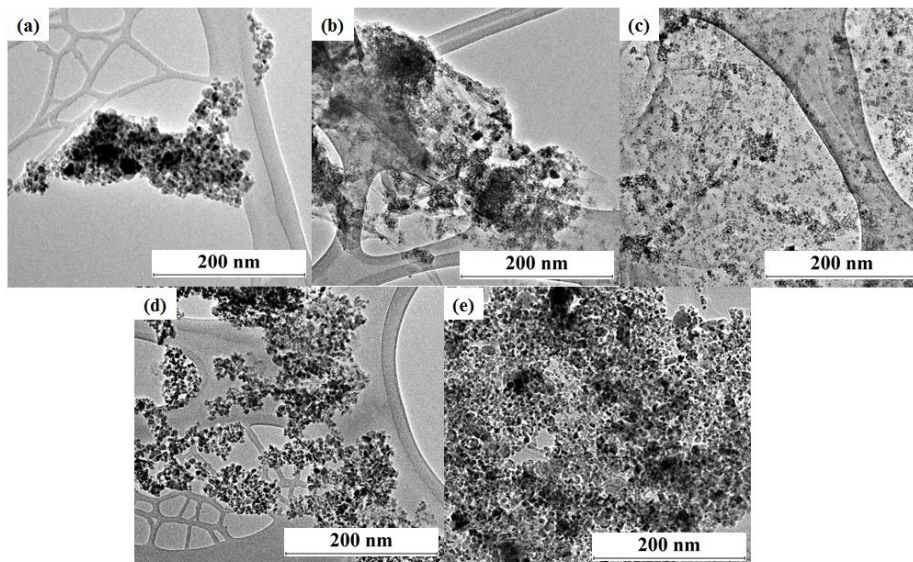


Figure 4.14: HR-TEM images of (a) F20, (b) G1F2, (c) G1F5, (d) G1F10 and (e) G1F20.

4.4.3 Mechanism for the Photocatalytic Studies of Fe₃O₄/rGO nanocomposites

Figure 4.14 presented the mechanism for the enhancement MB of the photodegradation by the introduction of magnetically separable Fe₃O₄/rGO photocatalysts under natural sunlight irradiation. The band-edge potential level is one of the important criteria in the photoexcited charge carriers for determining the photocatalytic efficiency. Upon light irradiation, Fe₃O₄ anchored on the rGO sheet undergoes charge separation, an electron-hole pair produced between valence and conduction band of Fe₃O₄, and subsequently leading to the promotion of valence band (VB) electrons into the conduction band (CB), leaving behind a hole in the VB (Eqn. (1)). Meanwhile, the MB molecules were excited to cationic MB radicals (MB*) (Eqn. (2)). These photo-induced electrons that trapped in the conduction band are good reductants (+0.5 to -1.5 V vs NHE) were instantaneously transferred to rGO sheets (Eqn. (3)) and consequently captured by the dissolved O₂ on the Fe₃O₄ surface to generate some reaction oxidation species, including superoxide radical (O₂^{•-}) and hydroxyl (•OH) (Eqn. (4)) under the band gap potential difference. On the other hand, the photogenerated holes are important and powerful oxidants (+1.0 to 3.5 V vs NHE) in the oxidation process and it can effectively oxidizes the adsorbents, usually it react with adsorbed H₂O/OH⁻ to produce strong hydroxyl radicals (•OH) (Eqn. (5)). The Fe₃O₄/rGO photocatalyst have sufficient band gap energy to photo-degrade the organic pollutants which the oxidation potential of the H₂O/•OH reaction (OH⁻ → •OH + e⁻; E⁰ = 2.8 V vs NHE) and the reduction potential superoxide radicals (O₂/O₂^{•-}; E⁰ = -0.28 V vs NHE) lies within the band gap of the Fe₃O₄/rGO (Beydoun et al., 1999; Hoffmann et al., 1995; Z. Zhang et al., 2012). Finally, these produced •OH radicals have high oxidative potential to oxidize MB molecules adsorbed via π-π stacking/electrostatic interactions to CO₂ and H₂O (Harifi et al., 2014) on the active sites of Fe₃O₄/rGO nanocomposites (Eqn. (6)).

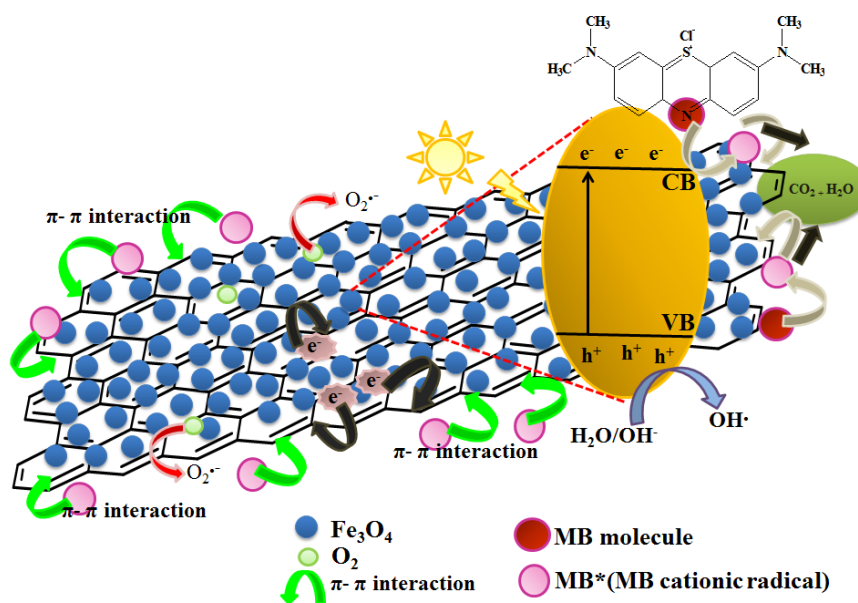
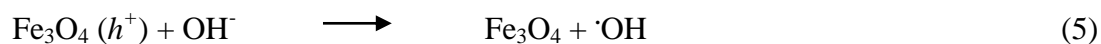


Figure 4.15: Schematic representation of photodegradation of MB by $\text{Fe}_3\text{O}_4/\text{rGO}$ nanocomposites under natural sunlight irradiation.

4.4.4 Electrochemical Application for Simultaneous Detection Dopamine (DA) and

Ascorbic Acid (AA)

4.4.4.1 Electrochemical Behaviour of $\text{Fe}_3\text{O}_4/\text{rGO}$ Nanocomposites

The electrochemical behaviour of as-modified electrodes were evaluated to elucidate their electron transfer property in the presence $\text{K}_3[\text{Fe}(\text{CN})_6]$, which act as a

redox probe. The cyclic voltammograms (CVs) of the different modified electrodes were showed in the presence of 5 mM of $K_3[Fe(CN)_6]$ and 0.1 M KCl at a scan rate of 100 mV/s, are shown in **Figure 4.15A** and **4.15B**, respectively. A pair of well-defined redox peak is observed with a peak to peak separation (ΔE_p) of 140 mV for bare GCE (**Figure 4.15A (a)**), whereas ΔE_p exhibited by the $Fe_3O_4/rGO/GCE$ at about 89 mV (**Figure 4.15A (b)**). Obviously, the redox peak current for the $Fe_3O_4/rGO/GCE$ has significantly increases 3-fold higher as compared to the bare GCE. This improved electrochemical behaviour can be related to the excellent electrical conductivity of Fe_3O_4/rGO on the GCE surface. Moreover, the superior electrical conductivity and unique electron transport property of graphene accelerates the electron transfer rate at electrode/electrolyte interface. On the other hand, the ΔE_p for the $Fe_3O_4/rGO/GCEs$: G1F2/GCE, G1F5/GCE, G1F10/GCE, G1F20/GCE is about 120, 89, 99, 138 and 230mV, respectively (**Figure 4.15B (a-d)**). Only at F20/GCE (**Figure 4.1B (e)**), the lowest redox peak current is observed than that of the $Fe_3O_4/rGO/GCE$, owing to the easily oxidized Fe_3O_4 nanoparticles possess high surface energies that subsequently leads to the rapid aggregation to larger particles, blocking the electron transfer at the electrode surface. At a low content of Fe_3O_4 in composite G1F2, the current peak is lower compared to the other composites. When increasing the amount of magnetic nanoparticles (Fe_3O_4) in the nanocomposite, the peak current is dramatically increased, indicating Fe_3O_4 plays crucial role in the increase of the electroactive surface area that improving the electrochemically active surface and accelerates relatively rapid electron transfer rate at modified electrode surface (Y. X. Zhang et al., 2013). However, the current response is decrease when the Fe_3O_4 content reached the optimum level, such as G1F10 and G1F20. This results can be attributed to the heavy aggregation of large Fe_3O_4 particles in nanocomposite, which having the same situation as in the F20/GCE, which may diminish the electrochemical behaviour of the modified electrode and hence

exhibits electrochemically inactive nature (Lian et al., 2010; Pan et al., 2012; Peng et al., 2012).

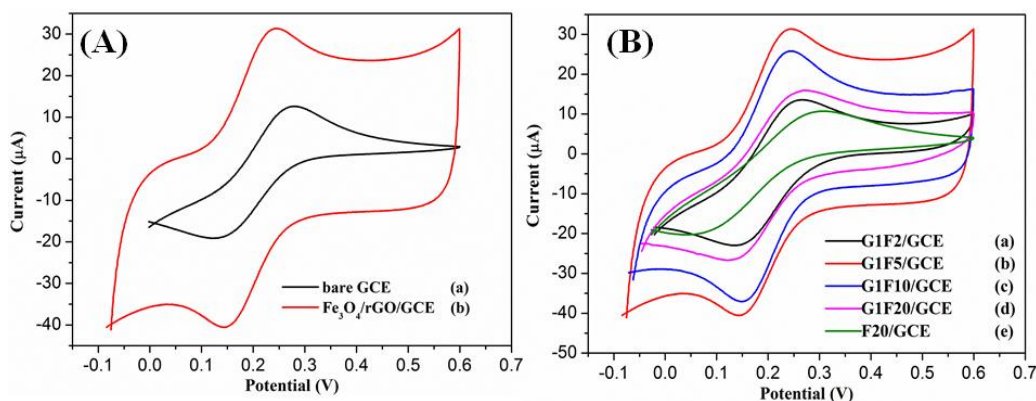


Figure 4.16: (A) Cyclic voltammograms obtained for (a) bare GCE and (b) Fe₃O₄/rGO/GCE in the presence of 5 mM K₃[Fe(CN)₆] and 0.1 M KCl solution at a scan rate of 100 mV/s. (B) Cyclic voltammograms obtained for (a) G1F2/GCE and (b) G1F5/GCE, (c) G1F10/GCE, (d) G1F20/GCE and (e) F20/GCE in the presence of 5 mM K₃[Fe(CN)₆] and 0.1 M KCl solution at a scan rate of 100 mV/s.

4.4.4.2 Electrochemical Impedance Spectroscopy (EIS) of Modified Electrodes

Electrochemical impedance spectroscopy (EIS) is an effective tool to probe the interfacial properties of chemically modified electrodes. **Figure 4.16** presented the Nyquist plots observed for the different modified electrodes in the presence of 5 mM K₃[Fe(CN)₆]/K₄[Fe(CN)₆] (1:1) solution containing 0.1 M KCl in the frequency range from 10⁻¹ to 10⁴ Hz. Regarding to the EIS spectra, Randels equivalent circuit was used when the electrode processes involving both kinetic and diffusion to obtain the circuit element values including charge transfer resistance (R_{ct} Ω), where the R_s , R_{ct} , W and Q_{CPE} refer to the solution resistance, charge transfer resistance, Warburg impedance and constant phase element, respectively and the corresponding parameters are summarized in **Table 4.1**. The rGO/GCE (**Figure 4.16A (b)**) displayed a straight line, revealing that graphene sheets exhibit large surface area and good conductivity that facilitating the rate

of electron transport process at electrode surface. In comparison with $\text{Fe}_3\text{O}_4/\text{rGO}/\text{GCEs}$ (Figure 4.16B (a-d)), the F20/GCE (Figure 4.16A (d)), demonstrated a large and remarkable increase in the diameter of semicircle. This high resistance (9.95 k Ω) might assign to the aggregated Fe_3O_4 which could diminish the electron transfer process. However, coupling the magnetite (Fe_3O_4) particles with graphene sheets, the EIS of these $\text{Fe}_3\text{O}_4/\text{rGO}$ modified electrodes display almost a straight line, indicates low interfacial electron transfer resistance and it promotes the electron transfer process of the nanocomposites, due to the larger surface area and excellent electrical conductivity of the $\text{Fe}_3\text{O}_4/\text{rGO}$ nanocomposites (C. J. Fu et al., 2014; Y. X. Zhang et al., 2013).

Table 4.1: EIS fitting parameters for modified electrodes.

<i>Electrochemical impedance fitting parameters</i>				
Electrodes	R_s (Ω)	Q_{CPE} (F)	R_{ct} (Ω)	W
G1F5	197.2	1.26×10^{-3}	3.7×10^{-3}	3.56×10^{-4}
F20	182.8	1.98×10^{-6}	9952	1.11×10^{-4}

Foot note: R_s – Solution resistance; Q_{CPE} – constant phase element; R_{ct} – Charge transfer resistance; W – Warburg impedance.

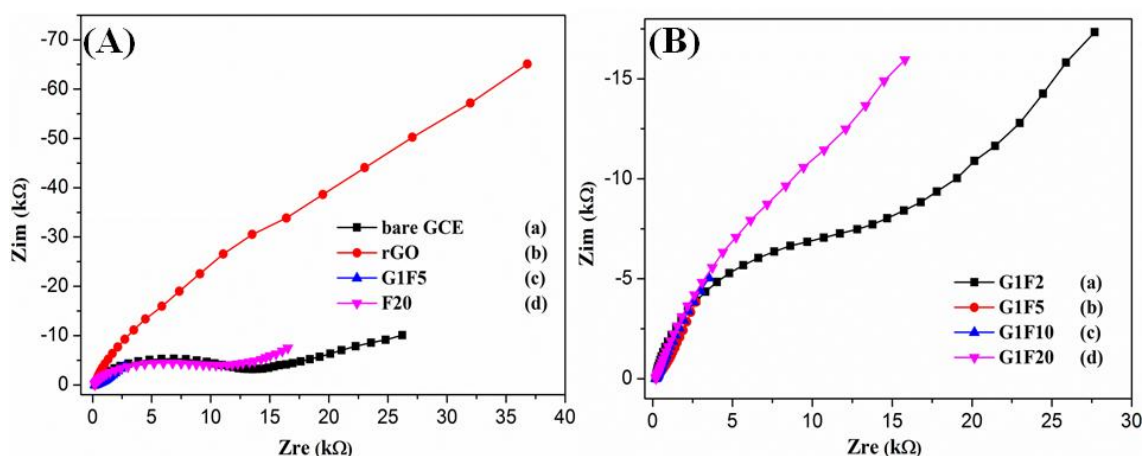


Figure 4.17: (A) Nyquist plots obtained for (a) bare GCE, (b) rGO, (c) G1F5 and (c) F20; (B) Nyquist plots for $\text{Fe}_3\text{O}_4/\text{rGOs}$ (a) G1F2, (b) G1F5, (c) G1F10 and (d) G1F20 in the presence of 5 mM $\text{K}_3[\text{Fe}(\text{CN})_6]/\text{K}_4[\text{Fe}(\text{CN})_6]$ (1:1) solution containing 0.1 M KCl.

(C) Equivalent electrical circuit for (a) F20 and (b) G1F5.

4.4.4.3 Electrocatalytic Response of Modified Electrodes towards the Oxidation of Dopamine (DA)

The electrocatalytic behaviour of as-modified electrodes in the presence of 0.1 mM DA in 0.1 M PBS (pH 6.5) was studied using cyclic voltammetry (CV) technique at a scan rate of 100 mV/s. **Figure 4.17 (Inset)** displays the CV responses obtained for the bare GCE, Fe₃O₄/rGO/GCE and F20/GCE in the presence of 0.1 mM DA. The bare GCE showed a well-defined redox peak with the anodic and cathodic peaks at 257 mV and 148 mV, respectively. Meanwhile, the oxidation peak current of Fe₃O₄/rGO/GCE was increased remarkably and the oxidation peak potential was shifted negatively. For the Fe₃O₄/rGO/GCEs (**Figure 4.17**), the dramatically increased in peak currents and negatively shifted oxidation peak potentials were observed for the electrocatalytic oxidation of DA in the sequence of: G1F5/GCE > G1F10/GCE > G1F20/GCE > G1F2/GCE. Among the Fe₃O₄/rGO/GCEs, the G1F5/GCE (**Figure 4.17b**) exhibits the most enhanced electrochemical performance towards the electrocatalytic oxidation of DA. The oxidation peak potential was negatively shifted to 234 mV with a significantly improved 30-fold oxidation peak current of 60.98 μ A in the comparison to the F20/GCE (2.87 μ A) and bare GCE (2.79 μ A). These results coincide with the observation from EIS (**Figure 4.17**) and indicate that the significantly improved electron transfer property and high electrocatalytic activity are beneficial for the DA oxidation. Hence, the existence of graphene is an ideal support material and effectively acts as an electron promoter in the electrocatalytic oxidation of DA. The good synergistic effects emerged between the magnetic particles (Fe₃O₄) and rGO sheets greatly enhance the conductive area and electron transfer rate between DA molecules and electron surface.

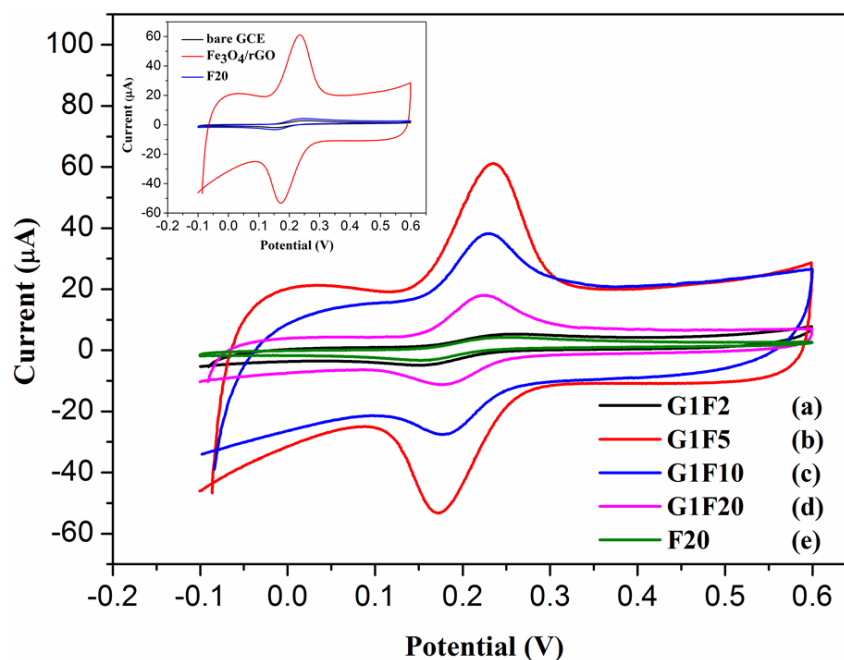


Figure 4.18: CVs for (a) G1F2, (b) G1F5, (c) G1F10, (d) G1F20 and (e) F20, in the presence of 0.1 M PBS (pH 6.5) containing 0.1 mM DA at a scan rate of 100 mV/s. Inset: Electrochemical detection of 0.1 mM DA for bare GCE, Fe₃O₄/rGO and F20.

4.4.4.4 Mechanism for the Electrocatalytic Oxidation of Dopamine (DA) at Modified Electrodes

Figure 4.18 shows the study of redox electrochemistry of dopamine (DA) and its oxidized form, dopaminequinone (DAQ) and the proposed mechanism (Angeles et al., 2008) for the electrocatalytic oxidation of DA. DA is easy to oxidize electrochemically and it form DAQ. When potential is applied to the modified electrode, DA oxidized electrochemically and formed DAQ after exchange of 2 electrons and 2 protons. These electrons were subsequently donate to the electrode and produce faradaic current (Barnes et al., 2010; Huang et al., 2012).

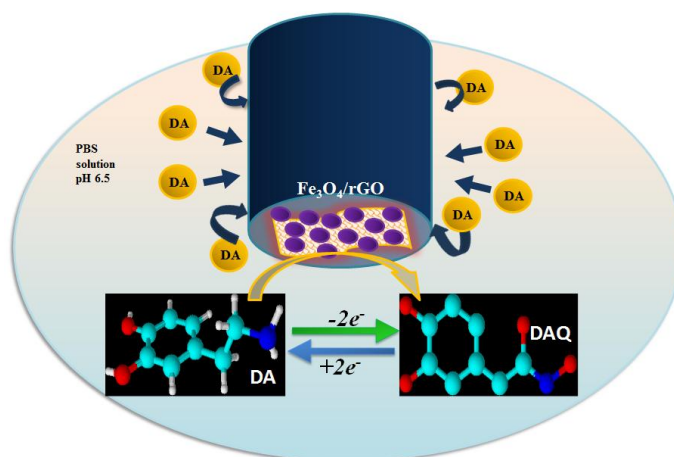


Figure 4.19: Electrocatalytic oxidation of dopamine at $\text{Fe}_3\text{O}_4/\text{rGO}/\text{GCE}$ electrode (N. Li et al., 2013).

4.4.4.5 Influence of Scan Rate on the Electrocatalytic Oxidation of DA at G1F5/GCE Electrode.

Figure 4.19 shows the influence of scan rates on the electrocatalytic oxidation of DA in the presence of the G1F5/GCE electrode to investigate the reaction kinetic of DA on the modified electrode. It is obviously observed that the oxidation peak currents are increased linearly and the oxidation peak potential was shifted positively with scan rate in the range of 100-300 mV/s (**Figure 4.19A**). From the CVs of oxidation DA at modified electrode, both redox peak currents (I_{pa} and I_{pc}) are linearly proportional to the scan rates, with linear equations expressed as I_{pa} (μA) = 0.2917 + 5.144v (mV/s) ($n=10$, $R^2=0.9997$) and I_{pc} (μA) = 0.3022 - 2.061v (mV/s) ($n=10$, $R=0.9997$), respectively (**Fig. 4.19B**). This observation indicates that the electrocatalytic oxidation of DA at G1F5/GCE is a typical surface adsorption-controlled process. For an adsorption-controlled process, the charge transfer coefficient (α) and apparent heterogeneous electron transfer rate constant (k_s) can be calculated from the variation of E_{pa} and E_{pc} with the logarithm of the scan rate (**Figure 4.19C**) by using Laviron's model. In **Figure 4.19D**, two linear regression equations of E_{pa} and E_{pc} on $\log v$ were plotted and

expressed as $E_{pa} (v) = 0.1053 \log v + 0.0087$ ($R^2 = 0.995$) and $E_{pc} (v) = -0.1001 \log v + 0.4035$ ($R^2 = 0.994$), respectively. The results demonstrated that the E_p values were proportional to the logarithm of the scan rates that higher than 600 mV/s. The slope of the linear equation is equal to $-2.3RT/\alpha nF$ and $2.3RT/(1-\alpha)nF$, which is assigned to the cathodic and anodic peak, respectively and as a consequence used to evaluate the kinetic parameters, α_c and α_a . R the gas constant ($8.314 \text{ JK}^{-1} \text{ mol}^{-1}$), T (293 K) and F the Faraday constant ($96,485 \text{ C mol}^{-1}$) from the linear equation refer to gas, temperature and Faraday constant. The anodic transfer coefficient (α_a) is calculated to be 0.44 while the electron transfer rate constant (k_s) was evaluated to be 2.09 s^{-1} by using the following Laviron's equation (Laviron, 1979):

$$\log k_s = \alpha \log(1 - \alpha) + (1 - \alpha) \log \alpha - \log \frac{RT}{nFv} - \frac{\alpha(1 - \alpha)nF\Delta E_p}{2.3RT}$$

Since the calculated K_s value was higher than the previously reported values (N. Li et al., 2013; W. Sun et al., 2012; Z. Zhu et al., 2010), and hence it indicates that the G1F5/GCE performed rapid electron transfer rate towards the electro-oxidation of DA.

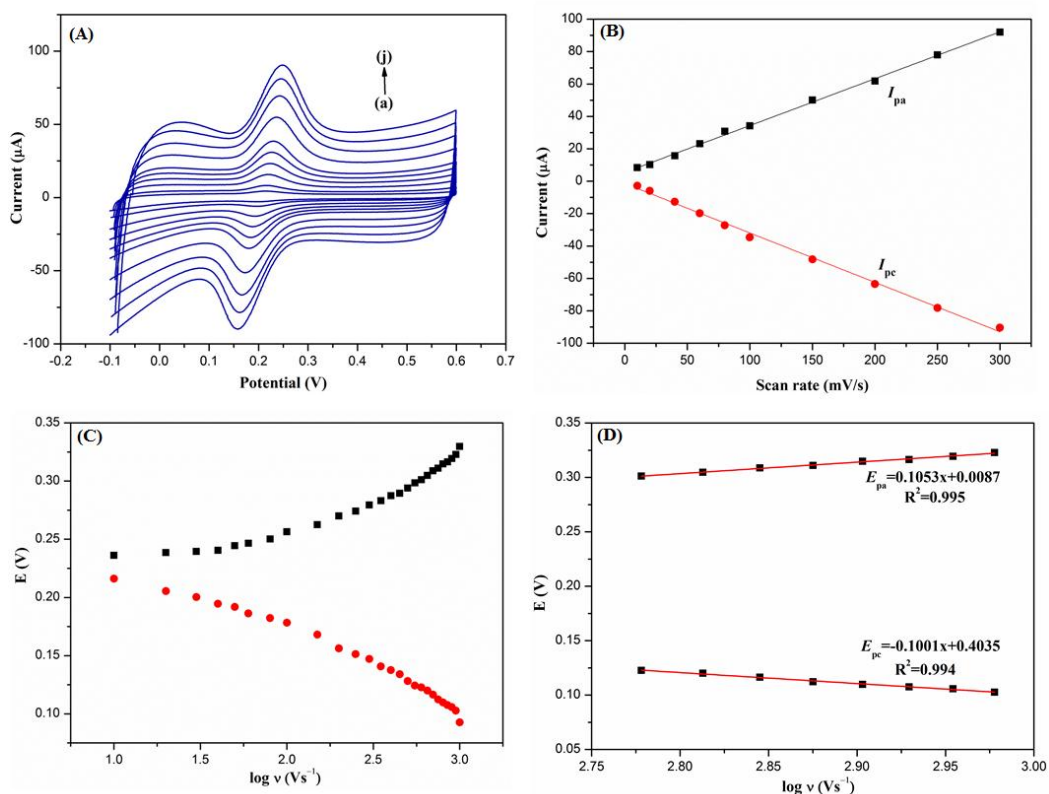


Figure 4.20: (a) CVs observed for G1F5/GCE in 0.1M PBS (pH 6.5) containing 0.1 mM DA at various scan rates ((a) –(j): 10, 20, 40, 60, 80, 100, 150, 200, 250 and 300 mV/s). (b) The plots of peak current vs. the scan rates. (c) Variation of E_p vs. the logarithm of scan rate. (d) Variation of E_p vs. the logarithm of the high scan rates: 600, 650, 700, 750, 800, 850, 900 and 950 mV/s).

4.4.4.6 Studies of G1F5 Concentration on the Electrocatalytic Activity of DA

The concentration of G1F5 suspension loading on the electrode surface greatly influences the electrocatalytic activity of DA. During the electrochemical measurement, the G1F5 volume was initially fixed at 5 μ L. From the observation in **Figure 4.20**, the oxidation peak current of DA was significantly increased when the concentration of G1F5 suspension increased from 0.25 mg/mL to 1.5 mg/mL due to the enhancement of the conductive surface area promotes the electron transfer rate. However, further increment of G1F5 suspension above 1.5 mg/mL leads to a dramatically decrease in the oxidation peak current of DA, owing to the mass transport limitation of DA inside a

thicker film (Qu et al., 2007). Additionally, the shifting of the oxidative over-potential towards more electropositive regions has caused a decreased current response may be attributed to an increased mass of graphene on the electrode surface beyond the optimum level (Brownson et al., 2011). Thus, 1.5 mg/mL of G1F5 suspension was chosen to deposit on the modified electrode for electrochemical detection.

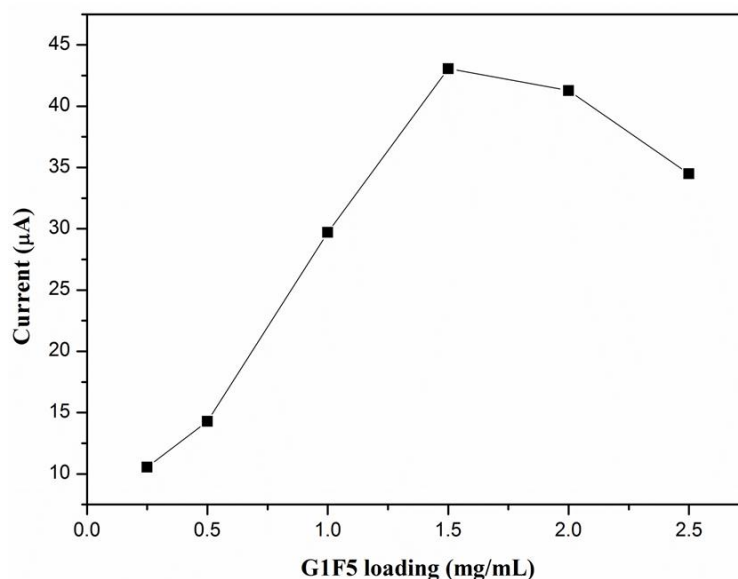


Figure 4.21: Effect of G1F5 amount of electro-oxidation current response of 0.1 mM DA in 0.1 M PBS (pH 6.5) at a scan rate of 100mV/s.

4.4.4.7 Selective Determination of Dopamine (DA) In The Presence of Ascorbic Acid (AA)

The selectivity of G1F5/GCE electrochemical sensor was investigated under the presence of interfering species, ascorbic acid (AA) in 0.1 M PBS containing 0.1 mM DA. **Figure 4.21** displays the DPV responses of simultaneously determination of DA and AA at the bare GCE and G1F5/GCE, respectively. The bare GCE showed the significant overlapping and undefinable oxidation peak potentials of DA and AA during the simultaneous detection of both species DA and AA, due to the poor selectivity. During the detection, AA is directly interfered with DA, resulting the bare GCE fails to

determine the individual electrochemical peaks for DA and AA (**Figure 4.21a**). Surprisingly, G1F5/GCE demonstrated the obviously increased peak current for DA; meanwhile the overlapped peak is resolved and clearly displayed the individual oxidation peaks for DA and AA at about 0.19 and 0.025 V, respectively (**Figure 4.21b**). Furthermore, the strong electrostatic interaction and π - π conjugation between the aromatic regions of positively charged DA and negatively charged G1F5 composite initiates and accelerates the electron transfer to enhance the electrocatalytic oxidation of DA to electron surface. Therefore, AA oxidation is inhibited and deactivated because of the repulsion of negatively charged interferences are promoted (L. Wu et al., 2012). **Figure 4.21** reveals the G1F5/GCE exhibited excellent electrocatalytic activity towards the oxidation of DA than AA and exert no interference in the selective determination of DA.

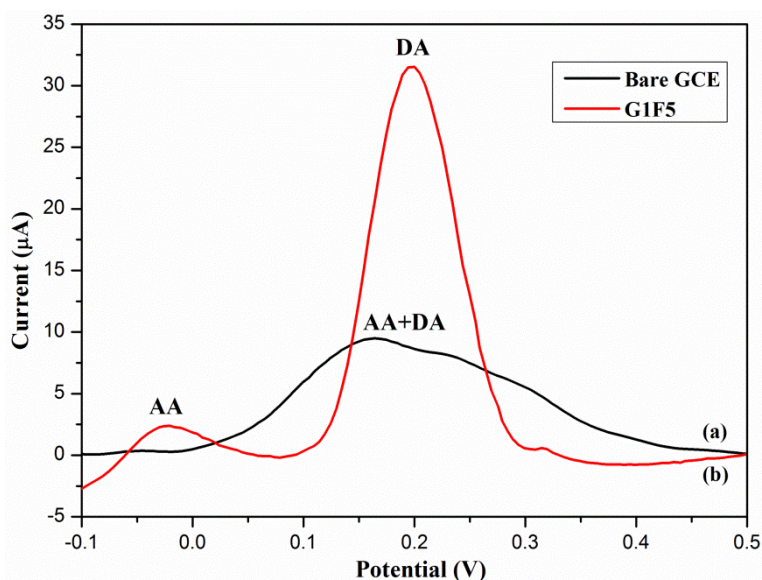


Figure 4.22: DPV response observed for (a) bare GCE and (b) G1F5/GCE electrodes in the presence of 0.1 mM of DA and 3 mM of AA in 0.1 M PBS (pH=6.5).

The electrochemical detection of DA is further evaluated by differential pulse voltammetry (DPV) under the presence of AA. **Figure 4.22A** shows a series of DPV

curves for the electro-oxidation peak currents obtained for the various concentration of DA at a fixed concentration of 2 mM AA at G1F5/GCE. The DPV peak current of DA is linearly proportional with the increasing concentration of DA in solutions and two well-defined and distinguished peaks correspond to the AA and DA are recorded at about -46 and 189 mV, respectively. Interestingly, the anodic peak of AA is almost stable and no obvious change for peak current AA during the detection with the DPV curve. Hence, the coexisting species AA has no induced interference influence in the determination of DA at G1F5/GCE modified electrode.

Figure 4.22B demonstrates the I_{pa} vs. DA concentration curve in the range of 0-100 μM . The linear regression equation was plotted and expressed as $I_{DA} (\mu\text{A}) = 15.64 + 2.733C (\mu\text{M})$ with a correlation coefficient of 0.996 and a sensitivity of 2.733 $\mu\text{A}/\mu\text{M}$. The limit of detection (LOD) was calculated to be 0.12 μM with signal to noise ratio of 3. Similarly, the electrochemical determination of AA was also evaluated by varying the AA concentration while keeping the DA concentration as constant (0.1 mM DA) as shown in **Figure 4.22C**. The oxidation peak current of AA increases proportionally with the increasing AA concentration. Furthermore, two different linear segments were observed in the calibration plots of peak currents versus AA concentration in the presence of 0.1 mM DA, which is corresponding to two different ranges of substrate concentration. The first linear segment ($I_{AA} (\mu\text{A}) = 62.41 + 1.576 C (\text{mM})$) corresponds to AA concentration from 1-9 mM, while the second linear segment ($I_{AA} (\mu\text{A}) = 71.07 + 0.6118 C (\text{mM})$) corresponds to AA concentration from 9-25 mM (**Figure 4.22D**). The decrease in sensitivity (slope) at higher linear range of AA is related to the kinetic limitation of the G1F5 (Ardakani et al., 2010). The limit of detection for the AA in lower and higher ranges is found to be 0.42 μM and 2.77 μM , respectively. Furthermore, shift in the peak potential of AA is likely due to the acidic nature of AA that affects and changes the pH of the solution when excess AA was added (M. Gao et al., 2013; How et

al., 2014). In comparison with other works (**Table 4.1**), it is noteworthy to mention that the modified electrode based on Fe₃O₄/rGO nanocomposite in the present study greatly increases their electrocatalytic active sites and accelerates and initiates the electron transfer in simultaneous detection of AA and DA. Additionally, the reproducibility of the G1F5/GCE modified electrode was carried out by the repetitive electrochemical measurements in the 0.1 M PBS (pH 6.5) solution containing 0.1 mM DA. The G1F5/GCE gives a relative standard deviation (R.S.D) of 3.0 % after 10 successive measurements, implying that the good reproducibility and stability of the modified electrode.

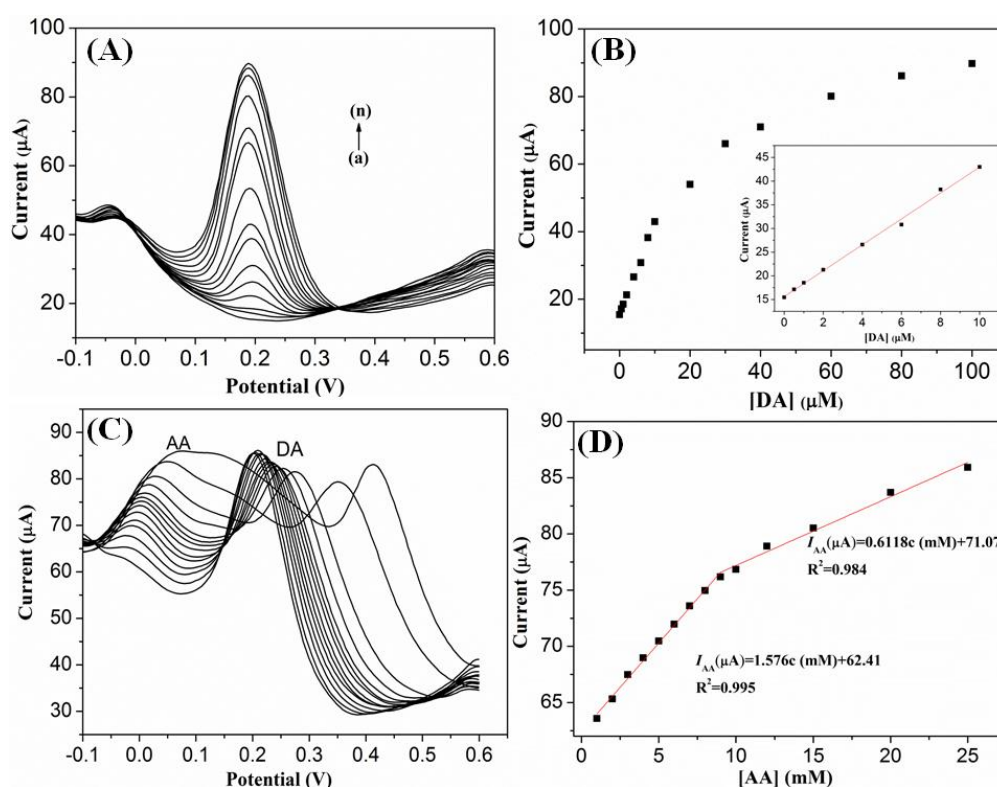


Figure 4.23: (A) DPV response of G1F5/GCE modified electrode with increasing the concentration of DA (from a to n: 0, 0.5, 1, 2, 4, 6, 8, 10, 20, 30, 40, 60, 80 and 100 μM) in the presence of 2 mM AA. (B) The relationship between the oxidation peaks current against DA concentration (0.5–100 μM) in the presence of 2 mM AA. Inset: Enlarge view of calibration plot in the concentration range of 0–10 μM of DA. (C) DPVs response of G1F5/GCE modified electrode with various concentrations of AA (1–25 mM) in the presence of 0.1 mM DA. (D) Calibration plot obtained for oxidation peak current against AA concentration.

Table 4.2: Comparison of various modified electrodes for the detection of DA.

Electrode	Method	Interferents	Linearity (μM)	Detection limit (μM)	Ref.
CAT ^a /ZnO Nps/CPE ^b	CA, CPA	-	5–41	3	(Fooladsaz et al., 2012)
Nanostructured gold	DPV	AA	10–100	5	(Plowman et al., 2010)
Cu ₂ O/GCE	CV	UA	0.1–10	0.01	(F. Y. Zhang et al., 2011)
TiO ₂ -graphene/GCE	CV	UA, AA	5–200	2	(Fan et al., 2011)
2-Amino-thiazol (AT) film/GCE	DPV	UA	5–25	5	(Tsai et al., 2011)
Graphene/GCE	CV	EP, UA, AA	2.5–100	0.5	(Ma et al.)
CTAB ^c / GNSP ^d	DPV	AA	4–52	0.6	(S. Q. Liu et al., 2012)
Meso-SiO ₂ /CPE	DPV	UA, AA	0.4–25	0.1	(D. Sun et al., 2010)
RGO-HDPPy ^e doped GCE	DPV	UA, AA	0.001–8	0.003	(Qian et al., 2013)
Fe ₃ O ₄ /rGO/GCE	DPV	AA	0.5–100	0.12	Present work

Foot note: ^aCatalase; ^bCarbon Paste Electrode; ^cCetyltrimethylammonium bromide; ^dGraphene nano-sheets; ^ePolypyrrole nanospheres with highly dispersibility.

CHAPTER 5: CONCLUSION AND FUTURE WORKS

5.1 Conclusion

The overall aim of present investigation is to develop a simple, stable and eco-friendly pathway for the synthesis of nanocomposite materials consisting of magnetic (Fe_3O_4) nanoparticles that uniformly decorated on the rGO sheets, with enhanced physical and chemical properties for potential applications in wastewater treatment and electrochemical detection of biomolecules.

The present work successfully developed a simple, efficient, cost-effective and environment benign approach to synthesize magnetically separable $\text{Fe}_3\text{O}_4/\text{rGO}$ nanocomposite *via* in-situ chemical deposition of Fe_3O_4 nanoparticles on the reduced graphene oxide sheets (rGO) in an alkaline condition. The particles size of Fe_3O_4 in the nanocomposites could be modified by varying the weight ratio of GO and Fe^{2+} ions in the starting material, and hence allowing the modification of the properties of nanocomposites to be modified, optimized and utilized for photocatalysis and biosensor applications. Furthermore, increasing the concentration of Fe^{2+} in the nanocomposites increase the size distribution of Fe_3O_4 nanoparticles that attached on the surface of rGO sheets, as well as the saturation magnetization of the nanocomposites. The synthesized $\text{Fe}_3\text{O}_4/\text{rGO}$ nanocomposites were dispersible in the most polar solvents, including water and ethanol, and thus they are a promising rising star material for the multifunctional applications.

This one-pot chemical approach offers great advantages over other synthesis methods reviewed. The developed nanocomposite preparation offers not only for the process control and scalability, but also allows control over the particles size and its distribution, crystal structure, electrical conductivity and magnetic properties of the nanocomposites through the modification of Fe^{2+} ions in the starting material.

Moreover, this method is environmentally benign and green approach as it does not involve any use of the toxic solvents. Additionally, the synthesis of Fe₃O₄/rGO nanocomposite occurred at room temperature, and hence the energy consumption is reduced as compared to the alternatives preparation methods such as hydrothermal, solvothermal and chemical co-precipitation which require high temperature.

The FESEM and HRTEM images portrayed that the Fe₃O₄ nanoparticles with an average size of 10 nm were uniformly embedded on the surface of rGO sheets. The XRD patterns of the Fe₃O₄/rGO nanocomposites revealed the observed diffraction peaks that attributed to the cubic spinel structure of Fe₃O₄ with good crystallinity. Moreover, the prepared Fe₃O₄/rGO nanocomposites exhibit superparamagnetic property at room temperature as shown in VSM analysis. The lower PL emission intensity of the as prepared Fe₃O₄/rGO nanocomposites indicating that incorporation of electron acceptor rGO efficiently suppressed the recombination of photoinduced electrons and holes pair and leading to rapid interfacial electron transfer which is more beneficial for the photocatalytic applications.

This novel multi-functional material, Fe₃O₄/rGO nanocomposite that possesses complementary behaviour between each constituent integrate both the electrically conductive property of graphene and superparamagnetism of Fe₃O₄ open up new opportunities for the wider and specific applications. One of a great potential application for Fe₃O₄/rGO nanocomposites was applied as a magnetically separable and high performance photocatalysts in the photodegradation dye organic pollutant. The superparamagnetic nature of synthesized Fe₃O₄/rGO nanocomposites which facilitates the simple physical separation of the catalyst from the solution enable it to be more advantageous to design suspension-based photocatalyst materials for environmental applications. In the photodegradation process, the emergence synergistic effect between

the rGO and Fe₃O₄ effectively contribute to the excellent adsorption behaviour and enhanced photocatalytic performance towards the degradation of dye. Besides, the good sustainability of this magnetically separable Fe₃O₄/rGO makes it as a promising and recyclable photocatalyst for environmental remediation applications.

The fabrication electrochemical sensor based on Fe₃O₄/rGO modified glassy carbon electrode (GCE) for the simultaneous detection of DA and AA was evaluated and described in the present study. The electrochemical studies of Fe₃O₄/rGO/GCE towards oxidation of DA were performed using cyclic voltammetry (CV) and differential pulse voltammetry (DPV) techniques. Dramatically increased current response of Fe₃O₄/rGO against the DA implying that Fe₃O₄/rGO/GCE exhibit excellent electrocatalytic activity and remarkable electron transfer rate in the DA oxidation. The good sensitivity, selectivity and lowest detection limit towards the determination of DA in the presence of AA reveals that the Fe₃O₄/rGO/GCE could be a potential candidate for the chemical sensing applications.

5.2 Future works

A magnetic nanocomposite of Fe₃O₄/rGO with both photo/electro-catalytic behaviour has been successfully produced and accomplished. However, it should be noted that there are still many improvements and possibilities that can be anticipated and promoting into a wider potential fields, such as solar cells, energy storage devices, nanoelectronics, biomedicine, magnetic fluids and catalysis. Initially, in term of fabrication Fe₃O₄/rGO nanocomposite, the characteristics of the nanocomposite should be further improved by functionalization or modification of surface properties for the Fe₃O₄ nanoparticles. Incorporation of surface functionalities such as bio-organic compounds, surfactants or polymers enables the tuning and stabilization the nanoparticles from aggregations through surface energies minimization. However, it is a

major challenge to design modified magnetically separable Fe₃O₄/rGO composite with effective surface coatings that provide optimum performance beside the surface treatment.

For the photocatalytic activity, improvements should be made through optimizing the surface area of the catalyst as well as the magnetic properties *via* preparation process. Furthermore, we could experiment with other organic pollutants, such as dichlorobenzene, methyl orange and rhodamine B for the wastewater treatment. Similarly, the sensing applications based on the Fe₃O₄/rGO/GCE can be extended and exploited for the electrochemical determination of other biomolecules and heavy metal ions, such as bisphenol A, DNA molecules, glucose, nitric oxide (NO), cadmium ions (Cd²⁺) and chromium ions (such as Cr(III), Cr(VI)) in the future works.

REFERENCES

- Ahn, T. B., Kim, J. H., Yang, H. M., Lee, J. W., & Kim, J. D. (2012). Formation pathways of magnetite nanoparticles by co-precipitation method. *Journal of Physical Chemistry C*, *116*, 6069-6076.
- Alim, K. A., Fonoberov, V. A., Shamsa, M., & Balandin, A. A. (2005). Micro-Raman investigation of optical phonons in ZnO nanocrystals. *Journal of Applied Physics*, *97*(12), 124313-124313-124315.
- Almeida, B. M., Melo Jr, M. A., Bettini, J., Benedetti, J. E., & Nogueira, A. F. (2015). A novel nanocomposite based on TiO₂/Cu₂O/reduced graphene oxide with enhanced solar-light-driven photocatalytic activity. *Applied Surface Science*, *324*(0), 419-431.
- Anderson, R. J., Bendell, D. J., & Groundwater, P. W. (2007). *Organic Spectroscopic Analysis*. United Kingdom, UK: Royal Society of Chemistry.
- Angeles, G. A., Lopez, B. P., Pardave, M. P., Silva, M. T. R., & Alegret, S. (2008). Enhanced host-guest electrochemical recognition of dopamine using cyclodextrin in the presence of carbon nanotubes. *Carbon*, *46*, 898-906.
- Ardakani, M. M., Rajabi, H., Beitollahi, H., Mirjalili, B. B. F., Akbari, A., & Taghavinia, N. (2010). Voltammetric determination of dopamine at the surface of TiO₂ nanoparticles modified carbon paste electrode. *International Journal of Electrochemical Science*, *5*, 147-157.
- Aurora, R. N., Kristo, D. A., Bista, S. R., Rowley, J. A., Zak, R. S., Casey, K. R., . . . Rosenberg, R. S. (2012). The treatment of restless legs syndrome and periodic limb movement disorder in adults—an update for 2012: practice parameters with an evidence based systematic review and meta-analyses. *Sleep*, *35*, 1039-1062.
- Bae, S., Kim, H., Lee, Y., Xu, X., Park, J. S., Zheng, Y., . . . Lijima, S. (2010). Roll-to-roll production of 30-inch graphene films for transparent electrodes. *Nature Nanotechnology*, *5*, 574-578.
- Balandin, A. A. (2011). Thermal properties of graphene and nanostructured carbon materials. *Nature Materials*, *10*, 569-581.
- Balandin, A. A., Ghosh, S., Bao, W. Z., Calizo, I., Teweldebrhan, D., Miao, F., & Lau, C. N. (2008). Superior thermal conductivity of single layer graphene. *Nano Letters*, *8*, 902-907.
- Barnes, E. O., O'Mahony, A. M., Aldous, L., Hardacre, C., & Compton, R. G. (2010). The electrochemical oxidation of catechol and dopamine on platinum in 1-Ethyl-3-methylimidazolium bis(trifluoromethylsulfonyl)imide ([C₂mim][NTf₂]) and 1-butyl-3-methylimidazolium tetrafluoroborate ([C₄mim][BF₄]): adsorption effects in ionic liquid voltammetry. *Journal of Electroanalytical Chemistry*, *646*, 11-17.
- Beydoun, D., Amal, R., Low, G., & McEvoy, S. (1999). Role of nanoparticles in photocatalysis. *Journal of Nanoparticle Research*, *1*(4), 439-458.
- Beydoun, D., Amal, R., Low, G. K.-C., & McEvoy, S. (2000). Novel photocatalyst: titania-coated magnetite. Activity and photodissolution. *The Journal of Physical Chemistry B*, *104*(18), 4387-4396.
- Bogner, A., Jouneau, P. H., Thollet, G., Basset, D., & Gauthier, C. (2007). A history of scanning electron microscopy developments: Towards “wet-STEM” imaging. *Micron*, *38*(4), 390-401.
- Bolotin, K. I., Sikes, K. J., Jiang, Z., Klima, M., Fudenberg, G., Hone, J., . . . Stormer, H. L. (2008). Ultrahigh electron mobility in suspended graphene. *Solid State Communications*, *146*, 351-355.

- Bourlinos, A. B., Gournis, D., Petridis, D., Szabo, T., Szeri, A., & Dekany, I. (2003). Graphite oxide: chemical reduction to graphite and surface modification with primary aliphatic amines and amino acids. *Langmuir*, *19*, 6050-6055.
- Brownson, D. A. C., Munro, L. J., Kampouris, D. K., & Banks, C. E. (2011). Electrochemistry of graphene: not such a beneficial electrode material? *RSC Advances*, *1*, 978-988.
- Buchenau, U., & Müller, I. (1972). Optical properties of magnetite. *Solid State Communications*, *11*(9), 1291-1293.
- Buyanova, I., Chen, W., Pozina, G., Bergman, J., Monemar, B., Xin, H., & Tu, C. (1999). Mechanism for low-temperature photoluminescence in GaNAs/GaAs structures grown by molecular-beam epitaxy. *Applied Physics Letters*, *75*(4), 501-503.
- Carrera, V., Sabater, E., Vilanova, E., & Sogorb, M. A. (2007). A simple and rapid HPLC-MS method for the simultaneous determination of epinephrine, norepinephrine, dopamine and 5-hydroxytryptamine: Application to the secretion of bovine chromaffin cell cultures. *Journal of Chromatography B*, *847*, 88-94.
- Chandra, U., Swamy, B. E. K., Gilbert, O., & Reddy, S. (2011). Determination of dopamine in presence of uric acid at poly (eriochrome black T) film modified graphite pencil electrode. *American Journal of Analytical Chemistry*, *2*, 262-269.
- Chandra, V., Park, J. S., Chun, Y., Lee, J. W., Hwang, I. C., & Kim, K. S. (2010). Water-dispersible magnetite-reduced graphene oxide composites for arsenic removal. *ACS Nano*, *4*, 3979-3986.
- Chen, C. C., Ma, W. H., & Zhao, J. C. (2010). Semiconductor-mediated photodegradation of pollutants under visible-light irradiation. *Chemical Society Reviews*, *39*, 4206-4219.
- Chicea, D. (2010). *Trends in Nanophysics: revealing magnetite nanoparticles aggregation dynamics—a SLS and DLS study*. Heidelberg, Germany: Springer-Verlag Berlin Heidelberg.
- Chieh, J., Hong, C., Yang, S., Horng, H., & Yang, H. (2010). Study on magnetic fluid optical fiber devices for optical logic operations by characteristics of superparamagnetic nanoparticles and magnetic fluids. *Journal of Nanoparticle Research*, *12*(1), 293-300.
- Chirita, M., & Grozen, I. (2009). Fe₂O₃-nanoparticles, physical properties and their photochemical and photoelectrochemical applications. *Chemistry Bulletin*, *54*(68), 1-8.
- Coleman, J. N. (2009). Liquid-phase exfoliation of nanotubes and graphene. *Advanced Functional Materials*, *19*, 3680-3695.
- Cornell, R. M., & Schwertmann, U. (2003). *The Iron Oxides: Structure, Properties, Reactions, Occurrences and Uses*. Weinheim, Germany: Wiley-VCH.
- Cranford, S. W., & Buehler, M. J. (2011). Packing efficiency and accessible surface area of crumpled graphene. *Physical Review B: Condensed Matter*, *84*, 205451-205458.
- Davey, M. W., Montagu, M. V., Inze, D., Sanmartin, M., Kanellis, A., Smirnoff, N., . . . Fletcher, J. (2000). Review plant L-ascorbic acid: chemistry, function, metabolism, bioavailability and effects of processing. *Journal of the Science of Food and Agriculture*, *80*, 825-860.
- Demas, V., & Lowery, T. J. (2011). Magnetic resonance for in vitro medical diagnostics: superparamagnetic nanoparticle-based magnetic relaxation switches. *New Journal of Physics*, *13*, 025005-025029.

- Deng, D. H., Pan, X. L., Zhang, H., Fu, Q., Tan, D. L., & Bao, X. H. (2010). Freestanding graphene by thermal splitting of silicon carbide granules. *Advanced Materials*, 22, 2168-2171.
- Deshmukh, M. M., & Singh, V. (2011). Graphene—an exciting two-dimensional material for science and technology. *Resonance*, 16(3), 238-253.
- Dorniani, D., Hussien, M. Z. B., Kura, A. U., Fakurazi, S., Shaari, A. H., & Ahmad, Z. (2012). Preparation of Fe₃O₄ magnetic nanoparticles coated with gallic acid for drug delivery. *International Journal of Nanomedicine*, 7, 5745-5756.
- El Ghandoor, H., Zidan, H., Khalil, M. M., & Ismail, M. (2012). Synthesis and some physical properties of magnetite (Fe₃O₄) nanoparticles. *International Journal of Electrochemical Science*, 7, 5734-5745.
- Ensafi, A. A., & Khayamian, M. T. T. (2009). A differential pulse voltammetric method for simultaneous determination of ascorbic acid, dopamine, and uric acid using poly (3-(5-chloro-2-hydroxyphenylazo)-4,5-dihydroxynaphthalene-2,7-disulfonic acid) film modified glassy carbon electrode. *Journal of Electroanalytical Chemistry*, 633, 212-220.
- Fan, Y., Lu, H. T., Liu, J. H., Yang, C. P., Jing, Q. S., Zhang, Y. X., . . . Huang, K. J. (2011). Hydrothermal preparation and electrochemical sensing properties of TiO₂-graphene nanocomposite. *Colloids and Surfaces B: Biointerfaces*, 83, 78-82.
- Farghali, M. A., El-Din, T. A. S., Al-Enizi, A. M., & El Bahnasawy, R. M. (2015). Graphene/magnetite nanocomposite for potential environmental application. *International Journal of Electrochemical Science*, 10, 529-537.
- Foner, S. (1959). Versatile and sensitive vibrating-sample magnetometer. *The Review of Scientific Instruments*, 30, 548-557.
- Fonin, M., Pentcheva, R., Dedkov, Y. S., Sperlich, M., Vyalikh, D. V., Scheffler, M., . . . Güntherodt, G. (2005). Surface electronic structure of the Fe₃O₄ (100): evidence of a half-metal to metal transition. *Physical Review B: Condensed Matter*, 72, 104436.
- Fooladsaz, K., Negahdary, M., Rahimi, G., Tamijani, A. H., Parsania, S., Dastjerdi, H. A., . . . Asadi, A. (2012). Dopamine determination with a biosensor based on catalase and modified carbon paste electrode with zinc oxide nanoparticles. *International Journal of Electrochemical Science*, 7, 9892-9908.
- Friak, M., Schindlmayr, A., & Scheffler, M. (2007). Ab initio study of the half-metal to metal transition in strained magnetite. *New Journal of Physics*, 9, 1-14.
- Fu, C. J., Zhao, G. G., Zhang, H. J., & Li, S. (2014). A facile route to controllable synthesis of Fe₃O₄/graphene composites and their application in lithium-ion batteries. *International Journal of Electrochemical Science*, 9, 46-90.
- Fu, L., Xia, T., Zheng, Y., Yang, J., Wang, A., & Wang, Z. (2015). Preparation of WO₃-reduced graphene oxide nanocomposites with enhanced photocatalytic property. *Ceramics International*, 41(4), 5903-5908.
- Fu, Y., & Wang, X. (2011). Magnetically separable ZnFe₂O₄-graphene catalyst and its high photocatalytic performance under visible light irradiation. *Industrial & Engineering Chemistry Research*, 50(12), 7210-7218.
- Fu, Y. S., Xiong, P., Chen, H. Q., Sun, X. Q., & Wang, X. (2012). High photocatalytic activity of magnetically separable manganese ferrite-graphene heteroarchitectures. *Industrial and Engineering Chemistry Research*, 51, 725-731.
- Gao, M., Li, W., Dong, J., Zhang, Z., & Yang, B. (2011). Synthesis and characterization of superparamagnetic Fe₃O₄@ SiO₂ core-shell composite nanoparticles. *World Journal of Condensed Matter Physics*, 1, 49-54.

- Gao, M., Peh, C. K. N., Ong, W. L., & Ho, G. W. (2013). Green chemistry synthesis of a nanocomposite graphene hydrogel with three-dimensional nano-mesopores for photocatalytic H₂ production. *RSC Advances*, 3, 13169-13177.
- Geim, A. K., & Novoselov, K. S. (2007). The rise of graphene. *Nature Materials*, 6(3), 183-191.
- Ghorai, S. (2013). *Chemical, physical and mechanical properties of nanomaterials and its applications*. (Doctoral dissertation, University of Iowa), Retrieved from <http://ir.uiowa.edu/etd/2501/>
- Gong, R., Li, M., Yang, C., Sun, Y. Z., & Chen, J. (2005). Removal of cationic dyes from aqueous solution by adsorption on peanut hull. *Journal of Hazardous Materials*, B121, 247-250.
- Gu, H. K., Zhang, R. K., Xu, X. X., & Xu, B. (2004). Facile one-pot synthesis of bifunctional heterodimers of nanoparticles: a conjugate of quantum dot and magnetic nanoparticles. *Journal of the American Chemical Society*, 126(18), 5664-5665.
- Guo, J., Wang, R. Y., Tjiu, W. W., Pan, J. S., & Liu, T. X. (2012). Synthesis of Fe nanoparticles@graphene composites for environmental applications. *Journal of Hazardous materials*, 225-226, 63-73.
- Hacisevki, A. (2009). An overview of ascorbic acid biochemistry. *Ankara Ecz. Fak. Derg.*, 38(3), 233-255.
- Han, F., Yang, S., Jing, W., Jiang, Z., Liu, H., & Li, L. A study on near-UV blue photoluminescence in graphene oxide prepared by Langmuir–Blodgett method. *Applied Surface Science*. Retrieved from <http://dx.doi.org/10.1016/j.apsusc.2015.01.214>
- Harifi, T., & Montazer, M. (2014). Fe³⁺:Ag/TiO₂ nanocomposite: Synthesis, characterization and photocatalytic activity under UV and visible light irradiation. *Applied Catalysis A: General*, 473, 104-115.
- Hoffmann, M. R., Martin, S. T., Choi, W., & Bahnemann, D. W. (1995). Environmental applications of semiconductor photocatalysis. *Chemical Reviews*, 95(1), 69-96.
- How, G. T. S., Pandikumar, A., Ming, H. N., & Ngee, L. H. (2014). Highly exposed {001} facets of titanium dioxide modified with reduced graphene oxide for dopamine sensing. *Scientific Reports*, 4.
- Huang, D. Q., Chen, C., Wu, Y. M., Zhang, H., Sheng, L. Q., Xu, H. J., & Liu, Z. D. (2012). The determination of dopamine using glassy carbon electrode pretreated by a simple electrochemical method. *International Journal of Electrochemical Science*, 7, 5510-5520.
- Hubbard, A. T., Stickney, J. L., Soriaga, M. P., Chia, V. K. F., Rosasco, S. D., Schardt, B. C., . . . Wieckowski, A. (1984). Electrochemical processes at well-defined surfaces. *Journal of Electroanalytical Chemistry and Interfacial Electrochemistry*, 168(1-2), 43-66.
- Hummers Jr, W. S., & Offeman, R. E. (1958). Preparation of graphitic oxide. *Journal of the American Chemical Society*, 80(6), 1339-1339.
- Iqbal, K., Khan, A., & Khattak, M. M. A. K. (2004). Biological significance of ascorbic acid (vitamin C) in human health-a review. *Pakistan Journal of Nutrition*, 3(1), 5-13.
- Jasuja, K., Linn, J., Melton, S., & Berry, V. (2010). Microwave-reduced uncapped metal nanoparticles on graphene: tuning catalytic, electrical, and raman properties. *The Journal of Physical Chemistry Letters*, 1(12), 1853-1860.
- Jeong, U., Teng, X., Wang, Y., yang, H., & Xia, Y. (2007). Superparamagnetic colloids: controlled synthesis and niche applications. *Advanced Materials*, 19, 33-60.

- Jia, C., Houben, L., Thust, A., & Barthel, J. (2010). On the benefit of the negative-spherical-aberration imaging technique for quantitative HRTEM. *Ultramicroscopy*, *110*(5), 500-505.
- Kamyabi, M. A., & Shafiee, M. A. (2012). Electrocatalytic oxidation of dopamine, ascorbic acid and uric acid at poly-2,6-diaminopyridine on the surface of carbon nanotubes/GC electrodes. *Journal of the Brazilian Chemical Society*, *23*, 593-601.
- Kearnes, M., & MacNaghten, P. (2006). Introduction:(re) imagining nanotechnology. *Science as Culture*, *15*(4), 279-290.
- Ketteler, G., Weiss, W., Ranke, W., & Schlögl, R. (2001). Bulk and surface phases of iron oxides in an oxygen and water atmosphere at low pressure. *Physical Chemistry Chemical Physics*, *3*, 1114-1122.
- Khollam, Y. B., Dhage, S. R., Potdar, H. S., Deshpande, S. B., Bakare, P. P., Kullarni, S. D., & Date, S. K. (2002). Microwave hydrothermal preparation of submicron-sized spherical magnetite (Fe₃O₄) powders. *Materials Letters*, *56*, 571-577.
- Kim, D. K., Zhang, Y., Kehr, J., Klason, T., Bjelke, B., & Muhammed, M. (2001). Characterization and MRI study of surfactant-coated superparamagnetic nanoparticles administrated into the rat brain. *Journal of Magnetism and Magnetic Materials*, *225*, 256-261.
- Kim, Y. K., & Min, D. H. (2012). Simultaneous reduction and functionalization of graphene oxide by polyallylamine for nanocomposite formation. *Carbon Letters*, *13*, 29-33.
- Klotz, S., Steinle-Neumann, G., Strassle, T., Philippe, J., Hansen, T., & Wenzel, M. J. (2008). Magnetism and the Verwey transition in Fe₃O₄ under pressure. *Physical Review B: Condensed Matter*, *77*, 012411.
- Kuo, W. S., & Ho, P. H. (2001). Solar photocatalytic decolorization of methylene blue in water. *Chemosphere*, *45*, 77-83.
- L. Zhang, L., Zhou, R., & Zhao, X. S. (2010). Graphene-based materials as supercapacitor electrodes. *Journal of Materials Chemistry*, *20*, 5983-5992.
- Lakshminarayanan, P. V., Toghiani, H., & Pittman, C. U. (2004). Nitric acid oxidation of vapor grown carbon nanofibers. *Carbon*, *42*, 2433-2442.
- Laviron, E. (1979). General expression of the linear potential sweep voltammogram in the case of diffusionless electrochemical systems. *Journal of Electroanalytical Chemistry and Interfacial Electrochemistry*, *101*(1), 19-28.
- Li, N., Zheng, E., Chen, X., Sun, S., You, C., Ruan, Y., & Weng, X. (2013). Layer-by-Layer Assembled Multilayer Films of Nitrogen-doped Graphene and Polyethylenimine for Selective Sensing of Dopamine. *International Journal of Electrochemical Science*, *8*, 6524-6534.
- Li, Y. L., Yao, K. L., & Liu, Z. L. (2007). Structure, stability and magnetic properties of the Fe₃O₄(1 1 0) surface: Density functional theory study. *Surface Science*, *601*, 876-882.
- Lian, P. C., Zhu, X. F., Xiang, H. F., Li, Z., Yang, W. S., & Wang, H. H. (2010). Enhanced cycling performance of Fe₃O₄-graphene nanocomposite as an anode material for lithium-ion batteries. *Electrochimica Acta*, *56*, 834-840.
- Lim, H. N., Huang, N. M., Lim, S. S., Harrison, I., & Chia, C. H. (2011). Fabrication and characterization of graphene hydrogel via hydrothermal approach as a scaffold for preliminary study of cell growth. *International Journal of Nanomedicine*, *6*, 1817-1823.
- Lim, H. N., Huang, N. M., & Loo, C. H. (2012). Facile preparation of graphene-based chitosan films: Enhanced thermal, mechanical and antibacterial properties. *Journal of Non-Crystalline Solids*, *358*, 525-530.

- Lin, Y., Geng, Z., Cai, H., Ma, L., Chen, J., Zeng, J., . . . Wang, X. (2012). Ternary graphene–TiO₂–Fe₃O₄ nanocomposite as a recyclable photocatalyst with enhanced durability. *European Journal of Inorganic Chemistry*, 2012(28), 4439-4444.
- Liu, S. Q., Sun, W. H., & Hu, F. T. (2012). Graphene nano sheet-fabricated electrochemical sensor for the determination of dopamine in the presence of ascorbic acid using cetyltrimethylammonium bromide as the discriminating agent. *Sensors and Actuators B: Chemical*, 173, 497-504.
- Liu, X. J., Pan, L. K., Lv, T., Zhu, G., Lu, T., Sun, Z., & Sun, C. Q. (2011). Microwave-assisted synthesis of TiO₂-reduced graphene oxide composites for the photocatalytic reduction of Cr(VI). *RSC Advances*, 1, 1245-1249.
- Liu, Y. L., Xie, B., Zhang, Z., Zheng, Q. S., & Xu, Z. P. (2012). Mechanical properties of graphene papers. *Journal of the Mechanics and Physics of Solids*, 60, 591-605.
- Lopez-Quintela, M. A., Tojo, C., Blanco, M. C., Rio, L. G., & Leis, J. R. (2004). Microemulsion dynamics and reactions in microemulsions. *Current Opinion In Colloid Interface Science*, 9(3), 264-278.
- Lu, T., Wang, J. H., Yin, J., Wang, A. Q., Wang, X. D., & Zhang, T. (2013). Surfactant effects on the microstructures of Fe₃O₄ nanoparticles synthesized by microemulsion method. *Colloids and Surfaces A: Physicochemical and Engineering Aspects*, 436, 675-683.
- Lue, J. T. (2007). Physical properties of nanomaterials. *Encyclopedia of Nanoscience and Nanotechnology*, 1-46.
- Ma, X. Y., Chao, M. Y., & Wang, Z. X. (2012). Electrochemical detection of dopamine in the presence of epinephrine, uric acid and ascorbic acid using a graphene-modified electrode. *Analytical Methods*, 4, 1687-1692.
- Maina, F. K., & Mathews, T. A. (2010). Functional fast scan cyclic voltammetry assay to characterize dopamine D2 and D3 autoreceptors in the mouse striatum. *ACS Chemical Neuroscience*, 1, 450-462.
- Mascolo, M. C., Pei, Y. B., & Ring, T. A. (2013). Room temperature co-precipitation synthesis of magnetite nanoparticles in a large pH window with different bases. *Materials*, 6, 5549-5567.
- Matsumoto, Y., Koinuma, M., Ida, S., Hayami, S., Taniguchi, T., Hatakeyama, K., . . . Amano, S. (2011). Photoreaction of graphene oxide nanosheets in water. *The Journal of Physical Chemistry C*, 115(39), 19280-19286.
- Milichko, V. A., Nechaev, A. I., Valtsifer, V. A., Strelnikov, V. N., Kulchin, Y. N., & Dzyuba, V. P. (2013). Photo-induced electric polarizability of Fe₃O₄ nanoparticles in weak optical fields. *Nanoscale Research Letters*, 8(1), 1-7.
- Mohammadi, M., & Akhondzadeh, S. (2011). Advances and Considerations in Attention-Deficit/Hyperactivity Disorder Pharmacotherapy. *Acta Medica Iranica*, 49, 487-498.
- Mohapatra, M., & Anand, S. (2010). Synthesis and applications of nano-structured iron oxides/hydroxides-a review. *International Journal of Engineering, Science and Technology*, 2(8), 127-146.
- Morgan, A. B., & Gilman, J. W. (2003). Characterization of polymer-layered silicate (clay) nanocomposites by transmission electron microscopy and X-ray diffraction: A comparative study. *Journal of Applied Polymer Science*, 87(8), 1329-1338.
- Mukherji, A., Seger, B., Lu, G. Q., & Wang, L. (2011). Nitrogen doped Sr₂Ta₂O₇ coupled with graphene sheets as photocatalysts for increased photocatalytic hydrogen production. *ACS Nano*, 5(5), 3483-3492.

- Naccarato, A., Gionfriddo, E., Sindona, G., & Tagarelli, A. (2014). Development of a simple and rapid solid phase microextraction-gas chromatography–triple quadrupole mass spectrometry method for the analysis of dopamine, serotonin and norepinephrine in human urine. *Analytica Chimica Acta*, *810*(0), 17-24.
- Nair, R., Blake, P., Grigorenko, A., Novoselov, K., Booth, T., Stauber, T., . . . Geim, A. (2008). Fine structure constant defines visual transparency of graphene. *Science*, *320*(5881), 1308-1308.
- Neto, A. H. C., Guinea, F., Peres, N. M. R., Novoselov, K. S., & Geim, A. K. (2009). The electronic properties of graphene. *Reviews of Modern Physics*, *81*, 109-162.
- Njagi, J., Chernov, M. M., Leiter, J. C., & Andreescu, S. (2010). Amperometric detection of dopamine in vivo with an enzyme based carbon fiber microbiosensor. *Analytical Chemistry*, *82*, 989-996.
- Novoselov, K. S. (2011). Nobel Lecture: Graphene: Materials in the Flatland. *Reviews of Modern Physics*, *83*(3), 837-849.
- Novoselov, K. S., Geim, A. K., Morozov, S. V., Jiang, D., Zhang, Y., Dubonos, S. V., . . . Firsov, A. A. (2004). Electric Field Effect in Atomically Thin Carbon Films. *Science*, *306*, 666-669.
- Novoselov, K. S., Jiang, Z., Zhang, Y., Morozov, S. V., Stormer, H. L., Zeitler, U., . . . Geim, A. K. (2007). Room-temperature quantum hall effect in graphene. *Science*, *315*, 1379.
- Obata, T. (2002). Dopamine efflux by MPTP and hydroxyl radical generation. *Journal of Neural Transmission*, *109*, 1159-1180.
- Oyer, A. J., Carrillo, J. M. Y., Hire, C. C., Schniepp, H. C., Asandei, A. D., Dobrynin, A. V., & Adamson, D. H. (2012). Stabilization of graphene sheets by a structured benzene/hexafluorobenzene mixed solvent. *Journal of the American Chemical Society*, *134*, 5018-5021.
- Pan, S. D., Zhang, Y., Shen, H. Y., & Hu, M. Q. (2012). An intensive study on the magnetic effect of mercapto-functionalized nano-magnetic Fe₃O₄ polymers and their adsorption mechanism for the removal of Hg(II) from aqueous solution. *Chemical Engineering Journal*, *210*, 564-574.
- Pankhurst, Q. A., Connolly, J., Jones, S. K., & Dobson, J. (2003). Applications of magnetic nanoparticles in biomedicine. *Journal of Physics D: Applied Physics*, *36*, R167-R181.
- Paredes, J. I., Rodil, S. V., Alonso, A. M., & Tascon, J. M. (2008). Graphene oxide dispersions in organic solvents. *Langmuir*, *24*, 10560-10564.
- Park, J. N., Lee, E. W., Hwang, N. M., Kang, M., Kim, S. C., Noh, H. J., . . . Hyeon, T. H. (2005). One-nanometer-scale size-controlled synthesis of monodisperse magnetic iron oxide nanoparticle. *Angewandte Chemie International Edition*, *44*(19), 2872-2877.
- Park, S., Ishikawa, T., & Tokura, Y. (1998). Charge-gap formation upon the Verwey transition in Fe₃O₄. *Physical Review B*, *58*(7), 3717-3720.
- Pawar, R. C., & Lee, C. S. (2014). Single-step sensitization of reduced graphene oxide sheets and CdS nanoparticles on ZnO nanorods as visible-light photocatalysts. *Applied Catalysis B: Environmental*, *144*, 57-65.
- Peng, L., Qin, P. F., Lei, M., Zeng, Q., Song, H. J., Yang, J., . . . Gu, J. D. (2012). Modifying Fe₃O₄ nanoparticles with humic acid for removal of Rhodamine B in water. *Journal of Hazardous Materials*, *209-210*, 193-198.
- Phan, T. D. N., Pham, V. H., Shin, E. W., Pham, H. D., Kim, S. W., Chung, J. S., . . . Hur, S. H. (2011). The role of graphene oxide content on the adsorption-enhanced photocatalysis of titanium dioxide/graphene oxide composites. *Chemical Engineering Journal*, *170*, 226-232.

- Plowman, B. J., Mahajan, M., O'Mullane, A. P., & Bhargava, S. K. (2010). Electrochemical detection of dopamine and cytochrome c at a nanostructured gold electrode. *Electrochimica Acta*, *55*, 8953-8959.
- Pruneanu, S., Biris, A. R., Pogacean, F., Socaci, C., Coros, M., Rosu, M. C., . . . Biris, A. S. (2015). The influence of uric and ascorbic acid on the electrochemical detection of dopamine using graphene-modified electrodes. *Electrochimica Acta*, *154*(0), 197-204.
- Puntes, V. F., Krishnan, K. M., & Alivisatos, P. A. (2001). Colloidal nanocrystal shape and size control: the case of Co. *Science*, *291*(5111), 2115-2117.
- Qian, T., Yu, C. F., Wu, S. S., & Shen, J. (2013). In situ polymerization of highly dispersed polypyrrole on reduced graphite oxide for dopamine detection. *Biosensors and Bioelectronics*, *50*, 157-160.
- Qu, S., Wang, J., Kong, J., Yang, P., & Chen, G. (2007). Magnetic loading of carbon nanotube/nano-Fe₃O₄ composite for electrochemical sensing. *Talanta*, *71*, 1096-1102.
- Ramsden, J. J. (2005). What is nanotechnology? *Nanotechnology Perceptions*, *1*, 3-17.
- Rao, C. N. R., & Cheetham, A. K. (2001). Science and technology of nanomaterials: current status and future prospects. *Journal of Materials Chemistry*, *11*, 2887-2894.
- Rao, C. N. R., Sood, A. K., Subrahmanyam, K. S., & Govindaraj, A. (2009). Graphene: The new two-dimensional nanomaterial. *Angewandte Chemie International Edition*, *48*, 7752-7777.
- Reina, A., Jia, X. T., Ho, J., Nezich, D., Son, H. B., Bulovic, V., . . . Kong, J. (2009). Large Area, few-layer graphene films on arbitrary substrates by chemical vapor deposition. *Nano Letters*, *9*(1), 30-35.
- Ren, L. L., Huang, S., Fan, W., & Liu, T. X. (2011). One-step preparation of hierarchical superparamagnetic iron oxide/graphene composites via hydrothermal method. *Applied Surface Science*, *258*, 1132-1138.
- Ritter, K., Odziemkowski, M. S., & Gillham, R. W. (2002). An in situ study of the role of surface films on granular iron in the permeable iron wall technology. *Journal of Contaminant Hydrology*, *55*, 87-111.
- Rockenberger, J., Scher, E. C., & Alivisatos, A. P. (1999). A new nonhydrolytic single-precursor approach to surfactant-capped nanocrystals of transition metal oxides. *Journal of the American Chemical Society*, *121*(49), 11595-11596.
- Sahoo, S. K., Agarwal, K., Singh, A. K., Polke, B. G., & Raha, K. C. (2010). Characterization of γ - and α -Fe₂O₃ nano powders synthesized by emulsion precipitation-calcination route and rheological behaviour of α -Fe₂O₃. *International Journal of Engineering, Science and Technology*, *2*(8), 118-126.
- Sathish, M., Tomai, T., & Honma, I. (2012). Graphene anchored with Fe₃O₄ nanoparticles as anode for enhanced Li-ion storage. *Journal of Power Sources*, *217*, 85-91.
- Schleicher, R. L., Carroll, M. D., Ford, E. S., & Lacher, D. A. (2009). Serum vitamin C and the prevalence of vitamin C deficiency in the United States: 2003-2004 National Health and Nutrition Examination Survey (NHANES)^{1,2}. *The American Journal of Clinical Nutrition*, *90*, 1252-1263.
- Seyller, T. (2011). Graphene: a new electronics material. Retrieved 28 June, 2011, from <http://www.graphene.nat.uni-erlangen.de/grapheneng.htm>
- Sharma, A., Kyotani, T., & Tomita, A. (2000). Comparison of structural parameters of PF carbon from XRD and HRTEM techniques. *Carbon*, *38*(14), 1977-1984.
- Shao, C. N., Chao, C. G., Wu, T. M., & Shy, H. J. (2007). Magnetic and optical properties of isolated magnetite nanocrystals. *Materials Transactions*, *48*(5), 1143-1148.

- Silva, M., Marques, R., Machado, N., & Santos, O. (2002). Evaluation of Nb₂O₅ and Ag/Nb₂O₅ in the photocatalytic degradation of dyes from textile industries. *Brazilian Journal of Chemical Engineering*, 19(4), 359-363.
- Singh, S., Swarnkar, R., & Gopal, R. (2010). Zn/ZnO core/shell nanoparticles synthesized by laser ablation in aqueous environment: optical and structural characterizations. *Bulletin of Materials Science*, 33(1), 21-26.
- Skoog, D. A., & West, D. M. (1980). *Principles of instrumental analysis* (Vol. 158, 5th ed). New York, NY : Saunders College Philadelphia.
- Somani, P. R., Somani, S. P., & Umeno, M. (2006). Planer nano-graphenes from camphor by CVD. *Chemical Physics Letters*, 430, 56-59.
- Stankovich, S., Dikin, D. A., Dommett, G. H., Kohlhaas, K. M., Zimney, E. J., Stach, E. A., . . . Ruoff, R. S. (2006). Graphene-based composite materials. *Nature*, 442(7100), 282-286.
- Stankovich, S., Dikin, D. A., Piner, R. D., Kohlhaas, K. A., Kleinhammes, A., Jia, Y. Y., . . . Ruoff, R. S. (2007). Synthesis of graphene-based nanosheets via chemical reduction of exfoliated graphite oxide. *Carbon*, 45, 1558-1565.
- Stankovich, S., Piner, R. D., Chen, X. Q., Wu, N. Q., Nguyen, S. T., & Ruoff, R. S. (2006). Stable aqueous dispersions of graphitic nanoplatelets via the reduction of exfoliated graphite oxide in the presence of poly(sodium 4-styrenesulfonate). *Journal of Materials Chemistry*, 16, 155-158.
- Su, J., Cao, M. H., Ren, L., & Hu, C. W. (2011). Fe₃O₄-Graphene Nanocomposites with Improved Lithium Storage and Magnetism Properties. *Journal of Physical Chemistry C*, 115, 14469-14477.
- Sun, D., Xie, X. F., & Zhang, H. J. (2010). Surface effects of mesoporous silica modified electrode and application in electrochemical detection of dopamine. *Colloids and Surfaces B: Biointerfaces*, 75, 88-92.
- Sun, W., Wang, Y., Zhang, Y. Y., Ju, X. M., Li, G. J., & Sun, Z. F. (2012). Poly(methylene blue) functionalized graphene modified carbon ionic liquid electrode for the electrochemical detection of dopamine. *Analytica Chimica Acta*, 751, 59-65.
- Teja, A. S., & Koh, P. Y. (2009). Synthesis, properties, and applications of magnetic iron oxide nanoparticles. *Progress in Crystal Growth and Characterization of Materials*, 55, 22-45.
- Teymourian, H., Salimi, A., & Khezrian, S. (2013). Fe₃O₄ magnetic nanoparticles/reduced graphene oxide nanosheets as a novel electrochemical and bioelectrochemical sensing platform. *Biosensors and Bioelectronics*, 49(0), 1-8.
- Thorek, D. L., Chen, A. K., Czupryna, J., & Tsourkas, A. (2006). Superparamagnetic iron oxide nanoparticle probes for molecular imaging. *Annals of Biomedical Engineering*, 34(1), 23-38.
- Tsai, T. H., Huang, Y. C., Chen, S. M., Ali, M. A., & AlHemaid, F. M. A. (2011). Fabrication of multifunctional biosensor for the determination of hydrogen peroxide, dopamine and uric acid. *International Journal of Electrochemical Science*, 6, 6456-6468.
- Tung, T. T., Feller, J. F., Kim, T. Y., Kim, H. K., Yang, W. S., & Suh, K. S. (2011). Electromagnetic properties of Fe₃O₄-functionalized graphene and its composites with a conducting polymer. *Journal of Polymer Science Part A: Polymer Chemistry*, 50(5), 927-935.
- Ul Hasan, K. (2012). *Graphene and ZnO Nanostructures for Nano-Optoelectronic & Biosensing Applications* (Doctoral Thesis, Linköping University). Retrieved from <http://urn.kb.se/resolve?urn=urn:nbn:se:liu:diva-78697>

- Vanheusden, K., Seager, C., Warren, W. t., Tallant, D., & Voigt, J. (1996). Correlation between photoluminescence and oxygen vacancies in ZnO phosphors. *Applied Physics Letters*, 68(3), 403-405.
- Varchon, F., Feng, R., Hass, J., Li, X., Nguyen, B. N., Naud, C., . . . Magaud, L. (2007). Electronic structure of epitaxial graphene layers on SiC: effect of the substrate. *Physical Review Letters*, 99, 126805-126809.
- Vlassioug, I., Smirnov, S., Ivanov, I., Fulvio, P. F., Dai, S., Meyer, H., . . . Lavrik, N. V. (2011). Electrical and thermal conductivity of low temperature CVD graphene: the effect of disorder. *Nanotechnology*, 22, 275716.
- Wang, J., Tang, B., Tsuzuki, T., Liu, Q., Hou, X., & Sun, L. (2012). Synthesis, characterization and adsorption properties of superparamagnetic polystyrene/Fe₃O₄/graphene oxide. *Chemical Engineering Journal*, 204–206(0), 258-263.
- Wang, X. W., Tan, H. W., Yang, Y., Wang, H., Wang, S. M., Zheng, W. T., & Liu, Y. C. (2012). Reduced graphene oxide/CdS for efficiently photocatalytic degradation of methylene blue. *Journal of Alloys and Compounds*, 524, 5-12.
- Wu, L., Feng, L., Ren, J., & Qu, X. (2012). Electrochemical detection of dopamine using porphyrin-functionalized graphene. *Biosensors and Bioelectronics*, 34, 57-62.
- Wu, Q. H., Feng, C., Wang, C., & Wang, Z. (2013). A facile one-pot solvothermal method to produce superparamagnetic graphene-Fe₃O₄ nanocomposite and its application in the removal of dye from aqueous solution. *Colloids and Surfaces B: Biointerfaces*, 101, 210-214.
- Wu, W., He, Q. G., & Jiang, C. Z. (2008). Magnetic iron oxide nanoparticles: synthesis and surface functionalization strategies. *Nanoscale Research Letters*, 3, 397-415.
- Wu, W., Jiang, C., & Roy, V. A. (2015). Recent progress in magnetic iron oxide–semiconductor composite nanomaterials as promising photocatalysts. *Nanoscale*, 7(1), 38-58.
- Xu, X. D., Zhang, H. Y., Shi, H. M., Ma, C. L., Cong, B., & Kang, W. J. (2012). Determination of three major catecholamines in human urine by capillary zone electrophoresis with chemiluminescence detection. *Analytical Biochemistry*, 427, 10-17.
- Yusoff, N., Kumar, S. V., Pandikumar, A., Huang, N. M., Marlinda, A. R., & An'amt, M. N. (2015). Core-shell Fe₃O₄-ZnO nanoparticles decorated on reduced graphene oxide for enhanced photoelectrochemical water splitting. *Ceramics International*, 41(3, Part B), 5117-5128.
- Zedan, A. F., Sappal, S., Moussa, S., & El-Shall, M. S. (2010). Ligand-controlled microwave synthesis of cubic and hexagonal CdSe nanocrystals supported on graphene. photoluminescence quenching by graphene. *Journal of Physical Chemistry C*, 114, 19920-19927.
- Zhang, F. Y., Li, Y. J., Gu, Y., Wang, Z. H., & Wang, C. M. (2011). One-pot solvothermal synthesis of a Cu₂O/graphene nanocomposite and its application in an electrochemical sensor for dopamine. *Electrochimica Acta*, 173, 103-109.
- Zhang, H., & Zhu, G. Q. (2012). One-step hydrothermal synthesis of magnetic Fe₃O₄ nanoparticles immobilized on polyamide fabric. *Applied Surface Science*, 258, 4952-4959.
- Zhang, L. W., Xu, T. G., Cheng, H. Y., & Zhu, Y. F. (2010). Significantly Enhanced Photocatalytic Performance of ZnO via Graphene Hybridization and the Mechanism Study. *Applied Physics B*, 101, 382-387.
- Zhang, M., Lei, D., Chen, L. B., Li, Q. H., Wang, Y. G., & Wang, T. H. (2010). Magnetite/graphene composites: microwave irradiation synthesis and enhanced

- cycling and rate performances for lithium ion batteries. *Journal of Materials Chemistry*, 20, 5538-5543.
- Zhang, W., Zheng, J., Shi, J., Lin, Z., Huang, Q., Zhang, H., . . . Hao, A. (2015). Nafion covered core-shell structured Fe₃O₄@graphene nanospheres modified electrode for highly selective detection of dopamine. *Analytica Chimica Acta*, 853(0), 285-290.
- Zhang, X., Jiang, B., Xie, Y. P., & Du, F. (2014). One-pot hydrothermal synthesis of Fe₃O₄/reduced graphene oxide nanocomposite for enhanced lithium storage. *Indian Journal of Chemical*, 53A, 265-273.
- Zhang, Y., Tian, J., Li, H., Wang, L., Qin, X., Asiri, A. M., . . . Sun, X. (2012). Biomolecule-assisted, environmentally friendly, one-pot synthesis of CuS/reduced graphene oxide nanocomposites with enhanced photocatalytic performance. *Langmuir*, 28(35), 12893-12900.
- Zhang, Y. X., Cheng, Y. X., Zhou, Y. Y., Li, B. Y., Gu, W., Shi, X. H., & Xian, Y. Z. (2013). Electrochemical sensor for bisphenol A based on magnetic nanoparticles decorated reduced graphene oxide. *Talanta*, 107, 211-218.
- Zhang, Z., Wang, W., Wang, L., & Sun, S. (2012). Enhancement of visible-light photocatalysis by coupling with narrow-band-gap semiconductor: a case study on Bi₂S₃/Bi₂WO₆. *ACS Applied Materials & Interfaces*, 4(2), 593-597.
- Zhou, C., Zhang, W., Wang, H., Li, H., Zhou, J., Wang, S., . . . Zhou, J. (2014). Preparation of Fe₃O₄-embedded graphene oxide for removal of methylene blue. *Arabian Journal for Science and Engineering*, 39(9), 6679-6685.
- Zhou, L., Shao, Y., Liu, J., Ye, Z., Zhang, H., Ma, J., . . . Li, Y. (2014). Preparation and characterization of magnetic porous carbon microspheres for removal of methylene blue by a heterogeneous Fenton reaction. *ACS Applied Materials & Interfaces*, 6(10), 7275-7285.
- Zhu, S. M., Guo, J. J., Dong, J. P., Cui, Z. W., Lu, T., Zhu, C. L., . . . Ma, J. (2013). Sonochemical fabrication of Fe₃O₄ nanoparticles on reduced graphene oxide for biosensors. *Ultrasonics Sonochemistry*, 20, 872-880.
- Zhu, Z., Qu, L., Guo, Y., Zeng, Y., Sun, W., & Huang, X. T. (2010). Electrochemical detection of dopamine on a Ni/Al layered double hydroxide modified carbon ionic liquid electrode. *Sensors and Actuators B: Chemical*, 151, 146-152.